X-ray and Raman scattering studies of novel phases in $3d$ and $4d$ transition metal oxides

Von der Fakultät Mathematik und Physik der Universität Stuttgart
zur Erlangung der Würde eines Doktors der Naturwissenschaften (Dr.
rer. nat.) genehmigte Abhandlung

Vorgelegt von:

Katrin Fürsich

aus Weißenburg i. Bay., Deutschland

Hauptberichter:	Prof. Dr. Bernhard Keimer
Mitberichter:	Prof. Dr. Tilman Pfau
	Prof. Dr. Vladimir Hinkov
Prüfungsvorsitzende:	Prof. Dr. Maria Daghofer
Tag der Einreichung:	14.10.2020
Tag der mündlichen Prüfung:	18.11.2020

Contents

Abstract

Due to an intricate interplay of electronic, magnetic, orbital, and structural degrees of freedom, transition metal oxides host a variety of nearly degenerate phases. These intertwined correlations can lead to a plethora of fascinating phenomena such as multiferroicity, colossal magnetoresistance, or even high-temperature superconductivity. The fine energy balance of Coulomb correlations, crystal field effects, and spin-orbit coupling results in rich and complex phase diagrams hosting several electronic, magnetic, and structural transitions triggered by external perturbations such as chemical doping, temperature, or pressure changes. The unprecedented opportunities offered by these so-called *quantum materials* are direct manifestations of quantum mechanics on a macroscopic scale and their application could unleash a revolution in modern technology in several fields, such as electronics, energy storage and conversion, sensing, etc. However, the ultimate control and use of transition metal oxides, *e.g.* as active elements in electronic devices, requires a fundamental understanding of the underlying physical phenomena in order to tailor the specific material behavior.

In this thesis we focus on two representative transition metal oxide systems, the rare-earth nickelates of composition RNiO$_3$ and the single layer ruthenate Ca$_2$RuO$_4$, whose magnetic and electronic responses show an exceptional susceptibility to structural deformations, such as tilts and rotations of the rather rigid NiO$_6$ or RuO$_6$ octahedra. To date most research on both compounds has focused on bulk crys-

talline samples or powders with modified composition, mostly through cation exchange. Here, we introduce different perturbations to further explore the phase diagram of these compounds. In particular, we stabilize phases without analogue in the bulk materials' systems by means of heterostructuring and electrical currents. Besides the creation of novel phases, the study of a perturbed system offers the possibility to access the microscopic energy scales at play and to discriminate the hierarchy of several order parameters, which are often simultaneously present in correlated oxide materials and sometimes difficult to disentangle. For all studies presented in this thesis we use experimental techniques based on light scattering to probe direct manifestations of a modified electronic and magnetic structure. Thereby, we access and quantify microscopically relevant parameters, such as the magnetic exchange coupling constants, which drive the low-energy physics in the equilibrium and nonequilibrium states of transition metal oxides.

We first focus on the rare-earth nickelates, which are archetypal correlated oxides showing a Mott metal-to-insulator transition and a unique antiferromagnetic order which is incompatible with simple superexchange models. This peculiar spin order and its interplay with the bond order that accompanies the metal-insulator transition has been subject to investigation for decades. Heterostructures comprising rare-earth nickelates have revealed fascinating opportunities to selectively control different order parameters, where phases with modified magnetic or bond order, such as spin-density waves, were realized. However, a full understanding of the electronic properties and the hierarchy of order parameters in RNiO$_3$, both in bulk form and as thin active layers in heterostructures, remains elusive mainly because of the lack of a suitable probe to simultaneously investigate spin and bond order. Here, we exploit the unique capabilities of resonant inelastic x-ray scattering to study both magnetic and bond order in rare-earth nickelates on a quantitative level. Using advanced modeling based on a double cluster approach to reproduce the experimental datasets, we

quantify the bond order in bulk-like samples and heterostructures. We find that the bond disproportionation in superstructures is suppressed due to two-dimensional confinement. Furthermore, we investigate the magnetic order and exchange interactions in the very same samples by measuring their dispersive spin excitations. First, we focus on a bulk-like reference sample and develop a microscopic model to explain the peculiar antiferromagnetic spin spiral that characterizes the magnetic structure of RNiO$_3$ systems. Using this spin-only model, we quantify the exchange interactions in rare-earth nickelates. Next, we look into heterostructures with modified bond disproportionation and a magnetic state different from the bulk. Our study of superlattices grown in the [001] direction of the perovskite structure reveals a robust non-collinear spin spiral magnetic order with dispersive magnon excitations that are essentially unperturbed by bond order modulations and spatial confinement. By contrast, we find magnons with flat dispersions and strongly reduced energies in superlattices grown in the [111] direction of the pseudocubic perovskite structure that exhibit collinear magnetic ordering. These results give insight into the interplay of different collective ordering phenomena in a prototypical $3d$ transition metal oxide and identify resonant inelastic x-ray scattering as a powerful tool to quantitatively study several order parameters and the corresponding collective excitations within a single experiment.

In another set of experiments, we develop further understanding enabling the epitaxial control of transition metal oxides and their properties. In particular, we access and quantify the underlying length scales that allow the stabilization of novel phases by means of heterostructuring. To this end we investigate the influence of epitaxial strain and two dimensional confinement in NdNiO$_3$ thin films using several complementary methods, such as electrical transport measurements, scanning transmission electron microscopy, and resonant elastic x-ray scattering. Our study focuses on the evolution of the metal-to-insulator and antiferromagnetic transitions in NdNiO$_3$ films as a function of film

thickness and $NdGaO_3$ crystallographic substrate orientation. We find that modifications of the NiO_6 octahedral network are the crucial factor for tuning the transition temperatures over a wide temperature range, while the metal-to-insulator transition is more susceptible to structural modifications. This observation is in accordance with density functional theory calculations, which reveal that small differences in the structural properties substantially affect the electronic interactions. Moreover, our resonant x-ray scattering study of the magnetic phase reveals that the period-four magnetic state is a robust order, where heteroepitaxially induced modifications of the bond disproportionation are reflected in the microscopic spin structure. Our results provide insights into the structure-property relationship of a correlated electron system and its evolution on microscopic length scales. This opens further prospects for the epitaxial control of macroscopic phases in metal-oxide heterostructures.

Interesting new physics emerge in the study of a second correlated oxide material, the single layer ruthenate Ca_2RuO_4— a $4d$ transition metal oxide with larger spin-orbit coupling compared to $3d$ transition metal oxides. The increasing strength of the spin-orbit coupling enhances the susceptibility of the magnetic ground state to structural distortions, which is reflected in a rich phase diagram as a function of pressure, temperature, and doping. At ambient pressure, pure Ca_2RuO_4 hosts a temperature-driven metal-to-insulator transition and an unconventional antiferromagnetic state. Recent experiments have revealed a method to dynamically and continuously tune the properties of Ca_2RuO_4 by the application of electrical currents. The *in-situ* control of transition metal oxides constitutes an important step towards a future use of these materials as active elements for *in-operando* systems. While several recent studies report current-driven transitions into metallic and semimetallic states in Ca_2RuO_4, fundamental questions such as the microscopic mechanism and the possible role of Joule heating remain unanswered so far. We use Raman light scattering to study

the effect of heating in the current-stabilized nonequilibrium phases of Ca_2RuO_4 and find that heating is not the cause of the new phase in an actively cooled environment. We further investigate the current-stabilized phases of Ca_2RuO_4 as a function of temperature and current and identify manifestations of orbital and charge fluctuations in the nonequilibrium semimetallic and metallic states. Our results demonstrate that the semimetallic state is a genuine effect of the applied electrical current and that the current-induced phases exhibit characteristics distinct from the equilibrium ones.

In summary, the studies performed within the scope of this thesis illustrate the possibility to stabilize exotic and novel phases by means of heteroepitaxy and electrical currents. Additionally, we demonstrate that a synergistic combination of light scattering with theoretical models and complementary experimental methods provides access to the competing energy scales, which govern the electronic structure and consequently the macroscopic properties of these compounds. Our results provide quantitative insights into crucial microscopic parameters, such as exchange couplings, of unperturbed and nonequilibrium states in oxide materials and demonstrate opportunities to fine-tune the macroscopic properties of quantum materials, by exploiting external perturbations. Therefore this thesis paves the road to harness the rich properties and functionalities of transition metal oxides for the next-generation of on-demand applications.

Zusammenfassung

Aufgrund eines komplexen Wechselspiels von elektronischen, orbitalen, magnetischen und strukturellen Freiheitsgraden besitzen Übergangsmetalloxide eine Vielzahl von energetisch dicht beieinanderliegenden Phasen. In diesem Zusammenhang können faszinierende Phänomene wie Multiferroizität, kolossaler Magnetwiderstand oder sogar Hochtemperatursupraleitung auftreten. Die fein abgestimmte Balance zwischen verschiedenen Energieskalen, wie z. B. elektronischen Korrelationen, Kristallfeld-Effekten und Spin-Bahn Kopplung, spiegelt sich in komplexen und vielfältigen Phasendiagrammen der Übergangsmetalloxide wider, die zumeist mehrere elektronische, magnetische und strukturelle Übergänge in Abhängigkeit von externen Einflüssen wie Temperatur, Druck oder chemischer Dotierung aufweisen. Die beispiellose Fülle an Eigenschaften dieser Materialklasse ist eine direkte Manifestation quantenmechanischer Effekte auf einer menschlich erfassbaren Skala. Anwendungsmöglichkeiten dieser Effekte besitzen großes Potential eine technische Revolution auszulösen. Für eine volle Kontrolle und Nutzung von Übergangsmetalloxiden als Bestandteil von aktiven Bauelementen, zum Beispiel in elektronischen Schaltungen, ist jedoch ein umfassendes Verständnis der zugrundeliegenden physikalischen Phänomene nötig.

In der vorliegenden Doktorarbeit fokussieren wir uns auf zwei typische Übergangsmetalloxide, die Seltenerd-Nickelate RNiO$_3$ und das quasi-zweidimensionale System Ca$_2$RuO$_4$. Elektronische und magnetis-

che Eigenschaften beider Materialsysteme weisen eine außergewöhn-
liche Sensitivität gegenüber strukturellen Modifizierungen auf, wie zum
Beispiel der Rotation oder Neigung der relativ starren NiO_6 bzw. RuO_6
Oktaeder. Bis heute hat sich der größte Teil der Forschung an diesen
Systemen auf die Volumeneigenschaften konzentriert, die an vergleich-
sweise großen und massiven Proben in kristalliner- oder Pulverform bes-
timmt wurden. Zudem wurden verschiedene Materialvarianten mit le-
icht veränderter Zusammensetzung untersucht. In dieser Arbeit nutzen
wir andere externe Einflüsse aus, um die Komplexität und Vielfalt der
Volumenphasendiagramme zu erforschen, sowie exotische Nichtgleich-
gewichtszustände zu stabilisieren, die kein Analogon im unbeeinflussten
Materialsystem haben. Die extrinsisch beeinflussten, und so aus dem
Gleichgewicht gebrachten Zustände bieten zudem die Möglichkeit in-
trinsische Energieskalen des Materialsystems und die Hierarchie ver-
schiedener Ordnungsparameter zu bestimmen. In korrelierten Oxiden
sind oft mehrere Ordnungsparameter koexistent, was eine getrennte
Untersuchung erschwert. In allen Studien, die in dieser Arbeit aufge-
führt werden, setzen wir Experimente basierend auf Lichtstreuung ein,
um den direkten Einfluss der externen Störung auf die elektronische
Struktur zu untersuchen. Dies erlaubt uns mikroskopisch relevante Pa-
rameter, wie z. B. die Austauschwechselwirkung, zu quantifizieren und
so wichtige Einblicke in die zugrundeliegende Physik von Übergangs-
metalloxiden zu gewinnen.

Zunächst konzentrieren wir uns auf die Materialklasse der Seltenerd-
Nickelate, die als Prototyp für ein stark korreliertes Elektronensys-
tem betrachtet werden können. Die Seltenerd-Nickelate zeigen, als
Funktion der Temperatur und des Seltenerdionenradius, einen Mott-
artigen Metall-zu-Isolator Übergang und eine charakteristische antifer-
romagnetische Ordnung, die kein Pendant in anderen oxidischen Ma-
terialien hat. Sowohl die einzigartige mikroskopische Anordnung der
Spins in diesem System als auch das Wechselspiel von magnetischer
Ordnung und Bindungsdisproportionierung, die als Schlüsselmechanis-

mus des Metall-zu-Isolator Übergangs angesehen wird, sind seit Jahrzehnten Gegenstand intensivster Forschungsarbeit. Heterostrukturen bestehend aus Seltenerd-Nickelaten zeigen faszinierende Möglichkeiten unterschiedliche Ordnungsparameter selektiv zu kontrollieren, wobei neuartige Phasen mit einer veränderten Spinstruktur oder Spindichtewellen realisiert werden können. Viele Fragen bezüglich der elektronischen Struktur, sowohl in Volumenmaterialien als auch Dünnfilmstrukturen, sind jedoch noch offen, da bisher die Möglichkeit fehlte magnetische Ordnung und Bindungsdisproportionierung gleichzeitig zu untersuchen. In der vorliegenden Arbeit bedienen wir uns der resonanten inelastischen Röntgenstreuung, die uns die einzigartige Möglichkeit bietet, magnetische Ordnung und Bindungsdisproportionierung in den Seltenerd-Nickelaten gleichzeitig zu quantifizieren. Mithilfe von Modellrechnungen basierend auf einem Doppel-Cluster-Ansatz bestimmen wir die Amplitude und damit die Stärke der Bindungsdisproportionierung in Dünnschichten und Heterostrukturen. Unsere Untersuchung enthüllt eine starke Unterdrückung der Bindungsdisproportionierung in Übergittern, verursacht durch die Heteroepitaxie. Anschließend ermitteln wir in den gleichen Proben die magnetische Ordnung einschließlich der vorliegenden Austauschwechselwirkungen durch die Analyse dispersiver Spinanregungen, auch Magnonen genannt. Zunächst betrachten wir relativ dicke Filme und entwickeln ein neues mikroskopisches Modell, durch das die ungewöhnliche antiferromagnetische Ordnung erstmals durch die Berücksichtigung eines sogenannten Doppelaustauschbeitrags verstanden werden kann. Dieses Spinmodell ermöglicht es weiterhin die Größe der Austauschwechselwirkungen in den Seltenerd-Nickelaten zu bestimmen. Im Anschluss untersuchen wir Heterostrukturen, die eine modifizierte Bindungsdisproportionierung bzw. Spinordnung im Vergleich zu den Volumenproben aufweisen. Übergitter, die in der [001] Richtung der Perovskitstruktur gewachsen wurden, zeigen eine robuste Spinspirale mit dispersiven Spinanregungen, die größtenteils unabhängig von der reduzierten Bindungsdisproportionierung und

räumlichen Einschränkung sind. Im Gegensatz dazu beobachten wir Magnonen mit flacher Dispersion und reduzierter Anregungsenergie in Übergittern, die in der [111] Richtung gewachsen wurden und kollineare magnetische Ordnung aufweisen. Diese Erkenntnisse geben wichtige, neue Einblicke in das Wechselspiel verschiedener kollektiver Ordnungsphänomene in einem typischen $3d$ Übergangsmetalloxid und etablieren die resonante inelastische Röntgenstreuung als wertvolle Methode, um verschiedene Ordnungsparameter und die korrespondierenden kollektiven Anregungen quantitativ in ein und dem selben Experiment zu bestimmen.

Im weiteren Verlauf dieser Arbeit quantifizieren wir auch die mikroskopischen Längenskalen auf denen die epitaktische Kontrolle von Übergangsmetalloxiden und deren Eigenschaften möglich ist. Deshalb untersuchen wir den Einfluss epitaktischer Verspannung und zweidimensionaler Einschränkung der elektronischen Struktur auf $NdNiO_3$-Dünnflime mit verschiedenen komplementären Methoden, wie z. B. Transportmessungen, Raster-Transmissionselektronenmikroskopie und resonanter elastischer Röntgenstreuung. Wir analysieren insbesondere die Temperatur des Metall-zu-Isolator und des magnetischen Übergangs in Abhängigkeit von der Filmdicke und der Orientierung des $NdGaO_3$ Substrates. Unsere Studie zeigt, dass eine modifizierte Anordnung der NiO_6 Oktaeder auschlaggebend ist, um die Übergangstemperaturen über einen weiten Bereich zu variieren, wobei die Übergangstemperatur des Metall-zu-Isolator Übergangs deutlich sensitiver auf strukturelle Veränderungen reagiert. Letzteres kann mittels Dichtefunktionaltheorie erklärt werden, da kleine strukturelle Modifikationen von einer substanziellen Veränderung in den elektronischen Wechselwirkungen und der Bindungsdisproportionierung begleitet werden. Die Untersuchung der magnetischen Ordnung mit resonanter Röntgenstreuung deutet darauf hin, dass die Spinordnung mit einer Periodizität von vier Einheitszellen ein robuster Ordnungszustand ist, welcher lediglich durch eine grundlegend veränderte Bindungsdisproportionierung moduliert wird. Unsere

Ergebnisse geben direkten Einblick in das eng verknüpfte Wechselspiel zwischen strukturellen und elektronischen Eigenschaften in einem korrelierten Oxid, sowie dessen Entwicklung hin zu mikroskopischen Längenskalen. Zudem werden konkrete Möglichkeiten aufgezeigt, wie man neuartige makroskopische Zustände in Übergangsmetalloxiden mittels Epitaxie in Heterostrukturen gezielt stabilisieren kann.

Als zweites Materialsystem untersuchen wir Ca_2RuO_4 — ein $4d$ Übergangsmetalloxid welches eine größere Spin-Bahn Kopplung im Vergleich zu den $3d$ Oxiden aufweist. Die ausgeprägte Spin-Bahn Kopplung in diesem System erhöht die Empfindlichkeit der elektronischen Struktur gegenüber strukturellen Variationen, was sich in einem vielfältigen Phasendiagramm mit Übergängen abhängig von Temperatur, Druck oder Dotierung widerspiegelt. Ca_2RuO_4 besitzt einen temperaturgetriebenen Metall-zu-Isolator Übergang und, auch hier, basiert die antiferromagnetische Ordnung auf einem außergewöhnlichen Mechanismus. Neueste Forschungsarbeiten haben die Möglichkeit aufgezeigt, die Eigenschaften des Materialsystem dynamisch und kontinuierlich durch elektrische Ströme zu modulieren. Diese *in-situ* Kontrolle der Materialeigenschaften von Übergangsmetalloxiden ist ein wichtiger Schritt für die Verwendung von oxidischen Materialien als aktive Bauelemente für *in-operando* Systeme. In einigen neuen Arbeiten wurden stromgetriebene Übergänge in metallische und halbmetallische Phasen in Ca_2RuO_4 beobachtet, wobei grundlegenden Fragen zum mikroskopischen Mechanismus, sowie dem Einfluss von joulescher Erwärmung durch den Strom noch offen sind. In dieser Studie setzen wir Raman-Lichtstreuung ein, um die Erwärmung in den durch den Strom stabilisierten Nichtgleichgewichtszuständen von Ca_2RuO_4 zu untersuchen. Wir zeigen, dass die Strom-induzierte Erwärmung komplett vermieden werden kann, wenn die Probenumgebung aktiv gekühlt wird. Des Weiteren vermessen wir die durch den Strom stabilisierten Phasen von Ca_2RuO_4 als Funktion von Temperatur und Stromstärke, und finden Hinweise auf Ladungs- und Orbitalfluktuationen in den metallisch-

en und halbmetallischen Nichtgleichgewichtszuständen. Unsere Ergebnisse stellen eindeutig klar, dass die halbmetallische Phase allein auf den angelegten Strom zurückgeführt werden kann, und identifizieren spezielle Eigenschaften der Nichtgleichgewichtszustände, die im ungestörten Zustand nicht vorliegen.

Zusammengefasst zeigen die in der vorliegenden Arbeit präsentierten Studien die Möglichkeiten auf, exotische Zustände mithilfe von Heteroepitaxie und Stromfluss zu stabilisieren. Zudem verdeutlichen wir, dass eine synergetische Kombination von Lichtstreuexperimenten und theoretischen Modellrechnungen die Bestimmung von mikroskopischen Energieskalen ermöglichen, welche die elektronische Struktur und schlussendlich das makroskopische Verhalten von Übergangsmetalloxiden definieren. Unsere Ergebnisse geben quantitative Einblicke in fundamentale mikroskopische Wechselwirkungsparameter von oxidischen Materialien für Phasen im und außerhalb des Gleichgewichtszustands, und verdeutlichen das Potenzial welches externe Einflüsse bieten, um die Charakteristika von Quantenmaterialen maßzuschneidern. Hierdurch offenbaren sich ungeahnte Möglichkeiten für die Anwendung von Übergangsmetalloxiden, da diese Vielzahl von Eigenschaften reichhaltige Funktionalitäten mit sich bringt.

Acronyms

ABF	annular bright-field, imaging technique in transition electron microscopy
AFM	antiferromagnetic/antiferromagnetism
BESSY II	Berliner Elektronenspeicherring-Gesellschaft für Synchrotronstrahlung II, synchrotron facility in Berlin, Germany
CCD	charge-coupled device, detector used *e.g.* for Raman and RIXS experiments
DFT	density functional theory
ERIXS	RIXS spectrometer at the ID32 beamline at the ESRF, France
ESRF	European Synchrotron Radiation Facility, synchrotron facility in Grenoble, France
FM	ferromagnetic
FWHM	full width at half maximum
HAADF	high-angle annular dark-field, imaging technique in transition electron microscopy
INS	inelastic neutron scattering
LB	long bond, one type of octahedra in the bond-disproportionated phase of rare-earth nickelates
LINAC	linear accelerator, essential part of a synchrotron facility
LNO	$LaNiO_3$

LSAO	LaSrAlO$_3$
LSAT	[LaAlO$_3$]$_{0.3}$ × [Sr$_2$AlTaO$_6$]$_{0.7}$
MIT	metal-to-insulator transition
MLFT	multiplet ligand field theory
NGO	NdGaO$_3$
NNO	NdNiO$_3$
pc	pseudocubic
PGM	plane grating monochromator, essential element of a soft x-ray beamline and RIXS spectrometer
PLD	pulsed laser deposition
PNO	PrNiO$_3$
REXS	resonant elastic x-ray scattering
RIXS	resonant inelastic x-ray scattering
RXS	resonant x-ray scattering, *i.e.* resonant elastic and inelastic x-ray scattering
***R*NiO$_3$**	rare-earth nickelates with with R = La - Lu or Y
SB	short bond (*c.f.* long bond)
SDW	spin-density wave, metallic AFM with weak sub-lattice magnetization
SL	superlattice, periodic structure of at least two different materials
SOC	spin-orbit coupling
STEM	scanning transmission electron microscopy
STO	SrTiO$_3$
TM	transition metal
TMO	transition metal oxide
uc	unit cell
VLS	variable line spacing, plane grating used in the soft x-ray range
XAS	x-ray absorption spectroscopy
XRD	x-ray diffraction
XRR	x-ray reflectivity

Introduction

Complex transition metal oxides (TMOs) host a plethora of electronic
and magnetic phases arising from strongly-coupled spin, charge, orbital,
and structural degrees of freedom, that can lead to unusual magnetic,
multiferroic, and thermoelectric properties, metal-to-insulator transi-
tions (MITs), and high-temperature superconductivity. The unprece-
dented functionalities offered by TMOs could unleash a revolution in
modern technology for a variety of applications ranging from new con-
cepts for energy storage to next-generation electronic devices. In par-
ticular, the diverse magnetism observed in these compounds offers in-
triguing prospects for the post-silicon area, as many TMOs show exotic
forms of magnetism, such as spin-density waves or quantum magnetism.
The intriguing electronic and magnetic phenomena observed in TMOs
represent a direct manifestation of quantum mechanics at a macroscopic
level. Therefore this material class is often referred to as *quantum ma-
terials*. In fact, one of the oldest magnetic materials known to mankind
— magnetite with chemical composition Fe_3O_4 — is a representative
example of this group of materials. Magnetite has been used by humans
for millennia, but its ferrimagnetism can only be explained quantum
mechanically. Moreover, the nature of the charge order which accom-
panies the magnetism is still debated today [1].

   While all materials (including common metals, conventional semi-
conductors, ...) are ultimately governed by the rules of quantum me-
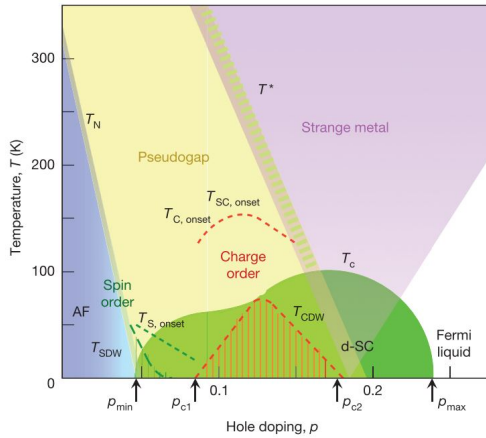chanics, most TMOs offer the possibility to make quantum effects "visi-

1

Figure 1: The phase diagram of holde-doped high-T_c cuprates, where a plethora of phases can be identified. The schematics of this phase diagram prevails to most unconvetional superconductors. Among others, we emphasize the indisputable role of magnetic fluctuations. The Fig. is from Ref. [2].

ble". Thereby, quantum effects, such as electron correlations, spin-orbit coupling, and resulting electron-entanglement, directly determine the macroscopic response of the material. The importance of the electron correlations governed by the Coulomb interactions has manifested itself in the discovery of so-called Mott-Hubbard insulators where in contrast to conventional band insulators (like $SrTiO_3$ with an electron configuration of $3d^0$) the electron-electron correlations can cause insulating states in systems with partially filled d bands at the Fermi level (*e.g.* $LaTiO_3$, $3d^1$ or $LaVO_3$, $3d^2$). The Mott-Hubbard physics are highly relevant for the understanding of a fascinating macroscopic quantum effect — high-temperature superconductivity in layered cuprates systems, such as $La_{2-x}Ba_xCuO_4$ or $YBa_2Cu_3O_{7-x}$ [3, 4]. These cuprates become superconducting below a transition temperature T_c that lies well above the boiling temperature of liquid nitrogen. Therefore these systems are often referred to as high-T_c cuprates, as conventional phonon-mediated superconductors are limited to $T_c \lessgtr 40\,K$ at ambient pressure. Interestingly, the rich phase diagram of hole-doped cuprates (Fig. 1) displays phenomena that are universal to most unconventional superconductors and therefore serves as a platform to deduce common features of the superconducting state. As one can glean from the phase diagram, the superconducting regime appears upon electron or hole doping from an antiferromagnetic Mott insulating state [2] suggesting the importance of magnetic (or spin) fluctuations for an alternative superconducting pairing mechanism. Intriguingly, the superconducting regime is in close proximity to a variety of competing states, ranging from insulating to strange-metal behavior. To further test the universality of these characteristics, substantial research attention moved from high-T_c cuprates towards other TMOs. In particular, researchers were interested in systems that are similar, *e.g.* isostructural and isovalent, to the cuprates as these analogues could help to distill the essential prerequisites for superconductivity. In this thesis, we will focus on two of these "auxiliary" TMO compounds comprising Ni and Ru ions. Both material

systems can become superconducting under specific conditions. In addition, many fascinating other phases are available in close proximity to the superconducting state. Besides the motivation to compare these materials to the high-T_c cuprates, and most importantly, nickelates and ruthenates became huge research fields on their own, due to their rich physics and unusual properties ranging from strange-metal behavior to unconventional types of magnetism. We will study the rare-earth nickelates of composition RNiO$_3$ (R=rare-earth ion) and the single-layer ruthenate Ca$_2$RuO$_4$.

Let us start considering the rare-earth nickelates to illustrate how electron correlations and electronic transitions can give rise to possible functionalities in TMOs. RNiO$_3$ show fascinating quantum phenomena such as a MIT [6–11], hydrogenation-induced quantum phase transitions [12–15], bad metal transport [16], and a broad-temperature-range thermistor behavior [17]. These peculiarities of RNiO$_3$ have been exploited for electronic and Mott-tronic applications such as current sensors [14], logic devices [12], bio-sensors [13], energy converters [18], etc.

A first indication for the pronounced electron correlations in TMOs and its connection with the rich properties and functionalities can be gleaned from the periodic table of elements and structural considerations. The group of TMs are given in the section of the periodic table of elements in Fig. 2 (a). We have highlighted the two elements Ni and Ru, which constitute the central part of the TMOs discussed in this thesis. The common feature of TM ions in quantum materials is a partially filled d electron valence shell[1] with inherent strong electron correlations, as d orbitals are more localized compared to s or p shells. Additionally, we point out that d orbitals have a geometric shape deviating from the sphere of s orbitals, and consequently, the degree of orbital overlap for neighboring ions is very susceptible to modifications of the crystal lattice. Let us consider one of the sim-

---

[1]Note that among others Cu and Zn in elemental form do not have a partially filled d electron shell. Nevertheless, the oxidation states Cu^{2+} or Cu^{1+}, which can be found in oxide materials, host d^n configurations with $n \neq 10$.
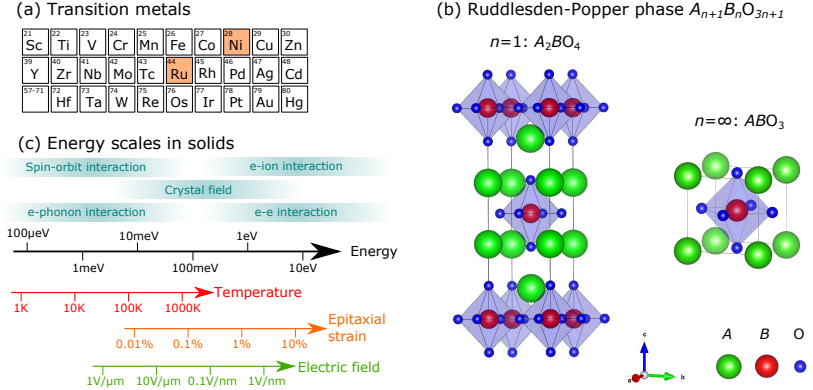
Figure 2: (a) Excerpt of the periodic table of elements. The transition metals (TMs) and their corresponding ions are characterized by a partially filled d electron shell. We have highlighted the two elements, that will be discussed in detail in this thesis. (b) Crystal structures for the two end members of the Ruddlesden-Popper series $A_{n+1}B_n O_{3n+1}$. For all members of this series, the TM ion (B, shown in red) is surrounded by six oxygen (O, shown in blue). In addition, the unit cell comprises the A site cations (A, shown in green, typically rare-earth elements). These layered perovskite structures are very common among TMO compounds, where n quantifies the number of adjacent BO_6 planes. The two materials discussed in this thesis, Ca_2RuO_4 and $RNiO_3$, are prototypical examples for the two end members of the Ruddlesden-Popper series with $n = 1$ and $n = \infty$, respectively. (c) Energy scales present in solids as well as caused by external perturbations. It is evident, that the energies of external perturbations and internal forces overlap. Therefore it is possible to modulate the properties of TMOs using different stimuli and thermodynamic variables. Panel (c) follows Ref. [5].

plest and most common structural motifs of ternary transition-metal oxides, the layered perovskite Ruddlesden-Popper structure shown in Fig. 2 (b). The two end members of the Ruddlesden-Popper phase $A_{n+1}B_nO_{3n+1}$ represent the crystal structure for the two materials discussed in this thesis, with $n = 1$ and $n = \infty$ for Ca_2RuO_4 and RNiO$_3$, respectively. For both cases the TM ion is surrounded by six oxygen ions, forming the TM-O$_6$ octahedra which are the fundamental building block of many TMOs, including RNiO$_3$ and Ca_2RuO_4. Different mechanisms such as for example the size of the A site cation can affect the shape of the TM-O$_6$ octahedra. In particular distortions, which in first approximation can be described by collective tilts and rotations of rigid TM-O$_6$ octahedra [19,20], result in possibly anisotropic TM-O-TM bond angles that deviate from the cubic 180° ones. This has important consequences for the electronic and magnetic properties, since, for example, electronic bandwidths are reduced to the extent that MITs are observed. Furthermore, reduced overlap of TM-d and oxygen-p orbitals can strongly modify the magnetic superexchange and therewith the macroscopic magnetic order.

The profound effect of even minor structural modifications on the macroscopic response in TMOs reveals several competing ground states, that are separated only by a small energy difference. On the one hand this reflects the subtle balance between different internal forces at play, which was already inferred from the phase diagram of the high-T_c cuprates. On the other hand, competing energy scales manifest themselves in a large susceptibility to external perturbations and/or thermodynamic variables, such as temperature, electric field, or epitaxial strain. Therefore, external control variables provide a powerful tool to disturb the intrinsic energy balance in TMOs, such that nonequilibrium and exotic states can be accessed. We can then use these metastable states to gain insights into the relevant energy scales of a specific system or to tailor specific properties on demand [21,22]. In Fig. 2 (c), we compare several intrinsic energy scales of a solid with relevant energies

for external perturbations, such as epitaxial strain and electric fields. The similarity of both energy ranges enables an effective control of the material by external variables to further enrich potential functionalities of TMOs.

In this thesis, we exemplify and exploit the strong structure-property relationship in TMOs using different material systems and the perturbation approaches introduced in Fig. 2 (c): heterostructuring, temperature changes, and electric fields. We will see that the perturbation methods presented here are strongly connected to the interplay of electronic degrees of freedom and collective tilts and rotations of the TM-O_6 octahedra. We point out that the novel phases stabilized by means of heterostructuring and electrical current do not have a bulk or equilibrium analogue, thereby offering the possibility to investigate new and exotic states of matter. In all studies presented in this thesis, we use advanced light scattering experiments to access the competing energy scales in the metastable phase and to extract microscopically relevant parameters. Especially, x-ray-based scattering experiments offer the possibility to probe the electronic structure in TMOs, and consequently, give valuable insight into the rich physics of TMOs and help to develop perspectives to design materials with properties on demand[2].

First, we focus on epitaxially-grown heterostructures that comprise a layered sequence of a TMO and a nonmagnetic band insulator. Thereby one can impose boundary conditions on a quantum material in a very controlled fashion. Recent advances in ablation techniques facilitate the growth of thin-film structures with high-quality, that can be compared to the purity and cleanliness of semiconductors [23]. Consequently, heterostructuring offers a clean way to tune the properties of TMOs. The main control variables in thin films and heterostructures are epitaxial

---

[2]Interestingly, this year we celebrate 125 years since the discovery of x-rays by W.C. Röntgen. His groundbreaking observation had an immediate and revolutionizing impact on medicine and physics, and even today major fields in several disciplines, such as physics, biology, material science etc. rely on x-ray-based research. We will discuss the generation and use of x-rays to investigate TMOs in Chapter 2 of this thesis.

strain (choice of substrate type and cut), spatial confinement (choice of layer thickness), and mismatch of the electronic and/or magnetic structure of the two materials across the interface. These interface effects, *e.g.* charge transfer, can give rise to properties not observed in the bulk of the material comprising the heterostructures. Examples of emergent phenomena in oxide heterostructures include a MIT without structural transition in epitaxially grown VO_2 [24], interface superconductivity between band-insulating oxides [25,26], or room-temperature magnetoelectric multiferroicity in artificially designed structures [5,27]. More specifically, we use heterostructuring to tune the properties of a prototypical $3d$ TMO — the rare-earth nickelates $RNiO_3$ which host a unique antiferromagnetic order without analogue in other oxide materials. After developing a spin model for the bulk system, we study the modulated order parameters in heterostructures using resonant x-ray scattering techniques. In particular, we probe the complex magnetic order in these compounds by quantifying the exchange interactions in a novel spin-density wave phase. Moreover, we illustrate ways to epitaxially control the transition temperature of the MIT and the antiferromagnetic (AFM) state using specific confinement geometries and interface effects.

Second, we proceed to continuously and dynamically tune the properties of TMOs, which is not possible by *ex-situ* methods, such as heterostructuring or doping, but facilitated for example by the application of electric fields, currents or uniaxial strain [28]. In particular, we show how the control of macroscopic properties by electric current is of high relevance to test quantum materials for *in-operando* device operations [29]. Field and current effects in TMOs include gating-induced MITs in VO_2 thin films [30–32], electric-field-control of superconductivity in ultra-thin cuprate thin films [33], or modulated double-exchange interactions in ferromagnetic junctions [34]. Here, we focus on a $4d$ TMO, namely Ca_2RuO_4, which shows tunable electronic properties triggered by electrical currents due to a spin-orbit coupling enhanced

structure-property relationship. We will use Raman light scattering to probe transitions into nonequilibrium metallic and semimetallic states.

This thesis is organized as follows:

Chapter 1: *3d* and *4d* transition metal oxides

First, we introduce general concepts of TMOs and show how electronic correlations manifest themselves in the macroscopic response of this material class. We proceed to discuss important peculiarities of the systems investigated in this thesis. Starting from the exciting bulk properties of $R\text{NiO}_3$, we see how different ordering phenomena can be modified by means of heterostructuring. We mainly focus on a modulated bond order amplitude and the crossover from noncollinear to colllinear magnetic order as a function of layer thickness. In the case of Ca_2RuO_4, we discuss important magnetic and structural properties and their interconnectivity to drive multiple transitions in this system. Then we review all effects of the metastable state obtained by applying an electric DC current and discuss important aspects of the *in-situ* control of this state in Ca_2RuO_4.

Chapter 2: Light scattering from solids

This Chapter is dedicated to the basics of light scattering from solids, which is the main method of investigation used in this thesis. After reviewing and developing important aspects of light-matter interactions, we will focus on the details of resonant inelastic x-ray scattering (RIXS) and Raman light scattering both from a theoretical and experimental point of view. The last part of the Chapter deals with different approaches for the analysis of the measured spectra.

Chapter 3: RIXS study of bond order and spin excitations in $R\text{NiO}_3$

In Chapter 3, we use high-resolution RIXS at the Ni L_3 edge to simul-

taneously investigate high-energy interband transitions characteristic of Ni-O bond ordering and low-energy collective excitations of the Ni spins in the rare-earth nickelates $R\text{NiO}_3$ (R = Nd, Pr, La). With the support of calculations based on a double-cluster model we quantify bond order amplitudes for different thin films and heterostructures and discriminate short-range bond order fluctuations from long-range static order. Moreover, we investigate magnetic order and exchange interactions in bulk-like and spatially confined $R\text{NiO}_3$ slabs by probing dispersive magnon excitations. First, we study the bulk case and develop a complete site-selective description of the magnetism in $R\text{NiO}_3$, where the exchange interactions are quantified for the first time. Second, we expand this model and further study the superlattices (SLs) with modified bond and magnetic order. Our study of SLs grown in the [001] direction of the perovskite structure reveals a robust non-collinear spin spiral magnetic order with dispersive magnon excitations, which are essentially unperturbed by bond order modulations and spatial confinement. In contrast, we find magnons with flat dispersions and strongly reduced energies in SLs grown in the $[111]_{pc}$ direction that exhibit collinear magnetic order. Our study provides direct insight into the magnetic dynamics and exchange interactions of bulk-like and spatially confined rare-earth nickelates and demonstrates that RIXS can serve as a site-selective probe of several collective excitations in these and other materials.

Chapter 4: Interplay of structure, bond and magnetic order in NdNiO$_3$ thin films

Here, we use a combination of electrical transport measurements, scanning transmission electron microscopy (STEM), resonant elastic x-ray scattering (REXS), and density functional theory (DFT) to investigate the evolution of the MIT and AFM transition in NdNiO$_3$ films as a function of film thickness and NdGaO$_3$ substrate crystallographic orientation. We find that for two different substrate orientations, or-

thorhombic [101] and [011], modifications of the NiO_6 octahedral network are key for tuning the transition temperature T_{MIT} over a wide temperature range. A comparison of films of identical thickness reveals that growth on [101]-oriented substrates generally results in a higher T_{MIT}, which can be attributed to an enhanced bond disproportionation as revealed by the DFT+U calculations, and a tendency of the [011]-oriented films to form structural defects and nonequilibrium phases. In addition, we study the interplay of the bond order amplitude and the magnetic order. The magnetic transition temperature T_N also sensitively depends on the substrate facet and the $NdNiO_3$ layer thickness. The amended bond disproportionation therefore has important implications for the magnetic state, which can be qualitatively different from the bulk, and for the exchange interactions. Our results provide insights into competing interactions at microscopic length scales and give new perspectives for the epitaxial control of macroscopic phases in nickelate heterostructures.

Chapter 5: Raman scattering from current-stabilized nonequilibrium phases in Ca_2RuO_4

In Chapter 5, we use Raman light scattering to study the current-stabilized nonequilibrium semimetallic and metallic phases in Ca_2RuO_4. By determining the local temperature through careful analysis of the Stokes and anti-Stokes intensities, we find that Joule heating can be completely avoided by supplying sufficient cooling power in a helium-flow cryostat and that the current induces the semimetallic state without inducing any significant heating. We further investigate the current-induced semimetallic state as a function of temperature and current. We confirm the absence of long-range antiferromagnetic order and identify a substantial Fano broadening of several phonons, which suggests coupling to charge and orbital fluctuations.

Chapter 1

$3d$ and $4d$ transition metal oxides

To understand the peculiarities of $3d$ and $4d$ TMOs and the importance of electronic correlations in these materials, we first glance at conventional band insulators and normal metals. Using band theory and the periodic potential of the crystal lattice, it is possible to obtain a description of the electronic structure of crystals and deduce fundamental properties including the macroscopic responses of a material. In this approximation the solid is described by noninteracting electrons moving in a periodic potential arising from the lattice of ions. Band theory introduces fundamental characteristics of a material system such as energy bands with allowed states, density of states and energy gaps, which can be inferred for example from electrical transport or optical conductivity measurements. Depending on the filling of the bands by noninteracting electrons (or equivalently holes), one can broadly categorize the materials into two groups: normal metals and band insulators. The former have partially filled bands close to the Fermi energy enabling electron/hole movement at infinitesimal excitation energy. In the case of band insulators, such as diamond, some bands are com-

pletely filled and separated by a bandgap from the next higher one, thereby preventing electron/hole movement. This basic schematics allows us to extract important properties of many materials, however it completely fails to describe TMOs even on the most basic level [35–37]. Let us consider MnO as a prototypical example of a TMO. Following the band picture MnO is expected to be a metal [38], however insulating behavior is found in experiments [39]. The conventional band description is lacking the Coulomb repulsion and resulting correlation of valence electrons, which is essential for the materials discussed in this thesis and in general for all TMOs.

To explicitly include the Coulomb repulsion and resulting electron correlations, *i.e.* the complex influence of a single electron on its neighbors, we move away from band theory and use the nondegenerate Hubbard model [40–42]. Here the solid is approximated by a lattice of interacting sites comprising one orbital each. The Coulomb repulsion between electrons is directly incorporated into the model when two electrons occupy the same lattice site. The Hamiltonian for the nondegenerate Hubbard model is written as [40–42]

$$\mathcal{H} = -t \sum_{ij,\sigma} c_{i\sigma}^{\dagger} c_{j\sigma} + U \sum_{i} n_{i\uparrow} n_{i\downarrow} \tag{1.1}$$

where t is the hopping matrix element and U the Coulomb repulsion of two electrons residing on the same lattice site. The electron density is given by $n_{i\sigma} = c_{i\sigma}^{\dagger} c_{i\sigma}$, with the creation (annihiliation) operator $c_{i\sigma}^{\dagger}$ ($c_{i\sigma}$) of an electron with spin σ at site i. The first part of $\mathcal{H}$ reflects the tight-binding approach, where the solid is described by isolated atoms (or ions) with localized atomic levels. Tunneling events between atoms can happen, as an electron hops from one potential well to another one. Depending on the hopping activity t, the isolated atoms hybridize and form bands. We use the bandwidth $W = 2zt$ to quantify the degree of itineracy of the electrons, where z gives the number of nearest neighbors. The second term of $\mathcal{H}$ parametrizes the Coulomb repulsion

of two electrons at the same orbital at a single lattice site, which ul-
timately gives rise to electron correlations, electron entanglement, etc.
We realize that the system approximated by $\mathcal{H}$ is insulating for $U \gg W$
due to the electron-electron interaction even though it is predicted to
be metallic in the conventional band picture. Such kind of insulator
is called Mott-Hubbard insulator. Its insulating nature is determined
by strong correlations (U), in contrast to conventional band insulators,
which follow from the periodic potential of the lattice. We will see
in Section 1.1 that the electron correlations are particularly strong for
the valence electrons of the d shell. Before moving to the magnetic
properties, we can deduce another important feature of many TMOs
from equation 1.1. As previously mentioned a material is insulating
for $U \gg W$, whereas for $U = 0$ the systems shows always metallic
behavior in this model (tight-binding approach). Consequently, we can
expect a crossover between insulating and metallic regime as a function
of U. That is a metal-to-insulator transition (MIT), and in this case
called Mott transition. MITs are observed in many different TMOs and
are subject to intensive research in particular due to their potential for
applications. Both of the systems discussed in this thesis, $R\mathrm{NiO_3}$ and
$\mathrm{Ca_2RuO_4}$, host MITs close to or above room temperature.

Pronounced electron correlations do not only manifest themselves
in the fundamental state of TMOs, but also profoundly influence the
magnetic behavior. In fact, correlations are the reason for the strong
magnetism and give rise to manifold spin states observed in TMOs
[35, 43, 44]. We describe the magnetic state by an effective Hamilto-
nian, the Heisenberg Hamiltonian

$$\mathcal{H}_{\mathrm{eff}} = J \sum_{ij} \mathbf{S_i} \cdot \mathbf{S_j} \tag{1.2}$$

with the exchange coupling $J = \frac{2t^2}{U}$ and spins $\mathbf{S_i} = (S_i^x, S_i^y, S_i^z)$ and
$\mathbf{S_j} = (S_j^x, S_j^y, S_j^z)$ residing on lattice sites i and j, respectively. $\mathcal{H}_{\mathrm{eff}}$
can be readily deduced from the Hubbard Hamiltonian in equation 1.1

assuming strong interaction ($U \gg t$) and one electron per lattice site ($n = 1$). The Heisenberg Hamiltonian describes the nearest-neighbor exchange interaction of localized quantum spins. The exchange coupling J is positive (negative) in the case of antiferromagnetic (ferromagnetic) coupling. The dominant exchange interaction in TMOs is the so-called *superexchange interaction* which describes the magnetic coupling of two paramagnetic TM ions via an intermediate nonmagnetic oxygen ion. In the case of ↑↓ arrangement of neighboring TM spins, effective delocalization of electrons via second-order virtual hopping processes decreases the kinetic energy. This delocalization is not possible for ferromagnetic ordering due to the Pauli exclusion principle. Therefore, the Heisenberg Hamiltonian predicts an antiferromagnetic (AFM) ground state for magnetic Mott insulators. This is confirmed by experimental observations, where most of the Mott insulators are found to be AFM, whereas ferromagnetism often coincides with metallic behavior. An intriguing exception is a metallic AFM with weak sub-lattice magnetization, found in heterostructures comprising $R\mathrm{NiO_3}$. The magnetic phase is then called a spin-density wave and can be explained in terms of Fermi surface nesting. In addition to the AFM state, we point out that $\mathcal{H}_{\mathrm{eff}}$ describes the lowest energy excitations of a magnetic system, *i.e.* spin waves. We will later analyze spin excitations measured by inelastic x-ray scattering with a Heisenberg-like Hamiltonian.

From this warm-up in electronic correlations, we realized the importance of the on-site Coulomb interactions to understand the appealing and exotic physics observed in TMOs. In the following we will temporarily ignore the periodic nature of the solid and focus on isolated transition metal ions to review the characteristics of the d electron shell. This atomic picture will guide us to important differences between $3d$, $4d$, and $5d$ TM ions.

1.1 Isolated transition metal ions

In TMOs the partially filled d electron valence shell participates in the formation of chemical bonds. Additionally, the d shell is quite localized to the ionic core and consists of spatially anisotropic orbitals. In particular, 3d orbitals extend only to a radius of $\approx$ 0.5 Å [37, 45, 46]. The localization increases the electron-electron interaction and is therefore the prime reason for the strong correlations observed in 3d materials such as RNiO$_3$. 4d and 5d orbitals are still quite localized however to a lesser extent, as the effective radius of d electrons increases from 3d to 5d elements. Especially 5d electrons have larger radii than 3d ones and correspondingly larger covalency with surrounding ions resulting in larger bandwidths. Simultaneously the effective Hubbard repulsion energy decreases, as does the Hund's rule energy. Therefore U decreases from $\approx$ 3 - 6 eV in 3d to $\approx$ 1.5 - 2 eV in 5d ions.

Correlations decrease from 3d to 5d, but the relativistic spin-orbit coupling (SOC) becomes stronger for heavier elements. The atomic SOC constant ζ scales with the atomic number Z following $\zeta \propto Z^4$. SOC is described by the following Hamiltonian

$$\mathcal{H}_{\mathrm{SOC}} = \sum_i \zeta_i \mathbf{l}_i \cdot \mathbf{s}_i = \lambda \mathbf{L} \cdot \mathbf{S} \tag{1.3}$$

where we imply the LS (also called Russell-Sauders) coupling scheme and the renormalized SOC constant used for solids $\lambda = \zeta/2s$. This coupling scheme presumes that the total spin $\mathbf{S}$ and orbital $\mathbf{L}$ momentum of the atom are given by the sum of individual electron spins $\mathbf{s}_i$ and the orbital moments $\mathbf{l}_i$, respectively: $\mathbf{S} = \sum_i \mathbf{s}_i$ and $\mathbf{L} = \sum_i \mathbf{l}_i$. $\mathbf{S}$ and $\mathbf{L}$ then couple to the total momentum $\mathbf{J} = \mathbf{S} + \mathbf{L}$ of the atom. This coupling scheme holds for all 3d elements, whereas a different picture needs to be used for 5d and some of the 4d elements. In particular 4d elements lie between the LS and so-called jj coupling scheme. The latter scheme assumes a strong individual coupling of spin and orbital momentum to

the total momentum $\mathbf{j}_i = \mathbf{s}_i + \mathbf{l}_i$ for every electron. The total momentum of the atom is given by $\mathbf{J} = \sum_i \mathbf{j}_i$. We will later see (Fig. 1.1) how different coupling schemes are reflected in the electronic structure and how they manifest themselves in the magnetic properties of TMOs. For now we will concentrate on the varying values of the SOC constant for different d electron shells. For light $3d$ elements, such as Ti^{4+}, the SOC constant is of the order $\lambda \approx 20\,meV$. The SOC increases for heavier $3d$ elements, for example Ni^{2+} comprises $\lambda \approx 80\,meV$ [45, 47][1]. For $5d$ elements SOC is substantially stronger (up to $0.5\,eV$). Thereby λ becomes comparable to the hopping parameter t and the Hubbard repulsion U, and in turn SOC dictates many properties of $4d$ and $5d$ systems [48, 49].

To sum up this Section, we have used the atomic picture to develop the following trends from $3d$ to $4d$ and $5d$ TMOs: an increase in SOC and a decrease in electronic correlation (U). We emphasize that strong electron correlations dominate the physics in $3d$ materials, such as $R\mathrm{NiO_3}$, whereas SOC can be treated perturbatively or even be neglected. In contrast, correlations and SOC often have to be treated on equal footing in the description of $4d$ materials, for example in $\mathrm{Ca_2RuO_4}$. In the next step, we will leave the atomic level and include the neighboring oxygen ions into the description of TMOs.

1.2 The role of oxygen in TMOs

1.2.1 Crystal field effects

Recalling the $\mathrm{TM\text{-}O_6}$ octahedra as the building blocks of many TMOs [see for example the perovskite phase in Fig. 2 (b)], it is evident that the oxygen ions play a central role in the physics of TMOs, because they are the next nearest neighbors of the TM ion. In the cases of $R\mathrm{NiO_3}$

---

[1]SOC in $3d$ TMOs can often be neglected not only because it is small, but also because the influence of a low-symmetry crystal field can cause a quenching of the angular orbital momentum (see Section 1.2.1 and Fig. 1.1).
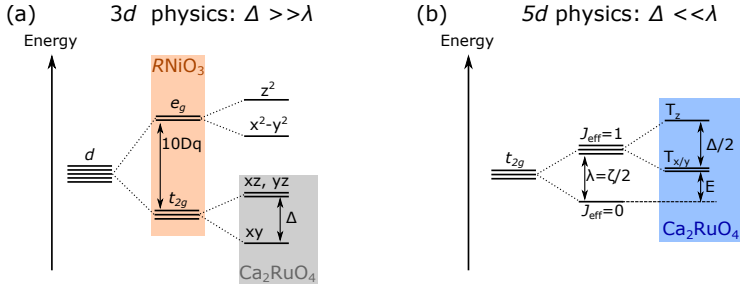
Figure 1.1: Electronic structure for dominating (a) crystal field effects of the TM-O_6 octahedra ($3d$-like), and (b) spin-orbit coupling ($5d$- and $4d$-like). (a) The spherical symmetry of a free atom or ion is lowered to O_h symmetry due to the octahedral coordination by the oxygen ions. The d orbitals are split into e_g and t_{2g} subsets. This is the case for $RNiO_3$ (orange box). Further splitting is observed for tetragonally compressed (or elongated, not shown here) TM-O_6 octahedra, where the deformation of the octahedra is parametrized by Δ. In this framework the electronic structure of Ca_2RuO_4 would be given by the gray box. (b) For dominating SOC, the t_{2g} subset is split into $J_{\text{eff}} = 0$ singlet and $J_{\text{eff}} = 1$ triplet states, separated by λ. The triplet state is split into T_x/T_y doublet and T_z singlet due to the tetragonal compression present in Ca_2RuO_4. The energy gap E between the nonmagnetic $J = 0$ singlet and the magnetic T_x/T_y doublet is therefore lowered by Δ and eventually overcome by the exchange energy. We will discuss in Section 1.4.1, that the condensation of the magnetic states into the $J = 0$ ground state results in magnetic long-range order via the so-called "excitonic magnetism" and that Ca_2RuO_4 should be described in the strong SOC limit, as indicated by the blue box, while the gray box from panel (a) can be discarded. The Fig. follows Refs. [50, 51].

and Ca_2RuO_4, each TM ion is surrounded by an O_6 octahedron, which lowers the spherical symmetry of an isolated atom/ion due to crystal field effects. In first approximation the oxygen ions may be considered as point charges that evoke a crystal field and therefore impose the octahedral (O_h) symmetry onto the TM ion. The basics of this effect can be understood in terms of of point charges but it is crucial to include hybridization effects between the d orbitals of the TM ion and the $2p$ orbitals of the oxygen, especially as the covalency contribution exceeds the effects from point charges [35, 45, 52, 53]. Following the conventions of group theory, the electronic structure governed by crystal field effects is shown in Fig. 1.1 (a) for both RNiO$_3$ and Ca_2RuO_4. The Ni ions in RNiO$_3$ are exposed to a standard octahedral crystal field (O_h) which leads to a splitting of the d orbital into e_g and t_{2g} subsets. The energy difference between e_g and t_{2g} manifold is called crystal field splitting $10Dq$ [36, 54]. For RNiO$_3$, a crystal field splitting of $10Dq \approx 1\,\mathrm{eV}$ provides a valid description of the electronic configuration of the Ni^{3+} ions. Additional tetragonal elongation or compression of the TM-O$_6$ octahedra (denoted Δ) leads to a further lowering of symmetry and more splittings. Tetragonal compression is found in Ca_2RuO_4, which effectively lowers the d orbitals energetically with components along the direction of compression, *i.e.* in the z direction. In Ca_2RuO_4 the crystal field splitting and tetragonal compression are $10Dq \approx 4\,\mathrm{eV}$ and $\Delta \approx 150\,\mathrm{meV}$, respectively [50, 55]. The increased value of $10Dq$ for $4d$ compared to $3d$ ions can be traced back to the larger electron radius from $3d$ to $4d$ and $5d$ elements. Consequently, the $p - d$ hybridization becomes larger for later elements, which in turn enhances the covalency contribution to the crystal field and results in increased $10Dq$ values for $4d$ and $5d$ elements [52]. From a broader perspective, we realize that the electronic structure, in particular orbital degeneracy and spin states, of TMOs are strongly connected to the local symmetry, therefore we can naturally expect to tune the electronic properties by changing the symmetry of the crystal. We will exploit exactly this in Chapters 3

and 4 where the properties of $R\mathrm{NiO_3}$ are modified by means of targeted heterostructuring.

As crystal fields break the rotational invariance, implications for the SOC are expected. In an e_g system such as the nominal d^7 configuration for $\mathrm{Ni^{3+}}$ in $R\mathrm{NiO_3}$, the orbital momentum is quenched due to $\langle e_g|\mathbf{l}|e_g\rangle = 0$. Consequently, $\mathbf{S}$ and $\mathbf{L}$ are not good quantum numbers anymore to classify e_g systems, and SOC does not act on these states in first order. Even though there might be higher-order effects resulting in sizable modifications, such as single-site magnetic anisotropies, we can safely use the electronic configuration in Fig. 1.1 (a), orange box, for the description of $R\mathrm{NiO_3}$. The situation is quite different for t_{2g} systems such as $\mathrm{Ca_2RuO_4}$, where the orbital moment is nonzero and SOC can split these states in first order. We recall that SOC strongly increases for $4d$ and $5d$ elements, which can lead to a nontrivial situation with competing energy scales. In that case the electronic structure strongly depends on the relative strength of the tetragonal compression and the SOC. For dominating SOC, the schematics shown in panel (b) of Fig. 1.1 is more appropriate to describe the electronic state of $\mathrm{Ca_2RuO_4}$. Here the t_{2g} subset is split into a $J_{\mathrm{eff}} = 0$ singlet and a $J_{\mathrm{eff}} = 1$ triplet, separated by λ. Tetragonal compression, parametrized by Δ, acts on the J_{eff} states and splits the triplet state into a lower lying T_x/T_y doublet and a higher lying T_x singlet. Indeed, recent theoretical [56–58] and experimental [50,59] studies point towards a strong SOC picture to appropriately describe $\mathrm{Ca_2RuO_4}$. Consequently the configuration developed on the basis of $3d$ physics and strong crystal field effects [1.1 (a)] should be discarded for $\mathrm{Ca_2RuO_4}$.

1.2.2 Mott-Hubbard vs. charge transfer insulators

As next-nearest neighbors of the TM ions, the oxygen ions change the local symmetry and separate the individual TM ions. Therefore the TM ions can mainly interact with each other via the oxygen ions, following the direct connection of the form TM-O-TM. Substantial (virtual)

electron hopping between oxygen and TM ions results from the strong
overlap between $3d$ and $2p$ orbitals of the TM ion and the oxygen, while
direct $d-d$ hopping, from one TM ion to another one, can mostly be
ignored. This has important consequences on the magnetic dynamics,
as magnetic superexchange interactions are mediated via the oxygen.
The key role of oxygen is particularly evident in perovskite materials
such as $LaMnO_3$ [60], the parent compound of high-T_c superconduc-
tors La_2CuO_4 [61], $RNiO_3$ and Ca_2RuO_4, but it can also be extended
towards rock salt structures, *e.g.* NiO [62]. It is therefore necessary
to explicitly include the oxygen $2p$ orbitals in the Hubbard model of
equation 1.1 to deduce a better understanding of TMOs. This leads to
the $d-p$ model, which constitutes the basis for the famous Zhang-Rice
singlet found in high-T_c cuprates [63–65]. Assuming a d^n configuration
of the TM ion, the hybridization with oxygen formally leads to two pos-
sibilities for the lowest energy excitations, as shown in Fig. 1.2, panels
(a) and (b). The first option is $d^n + d^n \to d^{n-1}d^{n+1}$ with an energy
cost of $\Delta E = U$ resulting from the Coulomb repulsion of two electrons.
This state corresponds to the Mott-Hubbard insulator, which we have
discussed in the beginning of this Chapter. The other one is a so-called
charge transfer excitation, where CT stands for *charge transfer*. In this
case, an electron gets transferred from the oxygen $2p$ shell to the TM
d shell: $d^n p^6 \to d^{n+1} p^5$ with an energy cost $\Delta E = \Delta_{CT}$, where p rep-
resents the oxygen ligand $2p$ orbitals. In this case the lowest excitation
is not $d-d$ like, but actually has $p-d$ character, as an electron gets
transferred from the oxygen p shell to the TM d shell. The smaller
energy cost of the lowest excitation determines the nature of the insu-
lator: $U > \Delta_{CT}$ gives a charge transfer insulator, whereas $U < \Delta_{CT}$
leads to the Mott-Hubbard insulator. Different TM ions are arranged
and classified according to Δ_{CT} and U in the Zaanen-Sawatzky-Allen
diagram [66]. This programmatic diagram illustrates that only earlier
$3d$ TMOs, comprising for example Ti and V fall into the Mott-Hubbard
class, whereas most oxides with later TM ions are charge transfer in-

sulators. That is because Δ_{CT} is large for early $3d$ elements with low oxidation states. Experimentally Δ_{CT} and U can be determined from $2p$ core-level photoemission spectra [67].

The charge transfer energy Δ_{CT} generally decreases from $3d$ to $4d$ and $5d$. The increasing atomic number Z for heavier elements effectively lowers the energy of the d levels, while the $2p$ oxygen levels mostly remain unaffected due to the sizable distance from the TM nuclei. Consequently the $p - d$ transfer decreases for increasing Z, which results in a generally smaller Δ_{CT} for later TM ions. Importantly besides Z, the oxidation state of the TM ion determines Δ_{CT}. For different oxidation states of the Ru ion, one finds $\Delta_{\mathrm{CT}} = 5\,\mathrm{eV}$, $2\,\mathrm{eV}$, and $1\,\mathrm{eV}$ for Ru^{3+}, Ru^{4+}, and Ru^{5+}, respectively [68]. Note, that the charge transfer energy for Ru^{4+} in $\mathrm{Ca_2RuO_4}$ might be closer to $0\,\mathrm{eV}$ [69], which has been found from fits to XAS spectra. For NiO (Ni^{2+}) a charge transfer gap of $4\,\mathrm{eV}$ [70, 71] was found, while very recent work for Ni^{1+} suggests a Mott-Hubbard-type gap [72].

Importantly Δ_{CT} can even become negative. This is particularly common for high-valence and high-oxidation states, such as $R\mathrm{NiO_3}$. Other examples of negative charge transfer materials with large contribution of oxygen holes are the ferromagnetic metallic compounds $\mathrm{CrO_2}$ and $\mathrm{SrCoO_3}$, and $\mathrm{SrFeO_3}$, which has a spiral magnetic structure. The electron removal and addition spectra for negative charge transfer insulator is shown in Fig. 1.2 panel (c). We realize that already in the ground state one electron is transferred from the oxygen $2p$ level to the d orbital of the TM ion, which led to the notion that the ground state of the materials with $\Delta_{\mathrm{CT}} < 0$ is *self-doped* [73]. The energy gain for this excitation/transfer is given by the energy difference between the top of the ligand band and the bottom of the $3d$ band, and is usually defined as effective charge transfer energy Δ_{eff}. Consequently, Δ_{eff} gives the energy separation of $d^n \underline{L}^0$ and $d^{n+1} \underline{L}^1$ configurations with $\underline{L}$ being an hole residing on the oxygen ligand. Negative charge transfer insulators are often found to host charge or bond disproportionation in the low

energy phase, as the rearrangement of electrons in the extended p shell costs less energy than in the d shell. Precisely this scenario can be found in the $R\text{NiO}_3$ with $\Delta_{CT} = -0.5\,\text{eV}$ [6, 74].

1.3   Rare-earth nickelates $R\text{NiO}_3$

Following the general introduction of TMOs and their basic proper-
ties, we now focus on a prototypical $3d$ correlated oxide: the rare-earth
nickelates $R\text{NiO}_3$ (with $R = \text{La - Lu or Y}$). While $R\text{NiO}_3$ host already
multiple electronic phases in bulk form, the physics in these compounds
can be further enriched by means of heterostructuring. We review im-
portant aspects and characteristics of bulk $R\text{NiO}_3$ and highlight some
novel phases that can be stabilized by heteroepitaxy.

1.3.1   Bulk properties

Nickelate perovskites of composition $R\text{NiO}_3$ are archetypes of correlated-
electron behavior in the vicinity of a Mott MIT [8–11]. The micro-
scopic origin of the MIT and of an unusual AFM state in the insulat-
ing phase have stimulated a great deal of theoretical work over sev-
eral decades [6, 78–83]. New perspectives have recently emerged from
the ability to synthesize thin-film structures with atomic-scale preci-
sion [23, 84, 85] and to probe ordering phenomena in such structures
using Ni L edge resonant x-ray scattering [86, 87].

   All $R\text{NiO}_3$ with $R \neq \text{La}$ show a MIT at a temperature that de-
creases monotonically as a function of increasing rare-earth ionic radius,
which straightens the Ni-O-Ni bonds and enhances the valence-electron
bandwidth (see Fig. 1.3). The MIT is accompanied by a structural
transition [88] from the orthorhombic space group *Pbnm* to monoclinic
$P2_1/n$. LaNiO_3 remains metallic, paramagnetic and within the $R\bar{3}c$
space group at all T. The Ni ions in $R\text{NiO}_3$ have a 3+ valence state re-
sulting in a formally d^7 configuration. Recalling the electronic structure
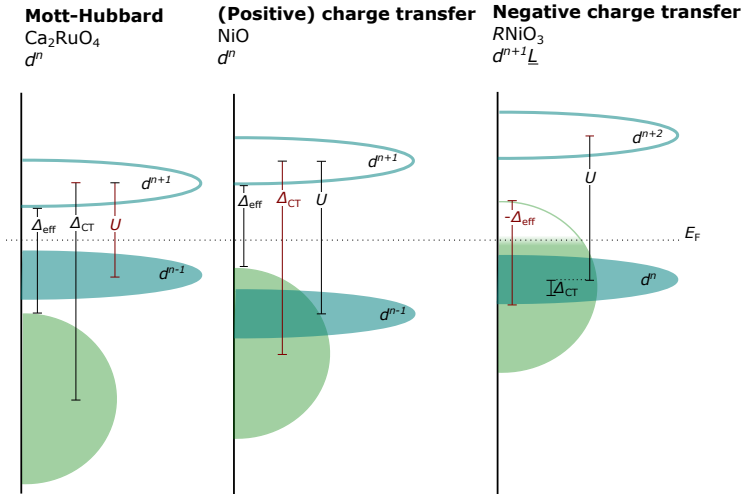
Figure 1.2: The energetics and insulating nature of correlated compounds are illustrated with schematic electron removal and addition spectra. The nominally full oxygen $2p$ bands are shown as broad light green bands. The correlated, narrow d bands are given in blue. The Coulomb repulsion U separates lower and upper Hubbard bands. The charge transfer energy Δ_{CT} gives the energy difference between the middle of the TM d and oxygen $2p$ bands. We further define an effective charge transfer energy Δ_{eff}, between the highest energy of the full oxygen level and the lowest level of the empty d band. The Fermi level is shown with a dashed vertical line and electron removal spectra are shaded in, while electron addition spectra are only outlined. The nature of the ground state wavefunction and material examples are given as well. The Fig. is reproduced following Refs. [75, 76].
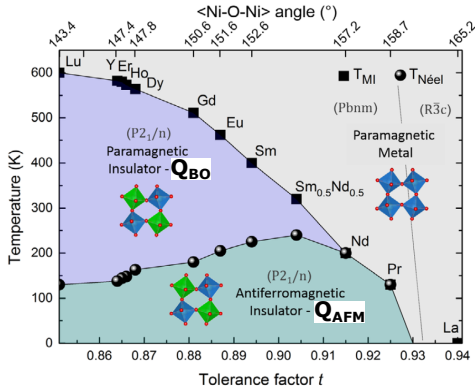
Figure 1.3: Phase diagram of bulk $R\text{NiO}_3$ illustrating metallic (gray), paramagnetic insulating (blue), and AFM insulating (green) phases as a function of tolerance factor t and Ni-O-Ni bond angle. The geometrical tolerance factor is defined as $t = d_{R\text{-O}}/(\sqrt{2}d_{\text{Ni-O}})$, where $d_{R\text{-O}}$ and $d_{\text{Ni-O}}$ are the Ni-O and R-O distances, respectively. The ideal (cubic) perovskite structure from Fig. 2 is realized for $t = 1$. Further details such as the ordering vectors for bond order ($\mathbf{Q}_{\text{BO}}$) and AFM ($\mathbf{Q}_{\text{AFM}}$) are introduced in the text. The Fig. is reproduced with adaptions from [77].

from Fig. 1.1 (a) with $10Dq \approx 1$ eV, the Ni ion would constitute a fully occupied t_{2g} subset, whereas the doubly degenerate e_g orbital hosts one electron. Following the Jahn-Teller [89, 90] or Kugel-Khomskii [91] framework, this configuration would result in an orbitally ordered insulating ground state, which has not been found experimentally. Instead, several theoretical studies suggested that the orbital degeneracy is lifted by charge disproportionation on the Ni site or by ordering of the Ni-O bonds, *i.e.* bond order, for all RNiO$_3$ with $R \neq$ La [74]. Experimental work identified this bond order as a pattern of alternating NiO$_6$ octahedra volumes along the diagonal of the pseudocubic (pc) perovskite structure in the insulating state, which is quantified by the ordering vector $\mathbf{Q}_{\mathrm{BO}} = (^1/_2, ^1/_2, ^1/_2)_{\mathrm{pc}}$ [92, 93]. Different models have been proposed to describe the insulating state and $\mathbf{Q}_{\mathrm{BO}}$. While early studies ascribed the insulating state to charge disproportionation on the Ni site [10], recent experimental and theoretical work has pointed out that $\mathbf{Q}_{\mathrm{BO}}$ actually results from ordering of the Ni-O bonds [81, 94]. The key to this finding is the negative charge transfer energy Δ_{CT} and the inherent *self-doped* ground state in RNiO$_3$. As discussed in Section 1.2, for $\Delta_{\mathrm{CT}} < 0$ an electron is transferred from the oxygen ligands to the Ni $3d$ orbital, effectively resulting in a $d^8\underline{L}^1$ configuration [78], where $\underline{L}$ stands for a hole on the oxygen ligands. At the MIT, the electrons rearrange on the oxygen ligands, whereas the Ni ions remain in the d^8 state. Consequently, alternating octahedra with longer (LB) and shorter (SB) Ni-O bond-lengths are formed in the insulating phase, which have a $d^8\underline{L}^0$ and $d^8\underline{L}^2$ configuration, respectively [6]. The insulating state with alternating octaherada is illustrated in Fig. 1.4 (a). The bond order manifests itself for example in x-ray absorption spectroscopy (XAS), where two pronounced peaks develop in the insulating state, corresponding to LB and SB octahedra, see Fig. 1.4 (b). The bond order directly influences the magnetic spin present on each NiO$_6$ octahedra. For the LB site in d^8 configuration, the spin of the Ni ion remains largely unaffected by the oxygen, that is $S \approx 1$. In contrast,
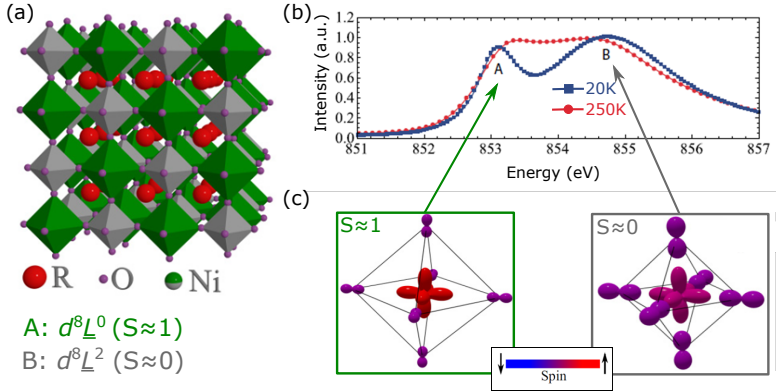
Figure 1.4: Bond order $R\mathrm{NiO_3}$. (a) Crystal structure in the insulating state with alternating LB (site "A", green) and SB ("B", gray). (b) XAS spectra for insulating and metallic phase. In the insulting state $(T = 20\,\mathrm{K})$, we observe a pronounced double peak structure indicating bond disproportionation. The clear signature of a double peak is absent in the metallic phase $(T = 250\,\mathrm{K})$. (c) Magnitude of spins within the LB and SB $\mathrm{NiO_6}$ octahedra, respectively. Panel (a) and (c) are taken from Ref. [6].

the oxygen holes on the SB site of configuration $d^8\underline{L}^2$ largely screen the spin of the Ni ion resulting in a $S \approx 0$ state.

In addition to bond order, $R\mathrm{NiO_3}$ with $R \neq \mathrm{La}$ host an unusual AFM order, which either develops simultaneously with the MIT upon cooling (for $R = \mathrm{Nd}$, Pr) or at lower temperatures in the insulating state (for smaller R; see Fig. 1.3) [95]. Early neutron powder diffraction experiments on $R\mathrm{NiO_3}$ found the magnetic ordering vector $\mathbf{Q}_{\mathrm{AFM}} = (\mathrm{^1/_4}, \mathrm{^1/_4}, \mathrm{^1/_4})_{\mathrm{pc}}$ [96, 97]. Two different spin structures were discussed to explain this peculiar ordering vector: a collinear up-up-down-down state or a noncollinear spin spiral. Independent magnetic x-ray scattering experiments later demonstrated a spin-spiral magnetic ground state (*c.f.* Fig. 1.5) in bulk-like films of $\mathrm{PrNiO_3}$ and $\mathrm{NdNiO_3}$ [86, 98, 99]. Ferromagnetic planes are stacked along the [111] direction with alternating SB and LB sites. Adjacent moments along
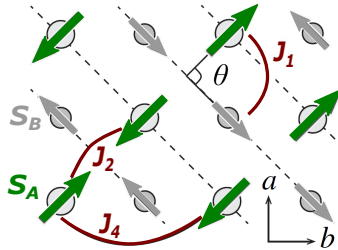
Figure 1.5: Noncollinear spin spiral in bulk RNiO$_3$. Ferromagnetic planes stacked along the [111] direction are indicated with dashed lines. Alternating planes host LB and SB sites with spins S_A (green) and S_B (gray). Neighboring spins have a 90° orientation with respect to each other. We indicated important exchange couplings (J_1, J_2 and J_4), which will be determined in Chapter 3 using RIXS. The Fig. is adapted from Ref. [100].

the [111] direction are rotated by 90° with respect to each other. We have indicated the nearest and next-nearest exchange couplings J_1, J_2 and J_4, respectively, in Fig. 1.5. The hitherto unknown exchange couplings will be determined in Chapter 3 using high-resolution resonant inelastic x-ray scattering and a spin-only model. Based on these observations we develop a microscopic model to explain the unique spin-structure in RNiO$_3$.

1.3.2 Tunable properties in RNiO$_3$ by heterostructuring

The strong connection and interplay of electronic and structural degrees of freedom in RNiO$_3$ offers an exciting playground to selectively tune several collective ordering phenomena by means of heterostructuring in these materials. Recent technical advances in the synthesis of epitaxial thin films and heterostructures allow one to combine different TMOs in artificial multilayer systems [5,26,84,101] and to tailor their properties in an unprecedented fashion [84,87,101–103]. In such systems, novel

and exotic states of matter can emerge, that are not present in the
bulk forms of the constituent materials, due to the complex interplay
of spin, orbital, and structural degrees of freedom [84, 104, 105] and
the proximity of competing states. Prominent examples of emergent
phenomena in TMOs comprise induced electronic and magnetic phase
transitions [106,107], orbital reconstructions [87,108,109], and interface
superconductivity [25, 26, 110]. Furthermore several functionalities can
be tuned by methods closely related to the concept of heterostructring,
such as lattice misfit with a substrate [111,112], chemical doping [113],
or electric [114] and magnetic fields. A profound understanding of the
underlying mechanism of these phenomena is of utmost importance to
enable a full control for future functional devices [21, 22].

   In particular, the prospect of realizing high-T_c cuprate-like physics
in orbitally engineered heterostructures of RNiO$_3$ [115,116] has sparked
enormous interest in thin-films and multilayers [77, 104, 117]. In addi-
tion to superconductivity, Giovannetti *et al.* [118] has predicted that
the combination of period-four AFM order and bond disproprotiona-
tion [119] in RNiO$_3$ could give rise to multiferroicity. In the follow-
ing paragraphs we provide a partial overview of important findings on
heterostrucures comprising RNiO$_3$. We will focus on the findings rel-
evant for the studies described in Chapters 3 and 4 and recommend
Refs. [77,105,120], which are a more extensive review on that topic.

   We first discuss a **spin-density wave (SDW)** that has been real-
ized in heterostructures comprising ultra-thin magnetically active RNiO$_3$
layers. A SDW is characterized by a metallic state where AFM order
persists in absence of bond order. Such a magnetic state, in a material
that simultaneously is a good electrical conductor, is of great interest
as an active element in so-called spintronics. The SDW state does not
occur in bulk-like films as bond order is a prerequisite for the onset
of AFM order (*c.f.* bulk phase diagram in Fig. 1.3). The SDW in
RNiO$_3$ has first been identified by µSR measurements in superlattices
with 2 unit cell (u.c.) thin LaNiO$_3$ stacks below $T \approx 100$ K [121].

The AFM phase is clearly absent in superlattices with thicker LaNiO$_3$ layers, which preserve bulk-like properties. The absence of bond order was later confirmed by resonant hard x-ray scattering at the Ni K edge [122], while the noncollinear AFM state was verified by magnetic x-ray scattering at the Ni L edge [86]. The latter study additionally identified that the d orbital population of the Ni directly affects the polarization plane of the noncollinear spin spiral in RNiO$_3$. The orbital occupation and polarization in RNiO$_3$ can be effectively modulated using epitaxial strain and spatial confinement [87,108,109]. Further investigations using Raman scattering and x-ray absorption spectroscopy have also revealed the presence of a SDW in PrNiO$_3$-based superlattices [123, 124], where one can realize an AFM spiral in the absence of bond order through a rational combination of epitaxial strain and spatial confinement.

Second, we introduce recent experiments, where epitaxial structures were grown with interfaces other than the ordinary $(001)_{pc}$ (pseudocubic notations) plane. In particular, **$[111]_{pc}$-oriented heterostructures and thin-films** have attracted widespread attention [85, 117, 125–127] to realize graphene-like physics[2] with possible nontrivial topological phases in RNiO$_3$. Catalano *et al.* reported that the T_{MIT} of a 100 Å thick NdNiO$_3$ film can be enhanced by more than 100 K when grown onto [111]-oriented NdGaO$_3$ substrates [85] [see Fig. 1.6 (b)]. One key characteristic of the [111]-oriented surfaces is the three-fold interconnectivity across the interface between the NiO$_6$ octahedra of the film and the GaO$_6$ octahedra of the substrate (see Fig. 1.6). In contrast, ordinary (001) interfaces share only one oxygen atom between thin-film and substrate. Therefore, the Ni-O-Ni bond angle can be altered in a straightforward fashion using [111]-oriented substrates. As we have seen in the phase diagram of RNiO$_3$ in Fig. 1.3, the Ni-O-Ni bond angle effectively controls the bandwidth of the system and pa-

---

[2]The $(111)_{pc}$ surface represents a buckled honeycomb structure similar to graphene.

rameterizes the MIT and AFM ordering temperature. In addition to
modified transition temperatures in [111]-oriented heterostructures, the
[111]-orientation offers the unique possibility to truncate the exchange
bonds along the magnetic ordering vector, as the surface normal co-
incides with the direction of the magnetic ordering vector. Therefore
ultra-thin slabs in [111]-oriented heterostructures offer an alternative
material platform to exfoliated 2D materials. Exactly this concept has
been exploited by Hepting *et al.*. The authors identified a crossover
from the noncollinear spin spiral to a collinear AFM state as a function
of $R\mathrm{NiO_3}$ layer thickness using magnetic x-ray scattering at the Ni L
edge (see Fig. 1.6 and Fig. 3.2). The observed collinear spin structure
comes along with suppressed bond order and results from truncating
the exchange bonds at the interface to nonmagnetic metal oxides [126].

Despite enormous research efforts, superconductivity has not been
detected in the $R\mathrm{NiO_3}$ perovskite phase. However, very recently Li
et al. discovered superconductivy in infinite-layer nickelate thin films
with composition $\mathrm{Nd_{0.8}Sr_{0.2}NiO_2}$ [128]. This $R\mathrm{NiO_2}$ compound is syn-
thesized from the perovskite precursor phase using a soft-chemistry
topotactic reduction and shows a superconducting transition tempera-
ture of about 9 to 15 K. Several experimental [128, 129] and theoreti-
cal [130,131] studies suggest a pronounced similarity to high-T_c cuprates
in terms of structure and the $d_{x^2-y^2}$ pairing channel. The observation
of a superconducting dome as a function of Sr doping further qualifies
$R\mathrm{NiO_2}$ as possible analogue to the high-T_c cuprate superconductors.
While the discovery of superconductivy in the Ni compounds surely
can be considered as a breakthrough, many open questions remain yet
to be clarified, including the possible role of the rare-earth ion for the
pairing mechanism and the effect of epitaxial strain on the stabilization
of the unusual $\mathrm{Ni^{1+}}$ valence state [72].

This short review exemplifies the possibilities to alter the phase
behavior of $R\mathrm{NiO_3}$ by means of heterostructing and to realize novel,
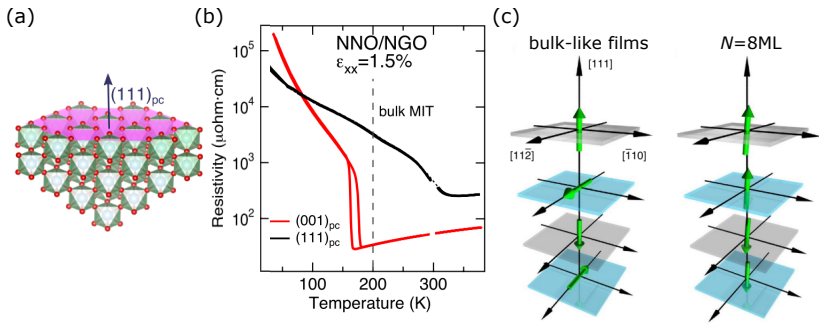exotic phases that are not present in the bulk. Along these lines, recent

Figure 1.6: [111]-oriented heterostrucutres. (a) Increased connectivity to the substrate for [111]-oriented interfaces, as film and substrate share three oxygen atoms. (b) Comparison of temperature-dependent resistitivity for NdNiO_3 (NNO) thin films grown on [111]- and [001]-oriented NdGaO_3 (NGO) substrate, respectively. The NNO film on [001]-oriented NGO shows bulk-like behavior, while the film on [111]-oriented NGO has a higher MIT temperature. (c) Crossover from non-collinear spin order to collinear mangetic order as a function of nickelate layer thickness N. The magnetic structure is inferred from resonant magnetic x-ray scattering. The Fig. is reproduced from Refs. [85] and [126].

theoretical and experimental studies suggest that the mechanism of the MIT differs for bulk and ultrathin nickelate layers [79,132]. Other studies indicate a close feedback between AFM and bond order, such that the presence of the former profoundly modulates the bond disproportionation amplitude [133, 134]. To further investigate the interactions and hierarchy of different ordering phenomena in RNiO$_3$ and to test model calculations, it is therefore crucial to experimentally determine both, bond and magnetic order, as well as to gain further insights to the crystal structure, including the position of oxygen atoms, quantitatively and on the very same samples. We therefore use resonant x-ray scattering techniques, which will be introduced in detail in Chapter 2, to investigate electronic and structural properties in RNiO$_3$.

We emphasize that despite decades of research on RNiO$_3$, the origin of the noncollinear spin spiral remains a puzzle, since a microscopic model for the noncollinear order is missing. In Chapter 3 we illustrate how resonant inelastic x-ray scattering (RIXS) can be used to simultaneously probe magnetic and bond order and the corresponding collective excitations in RNiO$_3$. In combination with theoretical models, we quantify the bond order as well as the magnetic exchange interactions that cause the unusual noncollinear spin spiral order of RNiO$_3$. We apply this methodology to thin films as well as to superlattices to explore the properties of RNiO$_3$, both in a bulk-like setting and in spatially confined layers.

While the role of octahedral tilts and rotations has been extensively studied in bulk RNiO$_3$ (see Fig. 1.3), yet only few studies have addressed its role in heterostructures. In Chapter 4, we conduct a comprehensive study of scanning transmission electron microscopy (STEM) [135–137], transport measurements and x-ray scattering as complementary techniques probing different length scales. We demonstrate that a macroscopic response (*i.e.* the T_{MIT} and the magnetic transitions temperature) can be varied over a wide temperature range utilizing strain engineering. In particular, we will discuss the role of

collective octahedral tilts and rotations, and their interplay with electronic degrees of freedom. Identifying the relevant and competing energy scales, we discuss advantages and limitations to stabilize nonequilibrium phases by heteroepitaxy.

1.4 Single-layer ruthenates $(Ca_{1-x}Sr_x)_2RuO_4$

Different physics comes into play in quantum materials with pronounced spin-orbit coupling (SOC). As discussed in Section 1.1 SOC is sizable in $4d$ TM ions, such as Sr_2RuO_4 and Ca_2RuO_4 [138]. Here, we introduce the Mott insulator Ca_2RuO_4, which hosts a temperature-driven MIT and follows an unconventional mechanism for AFM ordering. In analogy to RNiO$_3$, the properties of Ca_2RuO_4 can be tuned by epitaxial strain [139]. Here we focus on the possibility of *in-situ* control by electrical currents to continuously and dynamically alter the properties of Ca_2RuO_4. In the following Sections, we briefly review the structural and magnetic properties of bulk Ca_2RuO_4 and discuss recent results obtained from external perturbations by applying DC currents.

1.4.1 Structural and magnetic properties of Ca_2RuO_4

Controlling and stabilizing electronic phases in correlated-electron materials are pivotal objectives of modern solid-state science [21, 84]. In this context, compounds with $4d$ valence electrons have attracted a lot of attention as a plethora of ground states can be observed [141]. In particular, the fine balance between electron correlations, SOC and structural distortions in $4d$ metal oxides manifests itself as a high susceptibility to external perturbations. One prominent example is the layered perovskite system $(Ca_{1-x}Sr_x)_2RuO_4$ (see Fig. 1.7) whose end members, Ca_2RuO_4 and Sr_2RuO_4, are a Mott insulator and an unconventional superconductor, respectively [142, 143]. Compounds with mixed Ca and Sr composition can show metallic behavior with short-
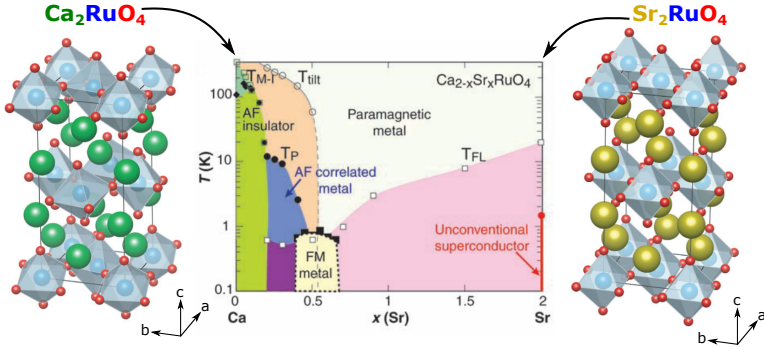
Figure 1.7: Phase diagram of the layered perovskite system $(Ca_{1-x}Sr_x)_2RuO_4$ with structure plots of the end members Ca_2RuO_4 and Sr_2RuO_4. Isovalent substitution of Ca by Sr leads to reduced tilts of the octahedra. Octahedra tilts, distortions, and rotations therefore govern the electronic response of the system. The structural plots are taken from Ref. [51] and the phase diagram is taken from Ref. [140].

range ferromagnetic fluctuations. The different phases follow the structural distortions that arise from the difference in ionic radii of Ca and Sr (Fig. 1.7).

Sr_2RuO_4 is considered as a poster child for unconventional superconductivity, as it is isostructural to the high-T_c cuprate compound $La_{2-x}Ba_xCuO_4$ and shows unprecedented crystal purity as well as minimal disorder. The discovery of superconductivity in Sr_2RuO_4 benchmarked a new area of research, as Sr_2RuO_4 was the first discovered perovskite without copper, that hosts superconductivity —albeit at a rather low transition temperature of $T_c = 1.5\,\mathrm{K}$ [142]. While cuprates have a d^9 configuration with spin $S = 1/2$, the Ru ions have a d^4 configuration and $S = 1$. In particular, the spin triplet symmetry of the superconducting order parameter originally inferred from initial µSR [144] and Knight-shift measurements [145] has sparked enormous attention, as Sr_2RuO_4 was interpreted in analogy to p-wave mediated pairing in superfluid ^{3}He [146]. Among the numerous experimental and

theoretical studies [147–149], we highlight that Fermi-liquid behavior above the superconductive transition was inferred from quantum oscillations [150]. After more than 20 years of research Sr_2RuO_4 was considered the prime — and also the only— candidate for odd-parity superconductivity [149]. For a detailed review of Sr_2RuO_4 and implications for quantum computing as well as topological superconductivity we point the reader to Refs. [151,152]. Recently a game-changing observation revived enormous interest in the symmetry of the order parameter: nuclear magnetic resonance results challenged the interpretation of the p-wave superconductivity in Sr_2RuO_4 [153], as the Knight-shift experiments could possible be adulterated by heating effects [154]. These recent experiments lead to new discussions in theory and experiments, where previous studies were critically reevaluated [155, 156]. To date most experimental studies suggest a d-wave character for Sr_2RuO_4, while a theoretical consensus has not yet been reached. Therefore, the superconductivity in Sr_2RuO_4 remains an active field of research even after decades of investigation.

The isovalent sister of Sr_2RuO_4 — Ca_2RuO_4 — shows a temperature-driven MIT at $T_{MIT} = 357\,K$ [159,161,162] (see Fig. 1.8). The concomitant structural phase transition preserves the lattice symmetry (space group $Pbca$), but yields elongated RuO_6 octahedra with a reduced tilt and an enlarged c lattice parameter in the high-temperature metallic state. The insulating and metallic phases are therefore named *"S"-Pbca* and *"L"-Pbca* phase, respectively, where S and L refer to short and long c axes [see Fig. 1.8 (a) and (b)]. In addition to temperature, other parameters, such as Sr substitution [143], epitaxial strain [139], and hydrostatic pressure [163], can turn Ca_2RuO_4 metallic. Hence, Ca_2RuO_4 offers the possibility to alter the electronic response by structural distortions due to the strong relationship of structural and electronic properties.
The key role of octahedral rotation, compression and tilts is further evident in the magnetic state of Ca_2RuO_4, which sets in at $T_N =$
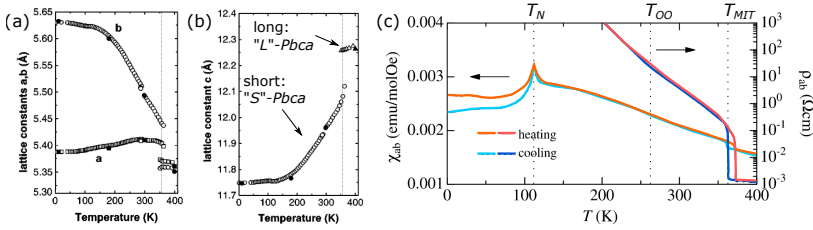
Figure 1.8: Basic properties of Ca_2RuO_4. (a), (b) Lattice constants of Ca_2RuO_4 as a function of temperature. (c) Magnetization and resistivity of Ca_2RuO_4 as a function of temperature for both cooling and heating cycle. We mark important temperatures: onset of magnetic order T_N, orbital order T_{OO} [157] and the MIT at T_{MIT}. Note that the role and presence of orbital order is not fully resolved in Ca_2RuO_4. Other interpretations revolve around a spin-nematic transition [158] at T_{OO}. The close connection of structural and electronic properties is evident. Panels (a) and (b) are taken from Ref. [159], panel (c) is adapted from Ref. [160].

110 K and is characterized by an G-type AFM ordering [159] [see Fig. 1.8 (c)]. Several theoretical [56–58] and experimental [50, 59] studies point towards an unconventional mechanism for magnetic ordering in Ca_2RuO_4, resulting from the condensation of spin-orbit excitons [see Fig. 1.1, panel (b)]. The tetragonal compression Δ splits the $J = 1$ triplet into a doublet (T_x/T_y) and a singlet (T_z). The doublet is separated from the nonmagnetic $J = 0$ state by the energy cost E to create an exciton. E can be overcome by the exchange energy $W \approx 2zJ$ resulting from superexchange interactions (*c.f.* the Heisenberg Hamiltonian in equation 1.2). Since the SOC[3] is of a comparable energy scale as the tetragonal compression and exchange interaction $(\lambda \approx \Delta \approx J \approx 100\,meV)$, the magnetically active doublet condenses into the $J = 0$ groundstate and long-range magnetic order is formed. The "excitonic magnetism" model further predicts that Ca_2RuO_4 lies

---

[3]Recall that SOC is particularly effective in open-shell t_{2g} systems such as Ca_2RuO_4.

close to a quantum critical point (QCP at $E \approx W$) separating long-range ordered AFM and spin-orbit singlet states, which was confirmed by the experimental observation of a soft longitudinal amplitude mode of the spin-orbit condensate [50]. In analogy to high-energy physics the amplitude fluctuations of the complex order parameter is called Higgs mode.

The close link between electronic properties and the structure, *i.e.* ocathedral tilts, rotations, and compression, in Ca_2RuO_4 offers the intriguing possibility to tune the response of the system by external perturbations. Recent research has revealed new ways of *in-situ* control of nonequilibrium phases in Ca_2RuO_4 by electrical currents, which facilitates *in-operando* tuning of quantum materials with potential use for applications.

1.4.2 Current-stabilized phases in Ca_2RuO_4

In this Subsection, we summarize important studies about DC current effects in Ca_2RuO_4. In their pioneering work Nakamura *et al.* [164] found a current-induced MIT at electrical fields much smaller than those required for a conventional Zener breakdown. X-ray diffraction measurements indicated that the current-induced metallic phase, also called L^*, differs from the temperature-driven metallic L-phase [Fig. 1.9 (b)]. Further studies focused on the current-induced closing of the Mott gap [165] and discussed the nonequilibrium phases of Ca_2RuO_4 in close relation to nonequilibrium superconductors and charge-ordered insulators. Interestingly, a stripe pattern separating metallic and insulating regions was recently observed by scanning near-field optical microscopy with the stripe orientation perpendicular to the direction of the applied current [166]. This unusual phase separation was found at intermediate current densities, *i.e.* smaller than the critical value to induce the MIT. These results were explained in terms of long-range strain effects resulting from the strong coupling between electronic and structural degrees of freedom in Ca_2RuO_4. Importantly, so far all ex-

periments, including spatially resolved investigations, suggest that the current-induced metallic state is a nonfilamentary bulk phenomenon.

Besides the MIT observed at currents of about $100\,\mathrm{mA}$, Sow *at al.* reported a large diamagnetic response [167] at much smaller current densities and below $T = 50\,\mathrm{K}$ [see Fig. 1.9 (a)]. The authors suggest a phenomenological model in which the gap closing induced by electrical currents gives rise to a semimetallic state with small electron and hole pockets. A detailed study based on neutron crystallography in combination with *ab-initio* calculations indeed found a partially gapped Fermi surface, thereby indicating a semimetallic electronic structure in the current-induced state [168]. Figure 1.9 (b) summarizes the c lattice parameter for AFM, insulating (S-phase), semimetallic, diamagnetic (S^*-phase) and metallic (L^*-phase) behavior. We note here, that S^* and L^*-phase coexist for certain current values. Very recently, Mattoni *et al.* [169] challenged the observation of the diamagnetic signal and identified it as a spurious contribution due to heating effects, and Ref. [167] has since been withdrawn. Nevertheless, the current-driven transition into the semimetallic state and the MIT remains unaffected by these new insights.

The driving mechanism behind the closing of the Mott gap by DC currents, which is considered the essential ingredient for the semimetallic behavior, is yet to be clarified together with the possible role played by Joule heating. This has motivated the spectroscopic study we report in Chapter 5. The current-stabilized steady state opens the rare possibility to perform inelastic photon scattering experiments in a nonequilibrium state that would be extremely challenging in light-induced transient phases [170]. As we will see in the next Chapter, Raman light scattering simultaneously probes the magnetic, electronic, and structural properties of TMOs and therefore is the ideal tool to study the current-stabilized nonequilibrium phases of $\mathrm{Ca_2RuO_4}$. Additionally, we exploit the unique capability of Stokes and anti-Stokes Raman scattering to probe the temperature of the sample *in-situ*. We rule out
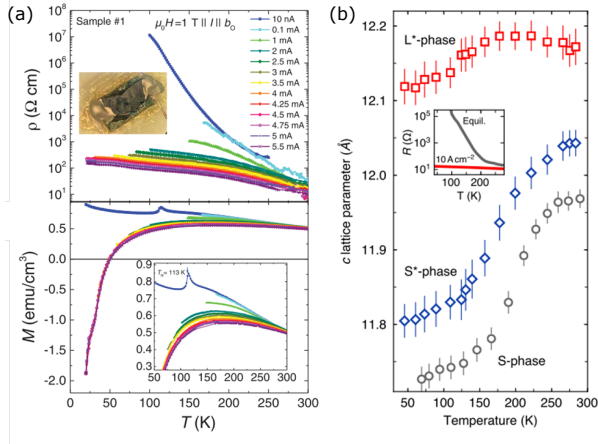
Figure 1.9: Current effects in Ca_2RuO_4. (a) Resistivity and magnetization as a function of temperature T for varying current values. For small current densities and low temperatures, Ca_2RuO_4 shows semimetallic and diamagnetic behavior, in contrast to the AFM and insulating behavior, which is observed in the equilibrium phase. (b) The c-axis lattice parameter is given as a function of temperature T for S-, S^*-, and L^*-phase. The inset shows the resistance as a function of T with (red) and without (gray) applied current. Panel (a) is taken from Ref. [167] and panel (b) from Ref. [168].

Joule heating as the origin of the current-driven MIT in actively cooled environments and demonstrate that the current-stabilized phases are distinct from the equilibrium ones.

Chapter 2

Light scattering from solids

In the scope of this thesis work we harness to a large extent light scattering experiments to investigate TMOs. We exploit a selection of light sources, offering variable energy ranges, and different detection schemes, including energy-resolved, energy-integrated, and momentum-dependent photon detection. In particular, we focus on the two complementary techniques, resonant x-ray scattering (RXS), including inelastic (RIXS) and elastic (REXS) scattering, and Raman light scattering. The general idea of every scattering experiment is quite straightforward: shine light with a defined wavelength/energy at a given scattering geometry on the sample/system/material of interest and measure the properties of the emitted photons. Thereby one can gain access to important features of the system of interest in its ground or excited states. More specifically, we compare the frequency, momentum, and polarization of the incoming photon (ω, $\mathbf{k}$, and $\boldsymbol{\varepsilon}$) with the one from the scattered photon (ω', $\mathbf{k}'$, and $\boldsymbol{\varepsilon}'$) to map out the properties of possible excitations in the system via conservation laws. The possibility to study elementary excitation of different nature makes scattering ex-

periments an important tool to investigate TMOs, as these techniques offer the appealing prospect to probe charge, spin, lattice, and orbital degrees of freedom within one experiment.

In this Chapter, we review important theoretical and experimental aspects of light scattering in solids. We specifically focus on the techniques used in subsequent Chapters, *i.e.* Raman and resonant x-ray scattering. Further, we exemplify how light scattering can be used to exploit synergetic effects with theoretical models to quantify important microscopic parameters. We point out that resonance effects and inelastic scattering can only be described using second-order perturbation theory as they include transitions via a virtual state. We now turn to the theoretical background and develop a general scheme in describing photon scattering experiments on a quantum mechanical and classical basis.

2.1 Theoretical background of light scattering in solids

2.1.1 Quantum mechanical treatment

We start the discussion of light-matter interaction with a general Hamiltonian

$$\mathcal{H}_{\text{full}} = \mathcal{H} + \mathcal{H}_{\text{p}} + \mathcal{H}' \tag{2.1}$$

which includes the many-body Hamiltonian of the material $\mathcal{H}$, the Hamiltonian of the photons $\mathcal{H}_{\text{p}}$, and the electron-photon interaction term $\mathcal{H}'$. The general idea to evaluate $\mathcal{H}_{\text{full}}$ is based on perturbation theory, where $\mathcal{H}_{\text{full}}$ is split into the unperturbed part $\mathcal{H}_0 = \mathcal{H} + \mathcal{H}_{\text{p}}$ and the perturbation $\mathcal{H}'$. We start with a general introduction and treatment of $\mathcal{H}_{\text{full}}$. Later we discuss specific details for Raman and RXS experiments, which are reflected in slight variations of $\mathcal{H}_{\text{full}}$.

$\mathcal{H}$ can be approximated for example by the Hubbard Hamiltonian

presented in equation 1.1, or by other auxiliary systems [54,171]. The photonic Hamiltonian $\mathcal{H}_\mathrm{p}$ is expressed in second quantization

$$\mathcal{H}_\mathrm{p} = \frac{1}{2} \sum_{\mathbf{k},\boldsymbol{\varepsilon}} \hbar\omega(\mathbf{k},\boldsymbol{\varepsilon})(a^\dagger_{\mathbf{k},\boldsymbol{\varepsilon}} a_{\mathbf{k},\boldsymbol{\varepsilon}} + a_{\mathbf{k},\boldsymbol{\varepsilon}} a^\dagger_{\mathbf{k},\boldsymbol{\varepsilon}}) \tag{2.2}$$

where $a_{\mathbf{k},\boldsymbol{\varepsilon}}$ ($a^\dagger_{\mathbf{k},\boldsymbol{\varepsilon}}$) annihilates (creates) a photon with momentum $\mathbf{k}$ and polarization vector $\boldsymbol{\varepsilon}$. The light-matter interaction ($\mathcal{H}'$) describes the interaction of an external photon field with the material. The vector potential $\mathbf{A}$ of the incoming photon couples to an electron of the material by modifying its momentum according to $\mathbf{p} \to \mathbf{p} + e\mathbf{A}$, where $-e$ is the electron charge. Here we neglect an additional magnetic term of the form $\frac{e\hbar}{2m}\boldsymbol{\sigma} \cdot (\nabla \times \mathbf{A})$, with the electron mass m and the Pauli matrices $\boldsymbol{\sigma}$, as the contribution is much smaller than the nonmagnetic one. The interaction Hamiltonian $\mathcal{H}'$ can be obtained from the difference of modified and initial kinetic energy of the electron

$$\mathcal{H}' = \sum_i \left[\frac{(\mathbf{p}_i + e\mathbf{A}(\mathbf{r}_i))^2}{2m} - \frac{\mathbf{p}_i^2}{2m} \right] = \sum_i \left[\frac{e}{m}\mathbf{p}_i \cdot \mathbf{A}(\mathbf{r}_i) + \frac{e^2}{2m}\mathbf{A}^2(\mathbf{r}_i) \right] \tag{2.3}$$

where we sum over all electrons i on sites $\mathbf{r}_i$ [172,173]. $\mathcal{H}'$ is composed of terms with the respective form $\mathbf{p} \cdot \mathbf{A}$ and $\mathbf{A}^2$, which we will discuss separately. To this end, we expand the vector potential $\mathbf{A}$ in plane waves using the photon creation and annihilation operators

$$\mathbf{A}(\mathbf{r}_i) = \sum_{\mathbf{k},\boldsymbol{\varepsilon}} \sqrt{\frac{\hbar}{2V\epsilon\omega(\mathbf{k},\boldsymbol{\varepsilon})}} \boldsymbol{\varepsilon}_\mathbf{k}(a_{\mathbf{k},\boldsymbol{\varepsilon}} e^{i\mathbf{k}\mathbf{r}_i} + a^\dagger_{\mathbf{k},\boldsymbol{\varepsilon}} e^{-i\mathbf{k}\mathbf{r}_i}) \tag{2.4}$$

where V is the volume and ϵ the permittivity of the system, respectively. We realize that the $\mathbf{p} \cdot \mathbf{A}$ term (first term of $\mathcal{H}'$ in equation 2.3) is linear in photon creation/annihilation operators and therefore describes absorption and emission processes. The second term in equation 2.3, $\mathbf{A}^2$, is quadratic in photon creation/annihilation operators and consequently involves transitions where the number of photons changes

by zero or two.

To facilitate the comparison with experiments we introduce the transition rate w. The time-dependent perturbation $\mathcal{H}'$ enters the transition rate w for a specific excitation via Fermi's golden rule, which readily follows from the Schröderinger equation with a time-dependent perturbation

$$w = \frac{2\pi}{\hbar} \sum_f \left| \langle f|\mathcal{H}'|i\rangle + \sum_n \frac{\langle f|\mathcal{H}'|n\rangle \langle n|\mathcal{H}'|i\rangle}{E_i - E_n} \right|^2 \delta(E_f - E_i) \qquad (2.5)$$

where $\langle i|$, $\langle f|$, and $\langle n|$ are the initial, final, and intermediate state of the combined photon-matter state with energies E_i, E_f, and E_n, respectively. In general, the first term of equation 2.5 dominates the transition rate. Close to a resonance, $E_i \approx E_n$, the second term becomes large and governs the transition rate w. The resonant enhancement is the essence of all resonant scattering techniques such as REXS and RIXS. We exploit the resonance effect in particular to boost the sensitivity to specific elements and transitions. Importantly, the first term in equation 2.5 (first-order perturbation theory) cannot describe inelastic scattering events, as the scattering process involves a two-step process via an intermediate [vibronic (electronic) state in the case of phononic Raman (RIXS) scattering] state. Therefore only second-order perturbation theory can be used to describe inealstic scattering, such as Raman scattering and RIXS. We emphasize, that the second term in equation 2.5 solely depends on the energy of the intermediate, virtual state, not on the energy of the final state. The delta function on the other hand is independent of E_n, therefore energy conservation is not required for the virtual intermediate transition.

We first discuss x-ray absorption spectroscopy (XAS), which is described by the first-order matrix element in equation 2.5 and illustrated in Fig. 2.1 (b). Since absorption constitutes a one photon process, we focus on the $\mathbf{p} \cdot \mathbf{A}$ term. We evaluate the first-order matrix element

$\langle f|H'|i\rangle$ in equation 2.5 by using the dipole approximation. Note that we change conventions and describe purely electronic states by $\langle i|$ and $\langle f|$ with energies E_i and E_f, respectively. The properties of the photons are explicitly expressed using ω, $\mathbf{k}$, and $\boldsymbol{\varepsilon}$ (for incoming) and ω', $\mathbf{k}'$, and $\boldsymbol{\varepsilon}'$ (for outgoing). The XAS intensity is given by [45, 171]

$$I_{XAS}(\hbar\omega, \boldsymbol{\varepsilon}) \propto \sum_f \langle f|\boldsymbol{\varepsilon}\cdot\mathbf{r}|i\rangle^2 \, \delta(E_f - E_i - \hbar\omega) \qquad (2.6)$$

Using a Green's function approach and introducing the finite core hole lifetime Γ, the XAS intensity can be expressed as

$$I_{XAS}(\hbar\omega, \boldsymbol{\varepsilon}) \propto \Im\langle f|T^\dagger \frac{1}{\hbar\omega + E_i - \mathcal{H}_0 + \mathrm{i}\Gamma/2}T|i\rangle \qquad (2.7)$$

where T describes the transition operator and $\mathcal{H}_0$ the Hamiltonian of the unperturbed system.

For two-step scattering processes such as RXS and inelastic light scattering, we need to consider equation 2.5 up to second order. In first order only the A^2 term gives finite contribution to the scattering cross section. For visible light these processes can be neglected as the momentum transfer $\mathbf{q}$ is very small, resulting in small matrix elements for excitations where the crystal electronic state significantly changes (*e.g.* for lattice vibrations). However it becomes important for the scattering of x-rays (with inherently higher photon energy and momentum compared to visible light), where larger transferred momentum $\mathbf{q}$ provides nonzero matrix elements between different electronic states. This term is responsible for the nonresonant Thomson scattering, which only depends on the total electron density, and for excitations of free electrons, including electrons in gaseous plasma. Both cases will not be discussed here, as they are irrelevant for the methods and results discussed in this thesis. In second order, the $\mathbf{p}\cdot\mathbf{A}$ term contributes to the scattering cross section for different excitations (magnons in crystals, lattice vibrations, or even polaritions) with two successive photon tran-

sitions. In particular, this term describes resonant scattering and allows scattering between different electronic initial and final states [172,174]. We therefore evaluate the terms linear in $\mathbf{A}$ in second order using the dipole approximation and arrive at the famous Kramers-Heisenberg formula [171,175]

$$
I_{RXS}(\hbar\omega, \boldsymbol{\varepsilon}) \propto \lim_{\Gamma \to 0^+} \sum_f \left| \langle f | T^\dagger \frac{1}{\hbar\omega + E_i - \mathcal{H}_0 + i\Gamma/2} T | i \rangle \right|^2 \\
\delta(\hbar\omega - \hbar\omega' + E_i - E_f) \tag{2.8}
$$

The Kramers Heisenberg formula sets the basis for Raman light scattering and all resonant techniques in particular RIXS.

2.1.2 Linear response theory and dielectric function

While many phenomena of light scattering, such as resonance effects, can only be understood using quantum mechanical treatment, it is instructive to consider the light-matter interaction in a classical scheme. Linear response theory is the fundamental principle of solid state spectroscopy and describes the linear reaction of a system to an external perturbation. It is valid for the whole range of the electromagnetic spectrum from radio waves to γ-rays. The linear response theory can be formulated in time and space, and relates the polarization field $\mathbf{P}$ and electric displacement field $\mathbf{D}$ to the electric field $\mathbf{E}$ of the incoming electromagnetic wave

$$
\mathbf{P}(\mathbf{q}, \omega) = \chi(\mathbf{q}, \omega)\epsilon_0 \mathbf{E}(\mathbf{q}, \omega) \\
\mathbf{D}(\mathbf{q}, \omega) = \epsilon(\mathbf{q}, \omega)\mathbf{E}(\mathbf{q}, \omega) = \epsilon_0 \mathbf{E}(\mathbf{q}, \omega) + \mathbf{P}(\mathbf{q}, \omega) \tag{2.9}
$$

Here the response functions $\chi(\mathbf{q}, \omega)$ and $\epsilon(\mathbf{q}, \omega)$ are the electric susceptibility and permittivity (also known as dielectric function), respectively. In general, $\chi(\mathbf{q}, \omega)$ and $\epsilon(\mathbf{q}, \omega)$ are imaginary second-rank tensors [172] that depend on the frequency ω and the momentum transfer $\mathbf{q}$. The

response functions provide microscopic information about the material and specifically comprise possible collective excitations that range from relaxation processes via excitons to core level transitions. Our focus lies on lattice vibrations (phonons), spin excitations (magnons) and inter-orbital transitions. We express the external electromagnetic field as plane wave $\mathbf{E}(\mathbf{r}, t) = E_0 \boldsymbol{\varepsilon} e^{i(\mathbf{k} \cdot \mathbf{r} - \omega t)}$ with the amplitude E_0, the unit vector along the polarization of the wave $\boldsymbol{\varepsilon}$, the frequency ω, and the wave vector $\mathbf{k}$[1]. We further employ the adiabatic, also called Born-Oppenheimer, approximation, assuming that electrons rapidly follow the slow motion of the heavy atomic nuclei. Therefore we can express χ as a function of the atomic displacement $\mathbf{u}$, *i.e.* as collective waves. We use a Taylor expansion of χ around the equilibrium position for displacements that are small compared to the dimension of the crystallographic unit cell

$$\chi(\mathbf{u}) = \chi_0 + \left.\frac{\partial \chi}{\partial \mathbf{u}}\right|_0 \mathbf{u} + \frac{1}{2}\left.\frac{\partial^2 \chi}{\partial \mathbf{u}^2}\right|_0 \mathbf{u}^2 + ... \qquad (2.10)$$

Following equation 2.9 the polarization yields

$$\mathbf{P} = \left(\chi_0 + \left.\frac{\partial \chi}{\partial \mathbf{u}}\right|_0 \mathbf{u}\right)\mathbf{E} = \chi_0 \mathbf{E} + \left.\frac{\partial \chi}{\partial \mathbf{u}}\right|_0 \mathbf{u} \cdot \mathbf{E} \qquad (2.11)$$

where we have neglected higher-order processes with two ore more collective excitations. The first expression in equation 2.11 ($\chi_0\mathbf{E}$) describes oscillations of the macroscopic polarization that are in phase with the incident radiation, as in the case of elastic x-ray scattering. The term linear in $\mathbf{u}$, *i.e.* the second part of equation 2.11, expresses the electric susceptibility by lattice displacements and therefore accounts for first-order Raman processes [172, 173].

Having established a general scheme of how to describe light-matter interaction on both classical and quantum-mechanical footing, we will

---

[1] Note here that we assume $|\mathbf{E}|$ is constant within a single unit cell of the material. This assumption strictly holds only for visible light as in this case $|\mathbf{k}|$ is smaller than the reciprocal lattice vector of the unit cell.

now advance into specific details of RXS and Raman scattering, the two main techniques utilized in this thesis, followed by a detailed introduction to the experimental setups.

2.1.3 Resonant scattering at the L edge of TMOs

While both experimental techniques, RXS and Raman scattering, are photon-in photon-out techniques, the former explicitly exploits one important aspect: resonance effects. The photon energy is tuned exactly to the energy difference between low-lying core level and an unoccupied valence state. We will focus on $3d$ TMO L-edges, that is the transition from $2p \rightarrow 3d$ states. For Ni these energies lie around $850\,\mathrm{eV}$ (soft x-ray regime).

Figure 2.1 gives an overview of several resonant core-level absorption and scattering experiments. The initial state comprises a completely filled $2p$ shell, while the $3d$ shell is partially filled, a basic characteristic of all TMOs as we have seen in the previous Chapter. The incoming photon with an energy tuned to the $2p \rightarrow 3d$ transition resonantly knocks out a core electron, while a core hole is left behind. This configuration is the final state of the first-order XAS process shown in Fig. 2.1 (b). The system is left in a high-energy state after the absorption of a photon, where the core hole is unstable and interacts with other core and valence states. The finite lifetime of the core hole implies a finite line width connected to the XAS process. In a second step, the energy of the system is released as another electron fills the core hole, while emitting photons or electrons (mostly secondary electrons and some high-energy Auger electrons). These decay channels can be determined experimentally as fluorescence or electron yields and are often a good approximation for the x-ray absorption coefficient of the material. In a scattering experiment, the second-order emitted photon is analyzed in a momentum- (and sometimes even energy- and polarization-) resolved fashion. Depending on the detection scheme, we differentiate between resonant elastic x-ray scattering (REXS) and
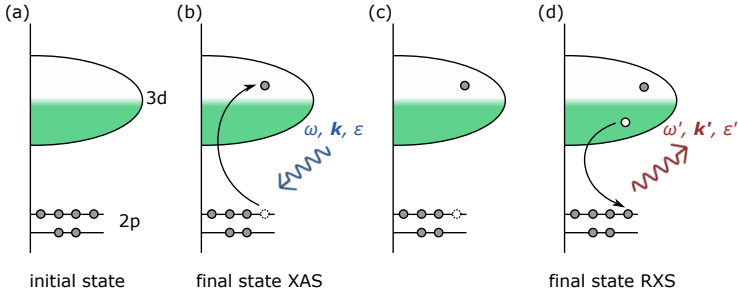
Figure 2.1: Schematic representation of core level spectroscopy at the L-edge. (a) The initial state comprises a fully occupied $2p$ shell and a partially filled $3d$ valence shell, an inherent feature of all TMOs. (b) An incoming photon with frequency ω, momentum $\mathbf{k}$, and polarization $\boldsymbol{\varepsilon}$ resonantly knocks out a valence electron, while a core hole is left behind. This is the final state for XAS. (c) The core hole is unstable and interacts with other core and valence states. The system is left in a highly energetic state after the absorption of a photon. (d) Eventually the energy is released as another electron fills the core hole, while a photon (frequency ω', momentum $\mathbf{k}'$, and polarization $\boldsymbol{\varepsilon}'$) or Auger electron gets emitted. The analysis of the emitted photon in terms of energy, momentum or polarization lies at the heart of resonant x-ray scattering (RXS). The Fig. is inspired from [171].

resonant inelastic x-ray scattering (RIXS). In the former case the pho-
tons are detected in an energy-integrated way using a diode in most
cases. The signal is dominated by the elastic contribution, particu-
lar in the proximity of a structural or magnetic Bragg reflection. In
contrast, RIXS is based on the energy-resolved detection of photons
using energy-dispersive elements incorporated in a spectrometer. In
the case of inelastic photon scattering, the energy and momentum of
the low-energy excitations can be analyzed by investigating the emitted
photons [36, 45, 53, 54]. We will use these low-energy collective excita-
tions to study a variety of different ordering phenomena in TMOs.

2.1.4   Resonant inelastic x-ray scattering

In the previous Subsection, we discussed RXS techniques in a general
scheme. Now we focus on RIXS, which constitutes one major exper-
imental method employed in this thesis. In particular, we use high
resolution RIXS to simultaneously study bond order and spin excita-
tions in $R\mathrm{NiO_3}$. For our RIXS measurements, we use incoming photons
resonantly tuned to the L edge (transition from $2p \rightarrow 3d$) of a TMO.
After interaction with the sample the scattered photons are analyzed in
an energy- and momentum-resolved way. Thereby one can access low-
energy excitations, that are left in the material after the RIXS process.
We will now have a closer look at which elementary excitations are
accessible at the L edges of TMOs and how these excitations can be
used to study fundamental properties of many TMOs, in particular
$R\mathrm{NiO_3}$ [175].

Calculating the RIXS intensity directly from the Kramers Heisen-
berg formula in equation 2.8 is simply impossible, as the full many-body
Hamiltonian in TMOs cannot be solved exactly. Therefore, different
approximation schemes are used to develop expressions for initial, final,
and intermediate states as well as the transition operator. Within these
approximations the scattering intensity can be evaluated, and most im-
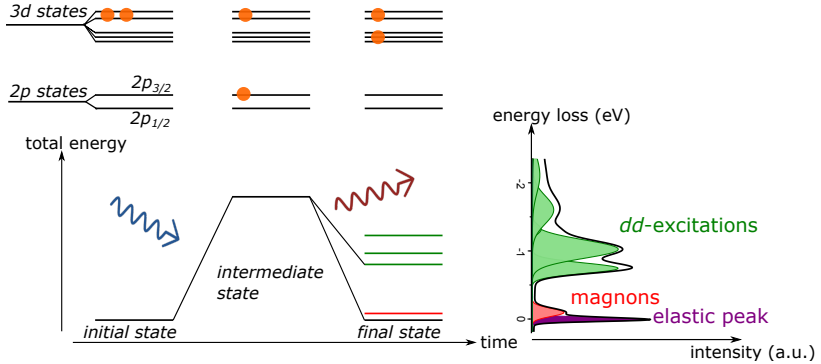portantly we can use these models to extract microscopic quantities

Figure 2.2: Schematic representation of the RIXS process at the L edge of a Ni d^8 system (such as RNiO$_3$) as a function of time. In the upper part we trace the transition of a core hole (shown as orange dot) as a photon gets absorbed and emitted. The lower part connects the energy level of the system and transitions therein with the spectrum measured (right hand side, shown for RNiO$_3$).

from comparison to experimental data. We introduce some of these approximations in the last part of this Chapter in Subsection 2.3.2.

Monitoring the RIXS process as a function of time (Fig. 2.2) yields two transitions of the core hole upon photon absorption and emission, respectively. The possible final state configurations are apparent in the measured spectrum on the lower right hand side. First, we discuss the possibility that the final configuration of the d electrons is not the same as the initial one, *i.e.* effectively resulting in dipole-forbidden inter-orbital excitation. As a hole in the Ni d^8 systems makes two dipole-allowed transitions, the resulting inter-orbital excitation is allowed within the two-step RIXS process (as anticipated in the Kramers-Heisenberg formula). These so-called dd or ligand-field excitations give valuable insight in the orbital and valence-state character of many TMOs. We will use dd excitations in Chapter 3 to study the bond order of RNiO$_3$.

Second, we consider magnetic excitations such as single- or multi-

magnons [176, 177]. Collective magnon excitations can be stimulated due to the strong spin-orbit coupling of the core hole in the intermediate state. Traditionally, magnetic spin excitations are measured by inelastic neutron scattering (INS), due to the substantial magnetic moment of the neutron and inherent sensitivity to interactions with magnetic materials. However RIXS has challenged this well-established technique recently [178], as INS requires massive samples and has blind spots especially at high energies and high doping levels in high-T_c cuprates. RIXS is therefore a powerful — and sometimes even the only — tool to measure momentum-dependent spin excitations from thin films, heterostructures with buried interfaces, and nano-structures. We point out, that single crystalline $R\mathrm{NiO_3}$ are available to date only as thin layers in films and heterostructures[2]. Since the scattering volume is too small for neutrons, momentum-resolved experiments to access AFM and bond order can only be carried out using x-rays.

RIXS has been proven to be an excellent tool to study the electronic properties of correlated oxides. Specifically, the recent improvement in energy resolution of soft x-ray RIXS has made it possible to study in detail both collective magnetic [176–178] and orbital [75, 182–184] excitations in oxides. The use of x-rays with wavelengths of $\lambda \approx 1$ Å allows to probe a sizable fraction of the Brilouin zone, thereby offering the necessary $\mathbf{q}$ resolution to map out dispersive excitations. Additionally, RIXS is sensitive to excitations related to the electronic continuum, which are crucial for high-valence TMOs, such as $R\mathrm{NiO_3}$, where local and itinerant excitations coexist [75, 175, 185]. Furthermore RIXS offers the typical advantages of resonant x-ray techniques, like bulk-sensitivity, element selectivity, and momentum-resolution, together with more detailed spectroscopic information than provided by XAS [186]. In $R\mathrm{NiO_3}$ several ordered phases coexist, making RIXS a powerful tool to probe

---

[2]We are aware of the reports of $\mathrm{LaNiO_3}$ and $\mathrm{PrNiO_3}$ single crystals in Refs. [11,179] and [180], respectively. However, due to the elusive role of oxygen vacancies in these single crystals, we do not consider the single crystals as well established bulk representatives of $R\mathrm{NiO_3}$ [181].

these states simultaneously and in a site-selective manner [100], as well as to gain access to several order parameters within the same experiment.

Despite the great advantages, RIXS has only evolved to its full potential in the past years due to impressive technical advances, which drastically increased the energy resolution. We will briefly touch this development in Section 2.2. Even though theoretically possible, the limited resolving power even in modern RIXS spectrometers makes the measurements of phonons[3] and electron-phonon coupling still extremely challenging with RIXS [189]. To study phonons, we therefore introduce a complementary inealstic photon scattering technique using visible light, namely Raman scattering.

2.1.5 Raman light scattering

Similar to the case of RIXS, Raman scattering is a photon-in photon-out technique, which is described by the Kramers-Heisenberg formula. Instead of x-rays, Raman scattering relies on visible light and the intermediate sate comprises virtual vibronic states for phononic Raman scattering. If the incident monochromatic light has the same energy as the scattered photons, the scattering process is called elastic (or Rayleigh scattering, see Fig. 2.3). In the other case, momentum and energy can be transferred between the photons and the material, and an inealstic scattering event takes place. The creation (anihiliation) of an elementary excitation is called Stokes (anti-Stokes) process. It is important to realize that inelastic events (Raman scattering) are 10^4 times less likely than the elastic scattering process, *i.e.* the elastic line needs to be suppressed using optical filters to obtain a spectrum that is conceptually comparable to the one shown in Fig. 2.3. The Raman experiment detects the energy shift between incident and scattered light,

---

[3]Several experimental studies [187,188] observe changes in the quasi-elastic peak, which can be attributed to an amended phonon dispersion. Our statement refers to the detection of single phonons, similar to Raman or high-energy inelastic x-ray scattering, which is not yet feasible using RIXS, at least in the soft x-ray range.
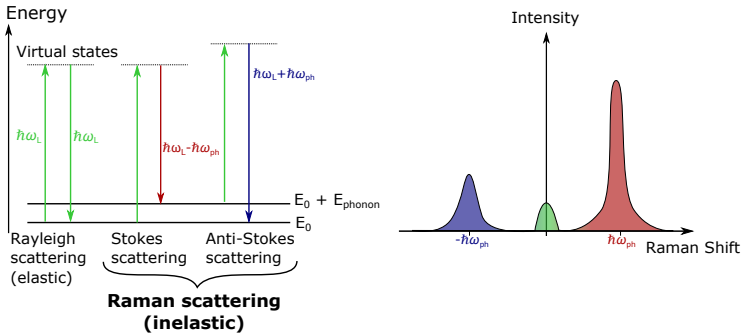
Figure 2.3: Schematic representation of Raman scattering. The transitions indicated on the left side are elastic scattering processes, also called Rayleigh, Stokes and anti-Stokes scattering. The latter two schemes are relevant in Raman experiments. The spectral fingerprints and their energy-dependence are displayed on the right side. We used matching colors for the corresponding transitions in both panels.

which is usually given in units of wavenumber $[\text{cm}^{-1}]$.

The use of visible light with $E \approx 1\,\text{eV}$ and $k \approx 10^{-3}\,\text{Å}$ in Raman experiments imposes some limitations, as the momentum transfer is negligible. Therefore, Raman experiments are mostly limited to the zone center Γ-point of the first Brillouin zone, while RIXS in contrast can probe a large part of the Brillouin zone due to the higher momentum offered by the x-ray photons. Note that second- or higher-order Raman processes can probe larger parts of the Brillouin zone.

Let us start the description of the Raman process in the classical approach based on the linear response theory introduced in Section 2.1.2. We recall the following relationship between polarization $\mathbf{P}$, electric field $\mathbf{E}$, susceptibility χ, and atomic lattice displacement $\mathbf{u}$ that describes the Raman process in first order

$$\mathbf{P} = \left.\frac{\partial \chi}{\partial \mathbf{u}}\right|_0 \mathbf{u} \cdot \mathbf{E} \tag{2.12}$$

Explicitly expressing the electric field as a plane wave yields

$$
\begin{aligned}
\mathbf{P} = \frac{1}{2}\frac{\partial \chi}{\partial \mathbf{u}}\mathbf{u_0}\boldsymbol{\varepsilon}E_0\{&\cos[((\mathbf{k}+\mathbf{q})\cdot\mathbf{r})-(\omega_{\mathrm{in}}+\omega)t]+\\
&\cos[((\mathbf{k}-\mathbf{q})\cdot\mathbf{r})-(\omega_{\mathrm{in}}-\omega)t]\}
\end{aligned}
\tag{2.13}
$$

where we have combined equations 2.10 (only the second term, which accounts for inelastic Raman light scattering) and 2.11. Here we realize that the electric field of the scattered light contains frequencies $(\omega_{\mathrm{in}}\pm\omega)$ that are shifted with respect to the frequency of the incident light ω_{in}. In particular, $(\omega_{\mathrm{in}}-\omega)$ describes the Stokes part, whereas $(\omega_{\mathrm{in}}+\omega)$ gives the anti-Stokes part of the excitations as introduced in Fig. 2.3. We define the so-called Raman tensor $R = \frac{\partial\chi}{\partial\mathbf{u}}\Big|_0\mathbf{u}$. The Raman tensor is a second-rank tensor and a fundamental quantity in the description of phonons, as R reflects the symmetry of the collective lattice vibration. The lattice vibrations are classified according to irreducible representations of the crystallographic point groups. Therefore they are denoted with the same Mullikan symbol as the irreducible representations, and we can use group theory to determine which of the vibrational species have nonvanishing components of R [172].

Following classic electromagnetic theory, an oscillating dipole with frequency ω emits the energy $\partial\Phi_s$ per time in an element of solid angle $\partial\Omega$. The differential cross section $\frac{\partial\sigma}{\partial\Omega}$ is therefore given as [173]

$$
\frac{\partial\sigma}{\partial\Omega} = \frac{1}{I_i}\frac{\partial\Phi_s}{\partial\Omega} = \frac{1}{I_i}\frac{\omega^4}{16\pi^2 c^3}|\boldsymbol{\varepsilon}_s\cdot\mathbf{P}|^2
\tag{2.14}
$$

where $I_i = \epsilon c E_i^2$ is the intensity of the incoming light and c the speed of light. Using equation 2.13 and the definition of the Raman tensor, we arrive at

$$
\frac{\partial\sigma}{\partial\Omega} = \frac{\omega^4}{16\pi^2 c^4}|\boldsymbol{\varepsilon}_s\cdot R\cdot\boldsymbol{\varepsilon}_l|^2
\tag{2.15}
$$

where $\boldsymbol{\varepsilon}_s$ ($\boldsymbol{\varepsilon}_l$) is the light polarization of the scattered (laser, *i.e.* incoming) light. Therefore the intensity observed in a Raman experiment

is given by

$$I_{\mathrm{Raman}} \propto \frac{\partial\sigma^2}{\partial\Omega\partial\omega} = \frac{\omega^4}{16\pi^2 c^4}|\boldsymbol{\varepsilon}_s \cdot R \cdot \boldsymbol{\varepsilon}_l|^2\delta(\omega - \Delta\omega) \qquad (2.16)$$

where we have introduced the double differential scattering cross section $\frac{\partial\sigma^2}{\partial\Omega\partial\omega}$, *i.e.* the power of light scattered into the solid angle $\partial\Omega$ in a frequency range between ω and $\omega + \partial\omega$. The delta function ensures energy conservation and centers the excitation around the Raman shift ω. Equation 2.16 can be condensed into the following expression for the Raman intensity: $I_{\mathrm{Raman}} \propto |\boldsymbol{\varepsilon}_s \cdot R \cdot \boldsymbol{\varepsilon}_l|^2$. We realize that certain combinations of incident and scattered light polarization probe different elements of the Raman tensor R. Additionally, I_{Raman} can vanish even if the components of the Raman tensor are nonzero. These so-called selection rules can be readily derived from the crystal symmetry via group theory. For the characterization of scattering geometry it is therefore necessary to know the direction of incoming and scattered light, as well as their polarizations. This is conveniently summarized using Porto's notation of the from $a(bc)d$. Here a (d) gives the direction of incoming (scattered) light, and b and c the corresponding polarization.

The appealing use of group theory to characterize the symmetry of latice vibrations is the strength and beauty in the classical description of Raman scattering. However, certain aspects, such as the intensity ratio of Stokes and anti-Stokes scattering, can only be derived within a quantum mechanical treatment, which we briefly discuss in the following paragraph.

A full description of Raman scattering on the basis of quantum mechanics goes well-beyond the scope of this short introduction, we refer the curious reader to standard text-books on this topic [173, 174, 190]. Here we present essentials and some important results from the quantum mechanical treatment of phononic Raman scattering. Recalling the discussion about the Kramers Heisenberg formula (equation 2.8)

in the Green's function approach, we notice that the material Hamil-
tonian $\mathcal{H}$ needs to include electron-phonon and phonon-phonon inter-
actions in the case of Raman scattering. To evaluate the matrix ele-
ment of the form $\langle f|\mathcal{H}|i\rangle$ in equation 2.8, one assumes the same initial
and final electronic electronic state, while the vibronic part of the sys-
tem changes. The vibrational wave function are expressed as harmonic
oscillator functions $\langle\nu_{fk}|$ and $\langle\nu_{ik}|$ with occupation numbers ν_{fk} and
ν_{ik} for final and initial state, respectively. Recalling the basic prop-
erties of the harmonic oscillator we realize that the matrix element
is only nonzero for the mode k if $\nu_{fk} = \nu_{ik} \pm 1$ holds. Exactly this
describes Stokes and anti-Stokes scattering, respectively. We follow
the fluctuation-dissipation theorem and introduce the retarded ther-
mal Green's function G to replace the classical Raman response func-
tion $\epsilon(\omega, \mathbf{q})$. The Raman intensity [174,190] I_{Raman} is calculated similar
to equations 2.15 and 2.16 and yields

$$I_{\text{Raman}} \propto \frac{\partial\sigma^2}{\partial\Omega\partial\omega} \propto (\boldsymbol{\varepsilon}_s \cdot \boldsymbol{\varepsilon}_l)^2 [1 + n(\omega)]\Im G \qquad (2.17)$$

with the frequency of the scattered ω_s and laser ω_l light. The Bose-
Einstein thermal distribution $n(\omega)$ is given as

$$n(\omega) = \frac{1}{\exp\frac{\hbar\omega_p}{k_{\text{B}}T} - 1} \qquad (2.18)$$

with the frequencies of the phonon mode $\omega = \omega_p = \omega_l - \omega_s$, the reduced
Planck constant $\hbar$ and the Boltzmann constant k_{B}[4].

Before moving on to details on Stokes and anti-Stokes scattering,
one word of caution concerning the cross sections that are actually mea-
sured in a Raman experiment. It is important to realize that $\frac{\partial\sigma^2}{\partial\Omega\partial\omega}$ in
equation 2.17 gives the power cross section, i.e. the ratio of scattering to
incident power. However, photon counting devices, such as the charge-

---

[4]We have omitted a detailed derivation of the absolute Raman intensity, as
we will mostly focus on the comparison of Stokes and anti-Stokes intensities to
determine the temperature of the investigated samples.

coupled device (CCD) detector in Raman scattering experiments, measure the quantum cross section $\left(\frac{\partial\sigma^2}{\partial\Omega\partial\omega}\right)_{\mathrm{Quantum}}$. The quantum cross section is defined as the ratio of scattered to incident photons: N_s/N_i. Using the relation between photon number N, time t and power P: $P = \frac{\hbar\omega}{t}N$, the quantum cross section can be expressed as

$$\left(\frac{\partial\sigma^2}{\partial\Omega\partial\omega}\right)_{\mathrm{Quantum}} = \frac{N_s}{N_i} \propto \frac{P_s}{P_i}\frac{\omega_l}{\omega_s} \propto \omega_s^3\omega_l \tag{2.19}$$

where we used the well-known expression $P_s/P_i \propto \omega_s^4$ from Rayleigh scattering (c.f. equations 2.15 and 2.16). Therefore, quantum and power cross section are proportional to ω_s^3 and ω_s^4, respectively. The scattering rates (proportional to the quantum cross section) of the Stokes R_{S} and anti-Stokes R_{AS} side of the spectrum follow the Bose-Einstein thermal distribution $n(\omega)$. Therefore the scattering rates can be expressed as $R_{\mathrm{S}} = A[n(\omega) + 1]$ and $R_{\mathrm{AS}} = An(\omega)$, respectively. A is a constant taking into account all experimental details. Therefore, the ratio of the Raman scattered photons of Stokes and anti-Stokes processes can be written as [173, 174]

$$\frac{I_{\mathrm{AS}}}{I_{\mathrm{S}}} = \frac{(\omega_l + \omega_p)^3}{(\omega_l - \omega_p)^3}\exp(\frac{-h\omega_p}{k_{\mathrm{B}}T}) \tag{2.20}$$

Based on this relation, one can determine the *in-situ* temperature T at the laser spot of the sample investigated. We will exploit this concept in Chapter 5.

The theoretical excursion to the fundamentals of light scattering has shown us that RIXS and Raman scattering are complementary techniques. We have realized that RIXS might be more powerful to investigate TMO due to the **q** resolution and resonant enhancement. However, it is also obvious that Raman scattering offers the somewhat simpler interpretation relying on rather intuitive selection rules. In addition, Raman scattering is more mature as it benefits from a longer history resulting in technical advances and simplifications. Therefore,

Raman scattering is used already in chemistry and material science and even in some industrial applications for quick feedback. Undoubtedly, a combination of both techniques allows us to study elementary excitations of a wide range which can give valuable insight into the exciting physics of TMOs.

2.2 Experimental aspects of light scattering

We turn now to the description of the experimental setup for Raman scattering and RXS. We will in particular review the generation of x-rays using synchrotrons and ways to analyze scattered photons in an energy-resolved fashion. The basic setup for any light scattering experiment is conceptually quite simple and contains three main components: a light source, the sample, and a detector. However, in real life, each of those components constitute complex apparatuses, requiring a high degree of engineering to facilitate a successful experiment, in particular for RIXS experiments.

Before moving to the detailed description of the experimental setups, we point out the difference between resonant inelastic and elastic x-ray scattering. Both experiments require a synchrotron light source to generate x-rays with variable energy to tune to the resonant edges of different TMOs. The main differences between RIXS and REXS become apparent in the detection of the scattered photons. As stated before, RIXS detects the scattered photons in an energy-resolved way using a spectrometer, which will be discussed in Section 2.2.2 below. In contrast, the REXS techniques measures the scattered photons using a diode, *i.e.* all photons irrespective of their energy are detected. It is therefore more appropriate to think of REXS as an energy-integrated technique. This conceptually fine difference in the two techniques result in a quite different experimental setup, where the REXS setup offers by far more simplicity and flexibility. However it is also obvious, that the dispersion of collective excitations can only be studied
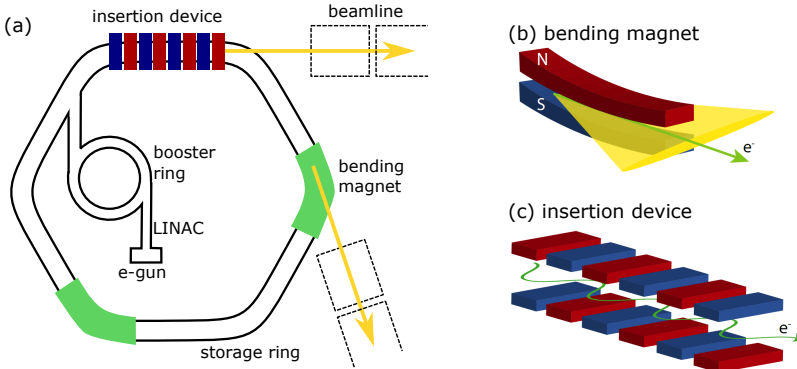
Figure 2.4: (a) Schematic setup of a synchrotron with the main components: electron gun (e gun), linear accelareator (LINAC), booster ring,
storage ring with bending magnets and other insertion devices, and
the beamline comprising the optics and the experimental hutch. Electron trajectory and emission profile for a bending magnet (b) and an
insertion device (c), respectively. Panel (b) and (c) are from Ref. [51].

using inelastic techniques such as RIXS and Raman scattering. We
recommend Ref. [191] for a detailed discussion on a REXS setup, and
continue to review key components of the two inelastic photon experiments. In particular, we emphasize differences between photons in the
x-ray (RIXS) and visible (Raman) range, and discuss implications on
the experimental realization.

2.2.1   Synchrotron radiation

Resonant x-ray spectroscopy and scattering techniques require synchrotron radiation for several reasons. To exploit the resonant nature
of RXS techniques, the photon energy needs to be tunable to a core
level resonance. This can only be achieved by the use of a synchrotron
light source and is not feasible using a standard monochromatic x-ray
source such as a Cu anode. In addition, we recall that RIXS is a second-
order process, which is extremely photon hungry. Therefore RIXS can

only be performed at an advanced light source that offers a variable-polarization monochromatic x-ray source with high photon flux. The RIXS experiments presented here are only feasible at modern third-generation synchrotron facilities, such as the European Synchrotron Radiation Facility (ESRF) in Grenoble, and free-electron lasers. Further, our experiments aim to detect small modulations of the low-energy electronic degrees of freedom, which is quite challenging and in some cases only feasible with extremely high-brilliance radiation. The term "brilliance" describes the spatial and spectral distribution of the photon flux and is usually used to compare different x-ray sources [51,171,172].

In particular, the relativistic speed of the electrons circulating in the storage ring (see Fig. 2.4) enables the high brilliance of synchrotron radiation. First, the high intensity radiation results from the rapidly increasing power emitted by a charge, which moves on a circular orbit with a kinetic energy in the relativistic regime. Second, Lorentz contraction squeezes the dipole radiation in a narrow beam tangential to the electron trajectory with an opening angle of about γ^{-1} rad, where γ is the Lorentz factor. In consequence, synchrotron radiation is highly focused and intense.

The basic setup of a synchrotron is shown in Fig. 2.4 (a). Electrons from an electron gun (e-gun) are pre-accelerated at the linear accelerator (LINAC) and inserted into the booster ring, which accelerates the electrons to relativistic speeds (typically in GeV energy range). After the injection into the storage ring, electrons are driven using radio-frequency cavities and are kept in a stable orbit using dipole and quadrupole magnets. Magnets and periodic magnetic assemblies, also called insertion devices, modulate the beam trajectory and lead to the emission of x-rays, which are then guided to the beamlines. Common insertion devices include bending magnets, wigglers, and undulators. An undulator comprises a periodic assembly of magnets that creates a field which focuses electrons on undulating paths. The oscillating electrons emit highly-focused electromagnetic radiation. In contrast

to wiggler and bending magnets, undulators have a discrete emission
spectrum, and offer higher intensities due to the constructive interfer-
ence of radiation. In addition, the use of undulators offers the possi-
bility to tune the polarization of the emitted x-rays[5]. The polarization
can be modified by changing the shift of different magnetic rails placed
next to each other. In particular, a shift of 0° (90°) gives linear (cir-
cular) polarization. To select a specific energy, for example the Ni L_3
edge, the amplitude of the oscillation of the electrons in modified. This
is in practice done by altering the gap between magnetic rails. Modern
synchrotron facilities, such as ESRF and BESSY II, have spatial un-
dulator periods in the cm range which create x-rays with wavelengths
down to the sub-nm range [172, 192, 193].

The generation of highly brilliant x-ray photons is common for dif-
ferent beamlines of a synchrotron radiation facility. Individual beam-
lines then use these photons for a variety of different experiments,
ranging from imaging setups for molecules to advanced scattering tech-
niques, such as RIXS. We turn now to the description of a RIXS beam-
line, with particular focus on the detection of the scattered photons.

2.2.2   RIXS setup

The key components which need to be considered in an inelastic soft
x-rays experiment are: the x-ray (light) source, *i.e.* the synchrotron
as explained in section 2.2.1, the experimental chamber and the heart
of the RIXS experiment, the spectrometer. Due to high absorption of
soft x-rays even in air the whole beam path needs to be in vacuum.

The RIXS experiments discussed in Chapter 3 of this thesis were
taken at the new ERIXS spectrometer at the ID32 beamline at the
ESRF located in Grenoble, France. The spectrometer and beamline
were specifically designed for RIXS experiments in the soft x-ray regime.

---

[5]Common undulators such as APPLE type undulators comprise four magnetic
rails with adjustable gap and shift. APPLE type undulators have both top and
bottom rails split into two, with the ability to shift them relative to each other.

The ultimate goal of this project was to build the "best" RIXS setup available to date in terms of energy resolution. The instrument was designed and developed by the ESRF in collaboration with the RIXS pioneers Giacomo Ghiringhelli and Lucio Braicovich from Politecnico di Milano. In October 2014, the ERIXS spectrometer was opened to users offering a combined resolving power of $E/\Delta E = 30000$, thereby promoting the ERIXS spectrometer to the world leading instrument of its kind. At the Cu L_3 edges ($\approx 930\,\text{eV}$ to $950\,\text{eV}$), ERIXS routinely achieves an energy resolution better than $60\,\text{meV}$, which can be further boosted to $35\,\text{meV}$ in high-resolution mode[6]. The energy resolution and the possibility to fully and continuously map out 3D dispersions qualified this instrument to the only available end-station to date to measure the dispersive spin exciations in $R\text{NiO}_3$, as shown in Chapter 3.

We will now discuss some important details of the ID32 beamline and ERIXS spectrometer following Refs. [194,196], which are more extensive on this topic. Both, end-station and spectrometer, reflect the goal to maximize energy resolution. A big caveat in the soft x-ray regime comprises the design of energy dispersive elements, which are needed for both the monochromater and the spectrometer. The use of single-crystals, as in the case of hard x-rays with shorter wavelength λ, is not possible [196–198]. Instead, one has to resort to gratings with lower efficiency. In the soft x-ray range, variable line spacing (VLS) gratings with a fixed radius curvature are used, as the line width broadening can be minimized by re-positioning the grating.

Following the beampath from the light-source, the beamline is equipped with a VLS Plane Grating Monochromator (PGM) to minimize energy broadening of the incoming beam. The sample is positioned in the scattering chamber on a full in-vacuum 4-circle sample goniometer. The scattered photons are then analyzed by the spectrometer. In a simplified consideration, the length of the spectrometer (= distance from

---

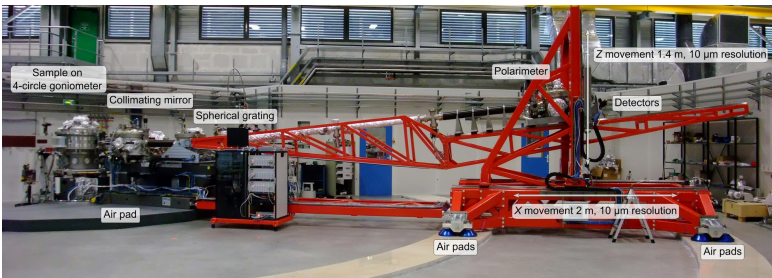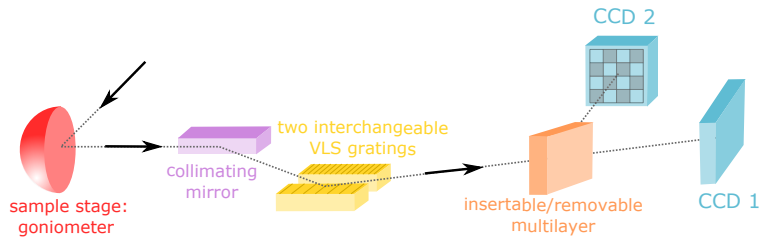[6]The two configurations are explained and discussed below and in Fig. 2.5.

Figure 2.5: Schematic and photograph of the ERIXS spectrometer at the beamline ID32 of the ESRF synchrotron in Grenoble, France. The dashed line in the upper part shows the beampath from the sample stage via the optical components of the spectrometer to the CCD detector. The schematics is reproduced following Ref. [194], and the photograph is taken from Ref. [195].

the energy dispersive element, *i.e.* grating, to the detector) is inversely proportional to the bandwidth of spectrum. Therefore, rather long spectrometer arms are needed for good energy resolution. The ERIXS spectrometer features a 11 m long scattering arm capable of rotating over 100° without breaking vacuum using differentially pumped seals (see Fig. 2.5). The first part of the spectrometer arm incorporates a collimating parabolic mirror and two interchangeable VLS spherical gratings with different groove densities. Both VLS gratings work in the first internal diffraction order. One VLS grating is optimized for efficiency (grating 2), the other one for resolution (grating 1). The scattered and dispersed photons are then detected with two CCD cameras at the end of the spectrometer chamber. One CCD camera measures the direct beam and the other one the beam diffracted from a multilayer that acts as polarimeter. Finally, it is worth to mention that recently Fumagalli *et al.* demonstrated a full polarization analysis of a RIXS spectrum using this newly developed polarimeter [199]. This study demonstrates the potential of RIXS to discriminate excitations according to their nature, in analogy to the selection rules, that are fundamental and powerful in Raman scattering.

The unique ERIXS setup presented above enables the measurements of previously invisible features. In addition, the ERIXS spectrometer serves as a blue print for many other spectrometers, that are currently being built at different synchrotrons around the world. This novel tool has helped RIXS to mature, increase its popularity, and become an important tool to characterize TMOs and their heterostructures. We will use the unprecedented capabilities offered by ERIXS to map out the magnetic dispersion in RNiO$_3$ (see Chapter 3).

2.2.3 Raman scattering setup

While conceptually the key components of the Raman setup are the same as the ones from the RIXS experiment, the use of visible light simplifies the technical design in the case of Raman scattering. The
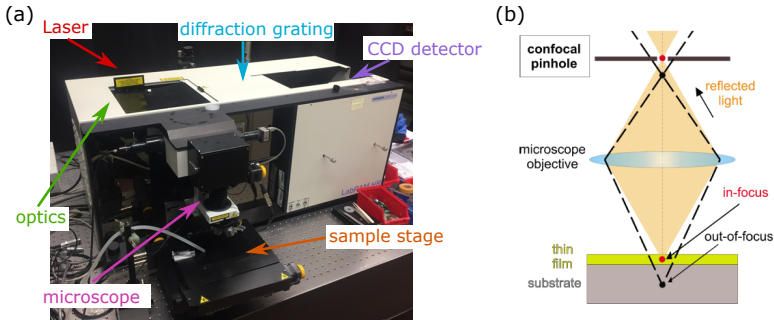
Figure 2.6: (a) Photograph highlighting key components of the Raman setup (Horiba Jobin Yvon LabRAM HR800). (b) Schematic illustration of the confocal z-scan technique to probe thin films comprising TMOs. Panel (b) is taken from Ref. [123].

Raman experiments presented in Chapter 5 were performed on a commercially available Horiba Jobin Yvon LabRAM HR800 spectrometer, which is an integrated micro Raman system. Micro Raman setups use objectives to focus the laser light and are therefore suited for laterally small samples such as the Ca_2RuO_4 single crystals. In contrast, macro Raman setups usually require sampling volumes in the cm^3 range. The diameter of the laser spot in our micro-Raman setup is $1.4\,\mu m$. Raman scattering is a bulk sensitive probe, where the probing depth is given by the penetration depth of the laser beam. The penetration depth for a red laser in TMOs such as Ca_2RuO_4 is around $3\,\mu m$.

The Raman experiments were performed using the 632.8 nm excitation line of a HeNe laser. Standard optical components such as an Iris and a clean-up filter are inserted in the beam path to suppress any additional laser lines. To facilitate the polarization analysis described in the theory section, we use a Fresnel rhomb that rotates the polarization plane of the linearly polarized beam. Further, a holographic notch filter reflects the beam towards the microscope, where an objective (standard objective with 50x magnification) focuses the laser beam onto the sample. All spectra are taken in backscattering geometry with

the incident and the reflected light parallel to the normal of the sample surface. The objective to focus the laser light onto the sample is then also used to collect the scattered light, which further passes the notch filter as well as the confocal pinhole and is analyzed at the spectrograph. A polarization analyzer and ultra-low frequency filter can be inserted to the beam path to selectively probe lattice vibrations with specific symmetry and to suppress the elastically scattered light, respectively. In particular, two volume Bragg-grating filters facilitate measurements down to small wavenumbers, thereby providing information about low-energy excitations. In addition, the ultra-low frequency filter enables to simultaneously record the Stokes and anti-Stokes part of the spectrum, which is crucial for the temperature determination in Chapter 5. The spectrograph employs two line gratings with different line densities as energy dispersive elements and a CCD camera to detect the photons.

To measure thin and ultra-thin films comprising TMOs, we use the confocal pinhole incorporated into the Raman setup [123] (see Fig. 2.6). The confocal pinhole in front of the detector suppresses out-of-focus light, effectively increasing the sensitivity in z-direction (*i.e.* the out-of-plane direction). Thereby, a separate measurement of thin film and substrate (after some subtraction procedure as detailed in Refs. [123, 200]) is possible.

For Raman experiments below room temperature, we use a commercially available KONTI cryostat from CryoVac. As the cooling procedure turns out to be crucial to observe the current-stabilized nonequilibrium phases in Ca_2RuO_4, we give details about the sample mounting and cooling system used in our experiment. In Fig. 2.7 (a), we highlight the path of the He flow as well as the cables which were installed to apply a DC current to the sample. In panel (b) of Fig. 2.7, we schematically illustrate the sample mounting using GE varnish, which electrically isolates the sample from the metallic sample holder while at the same time providing good thermal contact to the latter. The sample holder essentially acts as a cold finger. The sample is contacted
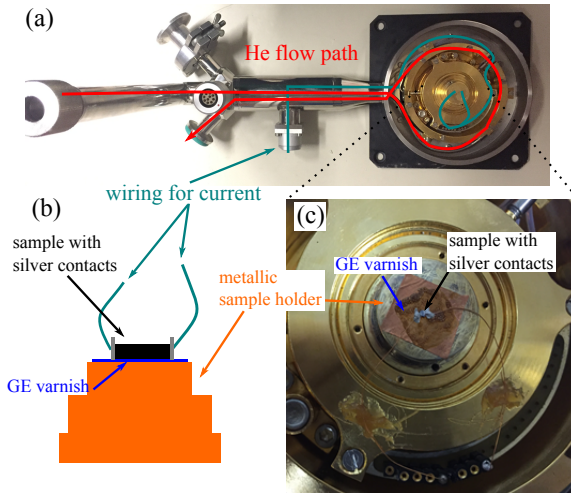
Figure 2.7: (a) Photo of the Raman cryostat with highlighted He flow path (red) and electrical sample wiring (green). (b) Schematics of the sample mounting on the metallic sample holder. (c) Detailed photograph of the sample mounted in the cryostat.

to standard Cu wires with conductive silver paint.

2.3   Analysis of measurements

Equipped with a basic understanding of light scattering in solids and knowledge of the experimental setup, we now move to the analysis of the measured data. We first discuss different line shapes in light scattering data. In the second part, we illustrate two theoretical approaches to extract fundamental microscopic parameters from measured data. This review should by no means be considered as complete guide, as there are many different ways to analyze spectroscopic data. Rather, we give a flavor of what is possible (as an experimentalist) and introduce important concepts that will become important later in Chapters 3 to 5, where the results of this thesis are presented.

2.3.1 Line shapes

While most of the focus in scattering and spectroscopic experiments lies on the energy and momentum of the emitted photon, also the shape of the spectral line can contain important information. In photon scattering experiments the emitted light can be described by an emission from a damped oscillator with base frequency ω_0, that would for example correspond to the frequency of a vibronic mode. The corresponding line shape is expressed as Lorentzian and has the from

$$L(\omega, \omega_0, \gamma) = \frac{2A}{\pi} \frac{\gamma}{4(\omega - \omega_0)^2 + \gamma^2} \tag{2.21}$$

where γ and A give the full width at half maximum (FWHM) and the area of the peak, respectively. The Lorentzian is the fundamental line shape of the absorption of emission and is therefore also called *natural* line. In addition to the Lorentzian line shape, a spectral line can be further broadened due to thermal and experimental effects, such as limited resolution. In that case the line shape is best described by a Gaussian shape

$$G(\omega, \omega_0, \sigma) = \frac{A}{\omega\sqrt{\pi/2}} \exp{-2(\frac{\omega - \omega_0}{\sigma})^2} \tag{2.22}$$

where σ and A give the FWHM and the area of the peak, respectively. Most commonly however, the spectral shape follows the Voigt profile, comprising a convolution of Lorentzain and Gaussian broadening

$$V(\omega, \omega_0, \sigma, \gamma) = \int_{-\infty}^{\infty} L(\omega, \omega_0, \gamma) * G(\omega, \omega_0, \sigma) d\omega \tag{2.23}$$

Our experimental data is best described by a sum of several peaks, where frequency, line width and area of each peak are optimized from fits to experiments. For symmetric peaks, we use the Voigt line shape to fit the Raman data, where the Lorentzian broadening is a variable (in addition to peak intensity and position) and the Gaussian width is

fixed to the experimental resolution. We have determined the resolution
of the LabRAM HR800 spectrometer to be $2\,\mathrm{cm}^{-1}$ by measuring the
spectrum of a discharge lamp containing Neon gas. In RIXS, most of
the low-energy excitations are resolution limited and we cannot access
the intrinsic line width. Therefore, we have fitted most of the spectra
using a Gaussian function, which reflects the resolution-limit.

We will further identify phonons with asymmetric lineshapes in the
Raman investigation in Chapter 5. Phonon asymmetries are known to
result from interactions with a continuum. The phonon asymmetry can
be obtained from fits to a Fano profile [201]

$$F(\omega, \omega_0, \Gamma) = A\frac{(q + \epsilon(\Gamma))^2}{1 + \epsilon(\Gamma)^2} \tag{2.24}$$

with $\epsilon(\Gamma) = {}^{(\omega - \omega_0)}/_{\Gamma}$. Besides the phonon frequency ω_0 and the effective
phonon linewidth Γ, we can extract the Fano parameter q whose inverse
is directly proportional to the electron-phonon coupling strength and
the imaginary part of the electronic susceptibility [202, 203].

The linewidth extracted from fits to the experimental data therefore
give insight into macroscopic electronic properties, such as correlation-
length, electron-phonon coupling, and many more. We now move to-
wards a more theoretical analysis scheme of spectroscopic data, in par-
ticular we show how resonant data can be used to extract important
electronic features of the investigated TMOs.

2.3.2   Theoretical toolkit for an experimentalist

Cluster calculations

As discussed in Chapter 1, the full many-body Hamiltonian of TM ions
can only be solved using approximations. The Hubbard Hamiltonian
presented in equation 1.1 is a rather coarse and fundamental approxi-
mation, but nevertheless offers important insights into electron corre-
lations. Among other auxiliary systems, cluster calculations develop

several symbiotic effects to study the physics of TMOs in a powerful combination with resonant scattering and absorption techniques at the L edges of TMs [54, 171]. In a cluster calculation, the material is approximated by its fundamental building block, the TM-O_6 octahedra. The fundamental principle of this approximation can be found in the multiplet ligand field theory (MLFT), which was originally developed in quantum chemistry. The model Hamiltonian includes the d and $2p$ orbitals of the TM ion to capture the resonant transition and the ligand orbtials L, which comprise in most cases the $2p$ orbitals of the oxygen ions. The description of the solid is consequently condensed into a selection of relevant orbitals of one TM-O_6 octahedra. This approach seems to be crude in the first place, but offers the possibility to explicitly include the entire electron–electron repulsion Hamiltonian. Therefore electron correlations as well as the full multiplet structure of TMOs can be reproduced. In addition to the electron-electron interaction, the basic Hamiltonian in cluster calculations can contain crystal field effects, hopping between oxygen ligand $2p$ and TM $3d$ orbitals, and SOC of the TM $2p$ states and the core hole. In particular XAS spectra could be calculated in excellent agreement with experimental data. Thereby, cluster calculations have proven to be very useful to extract microscopic parameters, which are relevant to describe the electronic structure and corresponding physics of TMOs [47, 109].

Another advantage of cluster calculations is that initial and final state are considered on equal footing, which is important for the comparison to experiments. More specifically, the rather sharp core level absorption lines cannot be explained by transitions into delocalized $3d$ bands. It is necessary to consider the excited state (after the absorption of a photon) as localized state due to the strong excitonic interaction of core hole and excited electron [36, 54].
A standard MLFT Hamiltonian has the from [6, 53]

$$\mathcal{H}_{\mathrm{MLFT}} = \mathcal{H}_U^{dd} + \mathcal{H}_U^{pd} + \mathcal{H}_{\mathrm{SOC}}^d + \mathcal{H}_{\mathrm{SOC}}^p + \mathcal{H}_{\mathrm{on-site}}^{d,p,L} + \mathcal{H}_{\mathrm{int}}^{dL} \qquad (2.25)$$

where $\mathcal{H}_U^{dd}$ and $\mathcal{H}_U^{pd}$ are the Coulomb interaction as anticipated by the Hubbard Hamiltonian (equation 1.1) between two d electrons and between d electron and $2p$ core hole, respectively. Spin-orbit coupling of the d spins ($2p$ core hole) is included via the term $\mathcal{H}_{\mathrm{SOC}}^d$ ($\mathcal{H}_{\mathrm{SOC}}^p$), where the SOC Hamiltonian is explicitly given in equation 1.3. Further, we include $\mathcal{H}_{\mathrm{on-site}}^{d,p,L}$ to take the orbital-selective on-site energies of d, $2p$ and L orbitals into account. $\mathcal{H}_{\mathrm{int}}^{dL}$ describes the $d-L$ hybridization, *i.e.* hopping between TM d and ligand $2p$ orbitals. In the given form, $\mathcal{H}$ can be solved using exact disorganization, which is for example implemented in programs such as Quanty [46, 204, 205].

While it is most common to use a single TM-O_6 cluster to describe the solid, we will extend the theory towards two cluster following Ref. [6] in Chapter 3. In this way we can replicate the essential building block of the bond-disproportionated phase in RNiO$_3$.

Spin wave theory

As shown in Chapter 1, magnetism is one of the key features of TMOs. We recall the AFM ground state of the undoped parent compound in high-T_c cuprates, that have stimulated great interest in the quantitative understanding of quantum AFM. Experimentally, collective magnetic excitations (spin waves or magnons) and their energy dispersion can be measured using RIXS, Raman or neutron scattering (see 2.1.4). However only the comparison of theoretical models with experimental data provides the possibility to quantify microscopic exchange parameters, that give detailed insight into the driving mechanism for long-range magnetic order, spin fluctuations, magnetization dynamics, etc.

An appealing treatment of long-range magnetic order on the basis of elementary excitations of coupled spin systems, so-called spin-waves, was developed in the 1950's [206, 207]. In this scheme, low-energy quantum effects contribute in a semiclassical way as time depended fluctuations around the classical ground state, while spin wave dispersions can be obtained using equations of motions. However, the description

of AFM in TMOs calls for a full quantum mechanical treatment of spin waves with the possibility to include and treat incommensurate magnetic structures, which was put forward by Toth [208]. Here the ground state and spin wave dispersion are the same as in the classical treatment. The elementary excitations however are treated as quasiparticles (magnons) with bosonic character. The spin system is therefore described as coupled harmonic oscillators using second quantization of bosonic operators [209].

The main mechanism for interacting spins in TMOs is the exchange interaction[7], which justifies the use of the quantum mechanical spin-only approximation. Therefore, in spin wave theory the magnetic properties are condensed into a Heisenberg-like (see equation 1.2) magnetic Hamiltonian of localized interacting moments $\mathbf{S_i}$ and $\mathbf{S_j}$ on a periodic lattice with sites i and j, respectively

$$\mathcal{H}_{\text{spin wave theory}} = \sum_{i,j} \mathbf{S_i} J_{ij} \mathbf{S_j} + \sum_i \mathbf{S_i} A_i \mathbf{S_i} + \mathbf{B} \sum_i g_i \mathbf{S_i} \qquad (2.26)$$

The Hamiltonian captures the exchange coupling described by the matrix J_{ij}, the single-ion anisotropy A_i and possible interactions with an external magnetic field $\mathbf{B}$, where g_i is the g- (or Landé) factor. The 3x3 matrix J_{ij} can include Heisenberg [210], Dzyaloshinskii-Moriya and other anisotropic exchange mechanisms. The Hamiltonian given in 2.26 can be solved exactly for example for an antiferromagnetic linear chain of spin $^1/_2$ atoms [211], and even for bulk $R\text{NiO}_3$ it is possible to derive an analytical expression (*c.f.* Chapter 3). For most systems however, and in particular for complex heterostructures described by large magnetic super-cells, numerical methods are necessary, which are implemented for example in the SpinW [208] software package. We will show in Chapter 3 how one can use spin wave theory to extract the microscopic exchange interactions from dispersive spin excitations measured

---

[7]The exchange interaction dominates over the dipole-dipole coupling, as the wavelength of the spin waves is comparable to the distance between two spins.

by RIXS.

Chapter 3

RIXS study of bond order and spin excitations in $R\mathrm{NiO_3}$ with $R=$ La, Pr, Nd

As we have seen in Chapter 1, Section 1.3, $R\mathrm{NiO_3}$ host several collective intertwined ordering phenomena. For a systematic study, we therefore seek to investigate bond and magnetic order simultaneously and on the same footing. We point out that the magnetic ordering in $R\mathrm{NiO_3}$ has been subject to investigation for decades, and still its underlying mechanism remains a puzzle. One of the main obstacles to understand the magnetism of $R\mathrm{NiO_3}$ lies in the characterization of different local spin states of the two inequivalent Ni sites and their associated exchange interactions. Here we take advantage of high-resolution RIXS to probe direct signatures of Ni-O bond order and fluctuations in high-energy interband ("dd") transitions, and to investigate collective spin excitations in both bulk $R\mathrm{NiO_3}$ and heterostructures exhibiting magnetic

states different from those in the bulk. After decades of research on the electronic phase behavior of RNiO$_3$, these experiments can finally determine the magnetic exchange interactions and hence yield unprecedented insight into the mechanism driving the formation of the unusual magnetic structure in this system.

After introducing sample details and developing the theoretical double-cluster model, we quantify the bond order amplitudes for different thin films and heterostructures and discriminate short-range bond order fluctuations from long-range static order. We proceed to study the magnetic order, where we first develop a hitherto missing, complete site-selective description of the magnetism in bulk RNiO$_3$, based on the observation of dispersive magnetic excitations. We further investigate magnetic order and exchange interactions in spatially confined RNiO$_3$ slabs by probing dispersive magnon excitations. Our study of super-lattices (SLs) grown in the [001] direction of the perovskite structure reveals a robust noncollinear spin spiral magnetic order with dispersive magnon excitations that are essentially unperturbed by bond order modulations and spatial confinement. In contrast, we find magnons with flat dispersions and strongly reduced energies in SLs grown in the [111] direction that exhibit collinear magnetic order. These results give insight into the interplay of different collective ordering phenomena in a prototypical $3d$ transition metal oxide and establish RIXS as a powerful tool to quantitatively study several order parameters and the corresponding collective excitations within one experiment.

This Chapter summarizes the findings that were published in Y. Lu, D. Betto, K. Fürsich *et al.*, Phys. Rev. X **8**, 031014 (2018) and K. Fürsich *et al.*, Phys. Rev. B **99**, 165124 (2019), which are items 5) and 6) in the List of Publications, respectively.

3.1 Methods

3.1.1 Sample and experimental details

For a systematic and quantitative study of the different ordering phenomena in RNiO$_3$, high-quality RIXS spectra with high-resolution are necessary. We therefore performed the RIXS experiments at the ID32 beamline of the European Synchrotron Radiation Facility using the ERIXS spectrometer [194] introduced in Chapter 2.2.2. As a compromise between reasonable acquisition time and sufficient resolving power, the combined instrumental energy resolution was set to ≈ 50 meV FWHM. For the whole experiment we kept the incident photon polarization parallel to the scattering plane in order to enhance the magnetic response of the system. To measure the dispersive magnetic excitations, we varied the scattering angle in the range from $55°$ to $135°$, which corresponds to a momentum transfer of 0.4 to 0.8 Å^{-1} at the Ni L_3 edge at 853 eV. Additional resonant elastic x-ray scattering (REXS) experiments (see Fig. 3.2) were performed at the BESSY-II undulator beam line UE46-PGM1 at the Helmholtz-Zentrum Berlin.

High-quality thin films and superlattices (SLs) were grown by pulsed laser deposition (see Table 3.1). A 400 Å thick NdNiO$_3$ (NNO) film was grown on a [001]$_{pc}$-oriented SrTiO$_3$ substrate and has been investigated as bulk representative in previous studies [100,122]. A LaNiO$_3$-LaAlO$_3$ (LNO-LAO) SL was grown on a [001]$_{pc}$-oriented LaSrAlO$_3$ (LSAO) and consists of 33 bilayers, each containing two pseudocubic (pc) unit cells (u.c.) of LNO and LAO. PrNiO$_3$-PrAlO$_3$ (PNO-PAO) SLs were grown on [001]$_{pc}$-oriented LSAO and [LaAlO$_3$]$_{0.3}$ × [Sr$_2$AlTaO$_6$]$_{0.7}$ (LSAT), with a $(2\,\text{u.c.}/2\,\text{u.c.}) \times 30$ and $(2\,\text{u.c.}/4\,\text{u.c.}) \times 20$ stacking of PNO and PAO, respectively. A NdNiO$_3$-NdGaO$_3$ (NNO-NGO) SL was grown on [111]$_{pc}$-oriented NdGaO$_3$ (NGO), which corresponds to the [101] direction in orthorhombic notation. The NNO-NGO SL comprises 4 bilayers with 3 u.c. of NNO (16 Å), separated by 2 u.c. of NGO (12 Å). In the NNO-NGO SL the unit cell is defined along the [111]$_{pc}$ direction.

Table 3.1: Overview of sample properties. In the first column we refer to previous experiments on the same or nearly identical samples studied with other techniques. For the NNO-NGO SL, the unit cell is defined along the $[111]_{\mathrm{pc}}$ direction and thus does not correspond to the unit cell used for the samples grown along $[001]_{\mathrm{pc}}$.

Sample	Growth direction	Stacking	$T_{\mathrm{N}}/\mathrm{K}$	Magnetic order	State at $T = 20\,\mathrm{K}$
NNO thin film on STO [100, 122]	$(001)_{\mathrm{pc}}$	-	200	spiral	insulating
PNO-PAO SL on LSAO [123, 124]	$(001)_{\mathrm{pc}}$	2 u.c./2 u.c.	120	spiral	insulating
PNO-PAO SL on LSAT [123, 124]	$(001)_{\mathrm{pc}}$	2 u.c./4 u.c.	140	spiral	insulating
LNO-LAO SL on LSAO [86, 121]	$(001)_{\mathrm{pc}}$	2 u.c./2 u.c	100	spiral	metallic
NNO-NGO SL on NGO [126]	$(111)_{\mathrm{pc}}$	3 u.c./2 u.c.	65	collinear	insulating

Fig. 3.1 shows hard x-ray diffraction data of the investigated SLs. The L scans can be seen in panel (a), (c) and (d), where pronounced Kissing fringes indicate excellent sample quality and sharp interfaces. We show a representative reciprocal space map around the (103) reflection for the PNO-PAO SL with 2/4 stacking grown on LSAT. The most intense peak in the reciprocal space map is from the LSAT substrate, while the film peak can be seen further right and shifted towards higher H values, suggesting partial relaxation of the rather thick sample. The structural characterization of the NNO thin film can be found in Ref. [100]. In addition, we use magnetic REXS to characterize the static magnetism in the NNO-NGO SL following the protocol described previously [86, 126]. The REXS experiments were performed at the UE46 PGM-1 end-station at the Helmholtz-Zentrum Berlin using σ and π polarized light (perpendicular and parallel to the scattering plane, respectively) and energies tuned to the Ni L_3 edge. The resonant x-ray characterization of the NNO-NGO SL on NGO $(111)_{\mathrm{pc}}$ shows collinear magnetic order and a drastically reduced ordering temperature, in agreement with previous studies (Ref. [126] and Chapter
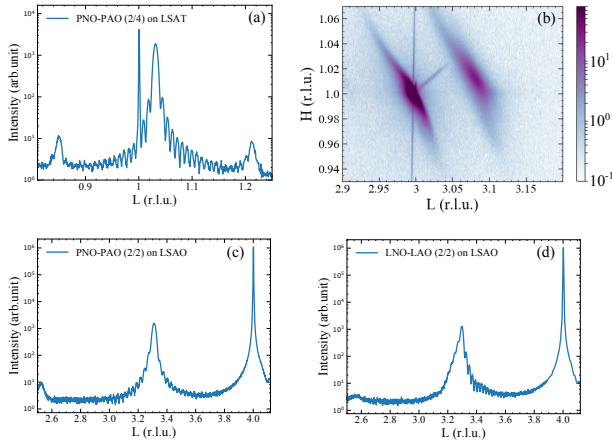
Figure 3.1: Hard x-ray diffraction data for the structural characterization of the SLs. (a) and (b): PNO-PAO SL with 2/4 stacking grown on LSAT. (a) L-scan around the (001) reflection. (b) Reciprocal space map around (103). The most intense peak is from the LSAT substrate at (103). The film peak can be found at higher H and L values, suggestion partial relaxation of the SL. (c) PNO-PAO SL with 2/2 stacking grown on LSAO. L-scan around (004). (d) LNO-LAO SL with 2/2 stacking grown on LSAO. L-scan around (004).
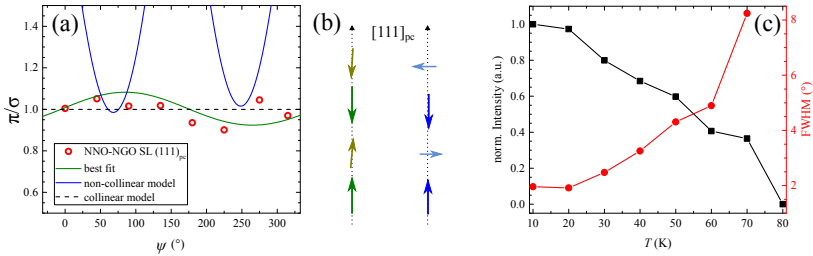
Figure 3.2: REXS study of the NNO-NGO SL. (a) Azimuthal dependence. The data (red points) clearly indicate a collinear alignment of magnetic spins. (b) Sketch of collinear magnetic order and noncollinear spin spiral. To obtain the best fit, we optimized in particular the angle between two neighboring spins. (c) Temperature dependence of the magnetic REXS signal.

1).

3.1.2   Double-cluster calculations

To facilitate the quantitative analysis of our RIXS data, we calculate both XAS and RIXS spectra using the double-cluster model recently developed by Green *et al.* [6]. This model goes beyond the usual exact diagonalization approach based on a single Ni site surrounded by oxygen ligands [46] introduced in 2.3.2. Instead, the double-cluster formalism comprises two NiO$_6$ clusters to explicitly include long-bond (LB) and short-bond (SB) sites, thus reproducing the elementary building block of the rocksalt pattern of alternating octahedra in RNiO$_3$. Each cluster is described by a standard multiplet ligand field Hamiltonian (see equation 2.25) including the full Coulomb interactions and the necessary orbital degeneracies [47,53]. The two clusters are then coupled by hybridization operators with O_h symmetry. The calculations are performed with the exact diagonalization code Quanty [46,204,205].

The double-cluster model considers several key features of the va-

lence electron system of RNiO$_3$, including negative charge transfer energy, Coulomb interactions, orbital degeneracies and bond disproportionation. Importantly, the latter cannot be incorporated in the commonly used single-cluster models. The negative charge transfer picture is essential to reproduce the *self-doped* ground state. As defined in Fig. 1.2, the charge transfer energy Δ_{CT} describes the cost to transfer one electron from the ligand to the TMO 3d band [66, 212]. In RNiO$_3$ Δ_{CT} is negative (see Section 1.3), therefore one hole is doped into the ligand states leading effectively to an O 2p - O 2p gap [75, 78]. We follow the conventions of Refs. [6, 75] and define Δ_{eff} as the energy difference between the top of the ligand band and the bottom of the 3d band. Consequently, Δ_{eff} gives the energy separation of $d^7\underline{L}^0$ and $d^8\underline{L}^1$ configurations in the case of RNiO$_3$. In order to obtain the exact multiplet structure and its spectroscopic fingerprint, it is of crucial importance to include Coulomb interactions as well as orbital degeneracies, as discussed in the literature [36, 54].

The interaction between clusters is quantified by the inter-cluster mixing V_{I}, which is proportional to the ratio between inter- and intra-cluster hopping, that are, respectively, the hopping between the two clusters and within a single NiO$_6$ cluster. In this way charge fluctuations among two neighboring NiO$_6$ octahedra are explicitly incorporated in the formalism. One can thus achieve several configurations beyond those of the classical single-cluster picture, thereby accounting for the highly covalent character of RNiO$_3$. Most importantly, the calculations show that the high-temperature state is dominated by the self-doped $d^8\underline{L}^1$ configuration.

In the low-temperature insulating ground state a bond disproportionation δd is introduced. This parameter is defined as the displacement of the oxygen position along the Ni-O-Ni bonds from the mean value without bond disproportionation, following the definitions in Ref. [6, 100], where the double-cluster approach was employed. For comparison with previous studies, we note that the bond disproportionation can

also be quantified as the difference between short and long Ni-O bond lengths [10,122], which doubles the value of δd compared to our definition. We incorporate the breathing distortion to the model by adjusting mixing and crystal-field terms according to Harrison's rules [94, 213]. Within the double-cluster model the alternating octahedra with $d^8\underline{L}^0$ ($S \approx 1$) and $d^8\underline{L}^2$ ($S \approx 0$) configuration follow naturally.

In the next Sections we use the double-cluster model to calculate XAS and RIXS spectra. Hereafter we introduce the output of the calculations by showing a typical example for the energy ranges and scattering geometries used in this work [Fig. 3.3 (a) and (b)]. For this survey, we use the parameters given in Ref. [100], namely $V_{\text{I}} = 0.33$ and $\delta d = 0.04$ Å at a momentum transfer of $q_{[111]} = 0.211$ [short for $q_{[111]} = 0.211(1, 1, 1)$]. The calculated spectra are broadened to account for experimental resolution and life-time effects. As a first step, we inspect the XAS spectrum to choose the resonant incident energies at which the following RIXS experiment/calculation is carried out. Fig. 3.3 (a) illustrates the Ni L_3 XAS spectra calculated within the double-cluster model. In the nondisproportionated case, we find a two-peak structure at the Ni L_3 edge due to dynamic charge order, $i.e.$ charge fluctuations between the clusters. In the disproportionated state the spectrum consists of contributions from LB and SB octahedra. In the presence of bond order, the two peaks change only weakly, but can now be attributed to strictly different static contributions, with peak A arising predominantly from the LB site and peak B arising almost equally from LB and SB sites [6]. The double-peak structure as well as the small energy shift between zero and nonzero bond disproportionation found in the calculation is a distinct property of RNiO$_3$ [214,215]. Already when considering the XAS spectra, it is evident that the double-cluster model reproduces the experiment [Fig. 3.4 (a)] much better than the conventional single cluster model, which displays only one sharp peak at the Ni L_3 edge [87,109]. Consequently, to obtain an accurate description of the RIXS spectra, which
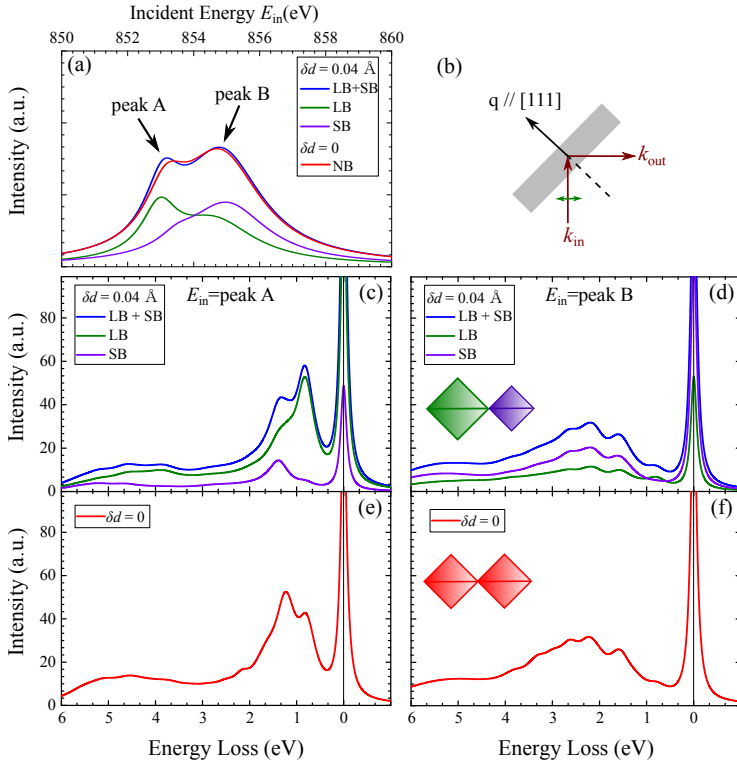
Figure 3.3: Overview of calculated XAS and RIXS spectra within the double-cluster model. Panel (a) gives the theoretical XAS at the Ni L_3 edge calculated with (blue) and without (red) bond disproportionation. The theoretical XAS spectra define the incident energies: peak A and B. (b) Scattering geometry for the RIXS experiment. (c) and (e): RIXS spectrum with incident photon energy tuned to peak A, as defined in panel (a). (d) and (f): RIXS spectrum with incident energy tuned to peak B. Spectra in panels c,d (e,f) were calculated with (without) bond disproportionation. The spectrum for the low-temperature bond-ordered state is the sum of the spectra corresponding to LB (green) and SB (purple) octahedra. The sketches in panels (d) and (f) illustrate the bond order below and above the MIT transition. For clarity, the octahedral rotations are omitted.

exhibit far more details and features, it is essential to adopt the double-cluster model.

We now turn to the discussion of the RIXS calculation. Fig. 3.3 gives an overview of the calculated RIXS spectra within the double-cluster model for both $\delta d \neq 0$ and $\delta d = 0$ (corresponding to low- and high-temperature phases, respectively) as well as for incident energy tuned to peak A and peak B, as defined in the XAS spectra in panel (a). Irrespective of δd, the shape of the spectra measured with incident energy tuned to peak A is quite different from the ones at peak B. While the spectrum at peak A displays sharp features around 1 eV, we identify a broad component around 2 eV at peak B. This observation implies a different origin of the excitations at peak A and B, thereby suggesting coexistence of bound and continuum excitations within one material. Indeed, Bisogni *et al.* [75] attributed the different features to local and band-like excitations by carefully monitoring their energy and temperature dependence. At peak A mostly bound dd excitations are observed, whereas at peak B the RIXS spectrum is dominated by band-like fluorescence decay. In addition, for both incident energies, charge transfer excitations lead to a broad high-energy background around 4 eV.

Firstly, we analyze the spectra calculated with nonzero bond disproportionation describing the insulating low-temperature state. In the bond-ordered phase, the calculated spectrum stems from the sum of the contributions arising from the LB and SB site. To gain a deeper understanding of the energy dependent excitations, we disentangled the contributions from LB and SB octahedra by separately plotting their individual spectra [panels (c) and (d) in Fig. 3.3]. Interestingly, the spectrum measured at peak A consists mostly of contributions from the LB site, corresponding to the expanded octahedron, while the SB site only adds minor spectral weight. Similar conclusions have been reached in Ref. [216]. The distribution of LB and SB contributions changes substantially when tuning the incident energy to peak B. We

find almost equal contributions from LB and SB octahedra, in close analogy to the XAS spectrum at low temperatures.

Secondly, we take a closer look at the temperature dependence of the calculated spectra, exemplified in the comparison between $\delta d = 0$ [high-temperature phase, panels (e),(f)] and $\delta d \neq 0$ [low-temperature phase, panels (c),(d)]. At peak A, we observe changes in the dd excitations around 1 eV. The spectral weight of the double peak structure shifts towards the high-energy side. In stark contrast, at peak B we recognize no obvious difference between zero and nonzero bond order.

From this first overview of the double-cluster calculation, we conclude that clear signatures of bond order can be gleaned from RIXS spectra measured with incident energy tuned to peak A. Therefore, we will focus on spectra measured at peak A in the following sections.

3.2   Quantifying the bond disproportionation in RNiO$_3$

3.2.1   Bond order in RNiO$_3$ films and superlattices with $R \neq$ La

In order to get a systematic overview, we measured a film and three SLs with different periodicities and rare-earth species, specifically Nd and Pr. This allowed us to study the bond order as a function of tolerance factor, *i.e.* rare-earth ion radius, as well as in the limit of two-dimensional confinement. The rare-earth ion radius has a strong influence on the onset temperature and strength of the bond order, as it effectively controls the bandwidth via the Ni-O bond angle and the consequent Ni $3d$ and O $2p$ hybridization [8, 93]. To access the bond order parameter, RIXS is an excellent tool as it is sensitive to dipole forbidden inter-orbital dd excitations, which are strongly influenced by the electronic reconstruction associated with the bond-ordered phase.

Fig. 3.4 (b) shows spectra for two PNO-PAO SLs measured with
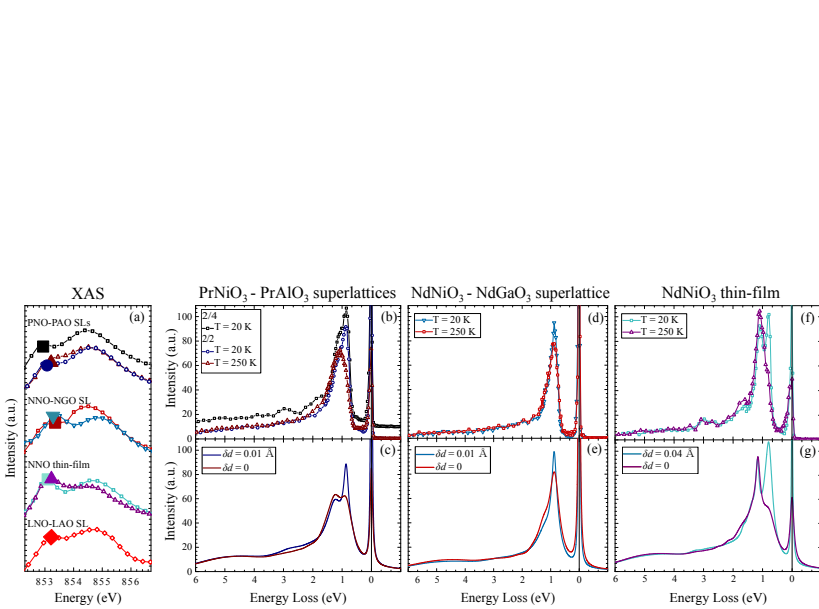
Figure 3.4: (a) XAS spectra for all investigated samples. The enlarged symbol indicates the incident energy for the RIXS experiment, *i.e.* the peak A. For the LNO-LAO SL we subtracted the La M_4 line. (b) RIXS spectra for two PrNiO$_3$-based superlattices with different stacking periodicities. The SL with 2/4 stacking is offset for clarity. (c) Double-cluster calculation for the PNO-PAO SLs. (d) RIXS spectra for the NdNiO$_3$-NdGaO$_3$ SL with the corresponding double-cluster calculation in (e). For both SLs we find a bond disproportionation of $\delta d = 0.01$ Å. (f) Experimental and (g) calculated spectra for a NdNiO$_3$ reference thin film. Panel (f) and (g) are reproduced from Ref. [100].

an incident energy tuned to peak A at $q_{[111]} = 0.211$ for $T = 20$ K and $T = 250$ K. For both PNO-PAO SLs with different stacking periodicity we observe almost identical spectra indicating a similar electronic structure. Comparing these data to the spectra from a NNO-NGO SL and a film [Fig. 3.4 (d) and (f), respectivly] measured in the same conditions, we observe remarkable differences for both the bond-ordered and the non bond-ordered phase. While most of the spectral weight for all systems is centered around 1 eV, the features in the NNO film are much sharper compared to the SLs. Additionally, the double peak structure in the NNO film is more pronounced.

To understand these observations in a quantitative manner, we performed double-cluster calculations as described in Section 3.1. We used the parameters given in Ref. [100] and solely optimized the bond disproportionation δd and inter-cluster mixing V_I to reproduce the experimental data. The calculated spectra that best describe the experimental data are shown in Fig. 3.4, panels (c), (e) and (g).

We first discuss the NNO film as reference for the bulk phase. There we find $V_I = 0.33$ and $\delta d = 0.04$ Å [100]. The bond disproportionation parameter is in excellent agreement with previous values from x-ray scattering at the Ni K edge [122,217] and powder diffraction measurements [218]. The consistency with the literature validates our approach and shows that our method is applicable to RNiO$_3$. We emphasize that the experimental RIXS spectra are much better reproduced with the double-cluster model than with the standard single cluster model, used in Ref. [75] as it allows a quantitative determination of the bond order parameter.

For the PNO-PAO superlattices we find the same value for the inter-cluster mixing $V_I = 0.33$ and a lower bond disproportionation $\delta d = 0.01$ Å in the low-temperature phase. In general, the reduced bond order in bulk PNO can be explained as a consequence of the greater overlap between Ni $3d$ and O $2p$ orbitals, in comparison to NNO, which also reduces the critical temperature for the MIT. Powder diffraction

measurements revealed a bond disproportionation of δd=0.026 Å for
bulk PNO [219]. The even lower value for δd in PNO-based superlat-
tices found here can be attributed to two-dimensional confinement and
pinning of the oxygen positions in the nickelate layers at the interfaces
with the buffer layer, which further increases the bandwidth [87,121].
Raman scattering showed that the bond order in PNO-PAO SLs can be
completely suppressed in compressively strained SLs and a pure metal-
lic spin-density wave was found [79,123]. However, even though the 2/2
PNO-PAO SL investigated in this study is under compressive strain,
we do not observe a complete suppression of bond order. Since RIXS
is a more sensitive probe of bond order than the detection of extra
phonon modes via Raman scattering, it would have been challenging
to conclusively identify the weak bond order distortion reported here in
the Raman experiments. On the other hand, the bond order parameter
is possibly not completely suppressed due to partial relaxation of the
rather thick SL used in the present work (see Fig. 3.1) and in Ref. [220]
compared to the one in Ref. [123].

The bond order amplitude in Nd-based SLs can be greatly reduced
due to spatial confinement, similar to the example of the Pr-based SLs.
As an example we refer to a NNO-NGO SL grown on a $[111]_{pc}$-oriented
substrate shown in Fig. 3.4, panels (d) and (e), where we find a reduced
bond disproportionation of δd=0.01 Å. The different shapes of the dd
excitations in the NNO-NGO SL and the NNO film for $\delta d = 0$ is re-
lated to the different cross sections for the $[111]_{pc}$- and $[001]_{pc}$-oriented
samples [221].

Although thin-films and SLs give rise to completely different shapes
of the RIXS spectra, the double-cluster approach with tuned parame-
ters describes both systems very well (lower panels of Fig. 3.4). This
gives evidence that the double-cluster model, and specifically the nega-
tive charge transfer scenario, is an excellent picture to describe the local
physics in RNiO$_3$ and suggests that holes in the oxygen ligands are a
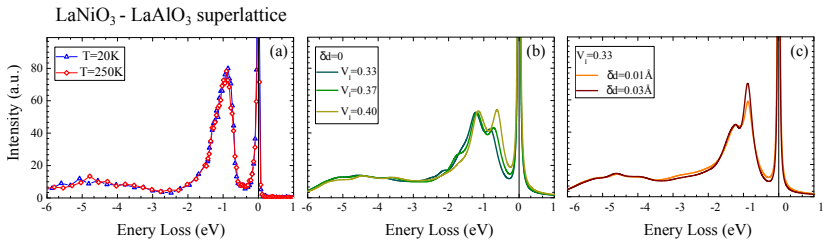key ingredient to understand the MIT. Our approach can be readily

Figure 3.5: (a) RIXS spectra for a LNO-LAO SL. (b) Calculation without bond disproportionation δd and adjusted inter-cluster mixing V_I. (c) Calculation with small bond disproportionation. The spectra calculated with finite δd reproduce the experiment much better. V_I is kept the same as in the PNO and NNO-based samples.

applied to all other RNiO$_3$ with $R \neq$ La, where bond order essentially governs the insulating phase. However, it is interesting to ask whether the double-cluster model can be adopted also for the correlated metal LaNiO$_3$, the only compound in the RNiO$_3$ family which shows no bond order, neither in bulk nor in heterostructures.

3.2.2 Breathing-type fluctuations in LaNiO$_3$

LaNiO$_3$ (LNO) can be considered as an exception among the RNiO$_3$ compounds as it stays paramagnetic and metallic at all temperatures (see phase diagram in Fig. 1.3). This is due to the fact that R=La is the largest rare-earth ion in the RNiO$_3$ family, so that in LNO the Ni-O bonds are rather straight, resulting in an increased hybridization of Ni $3d$ and O $2p$ orbitals. However, it has been demonstrated that by confining the active LNO layers towards a planar two-dimensional limit, one can induce AFM order [121]. This can be viewed as a spin-density wave (SDW) state in the absence of bond order [79, 132].

To gain a deeper understanding of the electronic mechanism inducing the SDW state and to test the double-cluster model against a highly correlated metal, we employ the same approach described in the previous section. The RIXS spectra are measured at peak A with the

scattering vector $q_{[111]} = 0.211$ and for two temperatures, $T = 20\,$K and $T = 250\,$K. As illustrated in Fig. 3.5, the spectrum of the LNO-LAO SL does not evolve with temperature above 1 eV energy loss. Therefore, we can safely exclude long-range static bond order in accordance with our previous resonant diffraction experiments, where no bond order Bragg reflections could be observed at the Ni K edge [122].

Remarkably, the spectra from the LNO-LAO SL are quite similar to those from PNO-PAO SLs at low temperature which could be modeled with small but nonvanishing bond disproportionation. We therefore tried to reproduce the experimental findings by using the same double-cluster model as in Sec. 3.2.1. We account for the larger bandwidth of LNO by increasing the inter-cluster mixing V_{I}, while maintaining the constraint of absent bond order ($\delta d = 0$). The calculation fails to reproduce the experimental RIXS lineshape even on a qualitative level [see Fig. 3.5 (b)]. As a next step, we allowed for small local breathing-distortions $\delta d \neq 0$. The theoretical spectra calculated with nonzero δd reproduce the experiment much better. While some discrepancies between the numerical and experimental data remain, the results support a picture of short-range order in the form of transient bond order-like distortions, $i.e.$ breathing-type fluctuations of the NiO$_6$ octahedra. The bond order fluctuations are observable by RIXS, because they are much slower than the RIXS scattering process itself. A complete quantitative description of the RIXS spectrum in this situation remains a challenge for future theoretical work.

Several independent findings point out the importance of bond order fluctuations in the description of RNiO$_3$, and in particular for $R = $ La [94,132,222,223]. Recent experiments based on the pair distribution function method have found evidence for two nonequivalent Ni sites in LNO even in the metallic phase [224,225]. Some studies even suggest that bond-length fluctuations are present in all RNiO$_3$ at high temperature, thereby classifying the metallic state in RNiO$_3$ as a polaronic liquid. The MIT and the associated bond order can then be ex-

plained in terms of stabilization/freezing of the pre-formed fluctuating rock-salt pattern of octahedra from the metallic state [224]. Additional evidence for charge/bond fluctuations can be found in the Fermi surface superstructure with wavevector $\mathbf{Q}_{\mathrm{BO}} = (1/2, 1/2, 1/2)_{\mathrm{pc}}$ observed by angle resolved photo emission in metallic LNO [226]. Together with our RIXS data, these results suggest that bond order fluctuations are essential for the theoretical description of LNO. Using high resolution RIXS in combination with a double-cluster model, we discriminated between long- and short-range bond order and quantified the bond disproportionation in several examples of RNiO$_3$. In the following we elucidate the effect of different bond order strengths on the spin excitations in RNiO$_3$.

3.3 Spin excitations in RNiO$_3$

As far as collective spin excitations are concerned, one can consider three different cases of magnetic order in RNiO$_3$ compounds, which have been discussed in Section 1.3. For insulating bulk-like films the robust bond order is a prerequisite for the spin spiral that appears at T_{MIT} or lower temperature depending on the rare-earth R [99]. In spatially confined systems, as realized in SLs grown along the $[001]_{\mathrm{pc}}$ direction, the spiral magnetic order can develop with weak or absent bond order [86, 123, 124]. Among this SL family the LNO-LAO is special, as the system remains metallic while developing the spiral order [86, 122]. Additionally, collinear magnetic order can be found in SLs with $[111]_{\mathrm{pc}}$ orientation [126] matching the magnetic propagation vector.

For the investigation of magnetism in RNiO$_3$, we focus on the low-energy part of the spectra already shown in the previous section. We use the same examples from Sec. 3.2 for strong and weak bond order, namely the NNO film and the PNO-PAO SLs with two different stacking periodicities. In addition we compare the spin spiral from the NNO film and the PNO SLs with collinear magnetic order, which can be
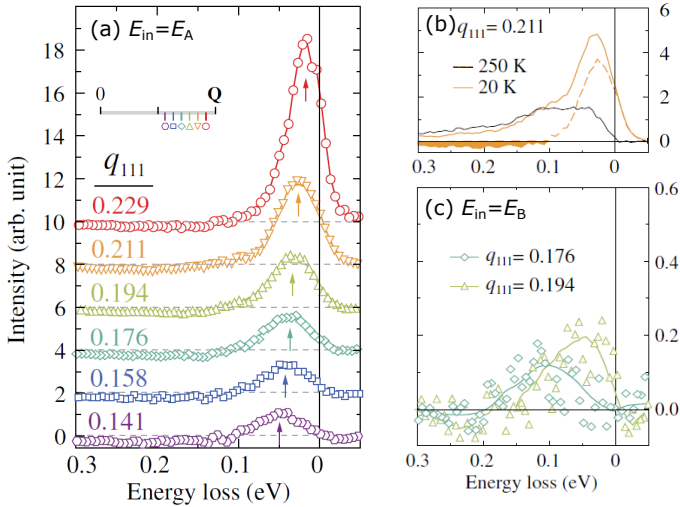
Figure 3.6: (a) Magnon measured at incoming energy $E_{in} = E_A$ tuned to peak A at all measured q_{111} values. The magnon scattering intensity can be obtained by subtracting the nondispersing contribution at high temperatures from the inelastic spectra, as illustrated for $q_{111} = 0.211$ in panel (b). (c) Magnon measured at incoming energy $E_{in} = E_B$ tuned to peak B at all measured q_{111} values.

found in the $(111)_{pc}$ NNO-NGO SL. For RNiO$_3$ with $R=$Nd, Pr bond and magnetic order set in at the same temperature ($T_{MIT} = T_{AFM}$).

3.3.1   NdNiO$_3$ films as bulk representative of RNiO$_3$

We first study the spin-exciations in a bulk-like film, therefore we focus in the following on the RIXS spectra of the NNO thin-film below 0.3 eV. To extract the low-energy excitations, the elastic contribution can be removed by subtracting a Gaussian peak at $\omega = 0$, with FWHM set to the experimental energy resolution of about 50 meV. We proceed to extract the magnetic RIXS spectra by subtracting the nondispersing background measured at 250 K from the spectra at 20 K, as illustrated
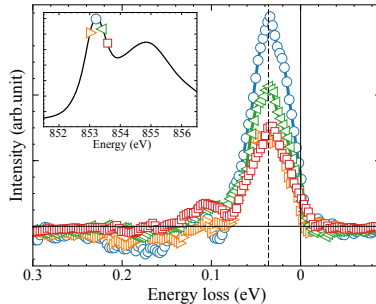
Figure 3.7: Collective spin excitation observed with RIXS. The RIXS spectra are measured at different incident energies E_{in}, which are varied around E_A (peak A). The exact values of E_{in} are marked in the XAS measurements shown in the inset using the corresponding symbol and color of the RIXS spectrum. The energy of the magnon remains constant, *i.e.* Raman-like, as E_{in} is varied around E_A. The data is taken at $q_{111} = 0.176$ and $T = 20\,\mathrm{K}$.

for $q_{111} = 0.211$ in Fig. 3.6 (b). After this, one is left with the magnetic RIXS spectra at each q_{111} for incoming energy tuned to peak A [Fig. 3.6 (a)] and B [Fig. 3.6 (c)]. The magnon excitation energies are obtained from the peak positions of the resulting spectra as indicated by arrows in Fig. 3.6 (a).

First, we discuss the case of incident photon energy tuned to $E_{\mathrm{in}} = E_A$, which is expected to couple dominantly to the spins of Ni_A sites, as suggested by the double-cluster model. The q values range from 0.40 to $0.65\,\text{Å}^{-1}$ in steps of $0.05\,\text{Å}^{-1}$, which correspond to $q_{111} = 0.141 - 0.229$. A clear inelastic contribution peaked at $\omega \leq 50\,\mathrm{meV}$ can be observed at all measured q values. We employ several complementary diagnostic indicators to discriminate between magnon and phonon contributions to the inelastic intensity. First, as magnons become heavily overdamped (and hence nearly invisible to scattering probes) in the paramagnetic state, we compare RIXS spectra well above and well below the AFM ordering temperature. In the paramagnetic state, the spectra exhibit

no noticeable q dependence, as expected for optical phonons [123,189].
In addition, incoherent, local spin-excitations [227] and charge excita-
tions [189] may also contribute to these featureless spectra. In contrast,
the spectra in the AFM state exhibit a prominent, strongly dispersive
feature [indicated by arrows in Fig. 3.6 (a)]. The dispersion emanates
from the AFM ordering wave vector $\mathbf{Q}_{\mathrm{AFM}}$ and exhibits maxima at the
borders of the AFM Brillouin zone, as expected for collective excita-
tions of the AFM state. In addition, the intensity is maximal at $\mathbf{Q}_{\mathrm{AFM}}$
and minimal at the AFM Brillouin zone border, again supporting the
assignment to magnons. The collective nature of the magnetic excita-
tion is further verified by the independence of its energy on variation
of E_{in} around E_A, see Fig. 3.7. We emphasize that the unique energy
selectivity of RIXS allowed us to maximize the cross section of local
excitations by utilizing its relatively large energy separation from the
continuum excitations in the RIXS intermediate state.

Second, we turn to the low-energy spectra measured with $E_{\mathrm{in}} = E_B$,
i.e., the energy that maximizes the RIXS coupling to the magnon ex-
citations associated with the Ni$_B$ sites. Fig. 3.6 (c) shows the magnon
spectra, that is after the subtraction of elastic and high temperature
contribution, along [111] for $E_{\mathrm{in}} = E_B$. Contrary to the data taken
with $E_{\mathrm{in}} = E_A$, where the RIXS signal gains significant weight from
collective magnon excitations, the spectra here are dominated by the
nondispersing contribution. While the remaining spectral weight may
indicate a small contribution from dispersive magnons, the signal is too
weak to be clearly distinguished from the statistical noise. The well-
defined dispersing magnon excitations observed at $E_{\mathrm{in}} = E_A$ and the
nearly null observation at $E_{\mathrm{in}} = E_B$ are in line with the prediction of
the site-resolved spin susceptibilities.

The combined knowledge of the static AFM ordering and the collec-
tive excitations of the Ni moments provides a solid basis — and simul-
taneously imposes stringent constraints — for low-energy spin models
aimed to describe the hitherto unexplained noncollinear magnetic struc-
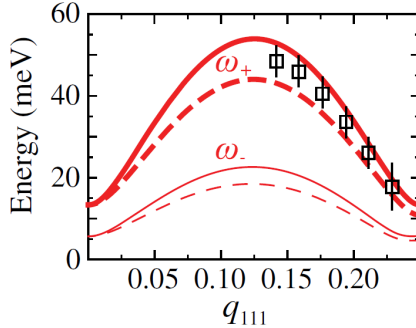
Figure 3.8: Calculated spin-wave dispersion along [111] for two kinds of domains (solid lines for hkl and $\bar{h}\bar{k}l$, and dashed for $h\bar{k}l$ and $\bar{h}kl$). Each includes two branches (thick and thin) due to the disproportionated spins. Open symbols are experimental data from Fig. 3.6 (a).

ture of RNiO$_3$, shown in Fig. 1.5 [86, 99]. We recall that the magnetic structure in RNiO$_3$ comprises ferromagnetic (111) planes that form a noncollinear ($\uparrow\leftarrow\downarrow\rightarrow$) AFM order. The ordering pattern of spins S_A (S_B) residing on the Ni$_A$ (Ni$_B$) sublattice readily follows from AFM superexchange (SE) interactions J_2 and J_4. However, the major question is which mechanism stabilizes the $90°$ mutual orientation of the S_A and S_B sublattices, given that a conventional (Heisenberg) coupling is frustrated and would result (via the "order-by-disorder" mechanism) in a collinear "up-up-down-down" arrangement instead.

We suggest that, near the MIT, low-energy charge fluctuations between Ni$_A$ and Ni$_B$ sites with unequal spins $S_A > S_B$ lead to a double-exchange (DE) process that depends on the angle θ between S_A and S_B. Competition between ferromagnetic DE and AFM superexchange is known to result in noncollinear ordering [210, 228], as recently observed in ferrates [229]. As far as small fluctuations around the classical spin pattern are concerned, one can incorporate the DE energy into the spin-only model [229, 230] from equation 2.26 (Section 2.3.2) with an effective parameter $J_1 = J_{SE} - J_{DE}$ comprising both SE and

DE contributions, where J_{DE} is associated with the kinetic energy due
to low energy charge fluctuations between Ni$_A$ and Ni$_B$ sites. We cal-
culate the magnon dispersions using the $J_1 - J_2 - J_4$ model, including
also a single-ion anisotropy term K, assuming easy axes parallel to
the cubic body diagonals. The spin disproportionation results in two
magnon branches. The disproportionation parameter $\delta d = 0.4$ Å was
chosen consistent with experiment [122] and with the prediction of the
double-cluster model for the experimental value of the bond dispropor-
tionation (Fig. 3.4 and associated discussion). The spin Hamiltonian
contains four adjustable parameters: J_1, J_2, J_4, and K, which can
be obtained by fits to experiment, while respecting some conditions
relating the different parameters. In particular, the experimentally
observed commensurate ordering wave vector implies the constraint
$|J_1| < J_{1c} = 2\sqrt{2K(J_2 + J_4)/3}$. We note that the major magnon
branch is not sensitively dependent on the exact value of J_1. An accu-
rate determination of J_1 requires resolution of the less intense, lower-
energy branch, which is beyond the capabilities of the current setup. In
the fitting procedure, J_1 is therefore varied systematically between its
upper and lower bounds to establish systematic errors for J_2, J_4, and
K. We obtain the following values and errors for the fitting parameters:
$J_2 = 4.1 \pm 1.7$, $J_4 = 8.3 \pm 2.2$, and $K = 1.3 \pm 1.3$ (all units of meV),
which implies $J_{1c} = 6.3$ meV. Figure 3.8 shows the magnon dispersion
calculated with the best-fit parameters and $J_1 = J_{1c}/2 = 3.2$ meV in
compassion with the experimental dispersion extracted from Fig. 3.6
(a) at $E_{\text{in}} = E_A$. For $E_{\text{in}} = E_B$ both calculation and experiment
show strongly suppressed magnon spectral weight. The fitted value of
the anisotropy constant K results in a magnon gap of 13 meV for the
main branch of the dispersion, which is comparable to that observed in
La$_2$NiO$_4$ [231]. However, the magnetocrystalline anisotropy is imma-
terial for our model and interpretation, which addresses the hierarchy
of exchange interactions between the Ni ions. We emphasize once more
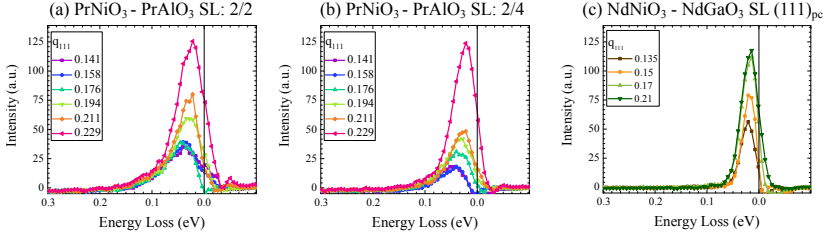that the dominance of the long-range interactions, J_2 and J_4, is a hall-

Figure 3.9: Dispersive magnetic excitations in PNO-based heterostructures after removal of elastic contribution and subtraction of high-temperature data, along the lines of Section 3.3.1. (a) PNO-PAO ($2\,\mathrm{u.c.}/2\,\mathrm{u.c}$) SL on LSAO. (b) PNO-PAO ($2\,\mathrm{u.c.}/4\,\mathrm{u.c}$) SL on LSAT. (c) NNO-NGO ($3\,\mathrm{u.c.}/2\,\mathrm{u.c}$) SL on NGO $(111)_{\mathrm{pc}}$.

mark of the competition between superexchange and double-exchange interactions near the MIT, which greatly reduces the nearest-neighbor interaction J_1.

Our study provides direct insight into the magnetic dynamics and exchange interactions of the rare-earth nickelates and demonstrates that RIXS can serve as a site-selective probe of magnetism in these and other materials.

3.3.2 Thin-film structures of RNiO$_3$

Following the study of magnon excitations in insulating bulk-like films, we focus now on the $(001)_{\mathrm{pc}}$ SLs with spiral magnetic order and reduced bond order, and the $(111)_{\mathrm{pc}}$ SL with collinear magnetic order. We use the approach developed in Section 3.3.1 to measure the dispersive spin excitations in several PNO- and NNO-based heterostructures [100]. To single out the purely magnetic signal, contributions from elastic scattering and other low-energy excitations were subtracted from the spectra. The elastic line is given by a Gaussian peak with FWHM $= 50\,\mathrm{meV}$ (experimental resolution) at zero energy loss. The spectrum measured above the magnetic ordering temperature gives the nonmagnetic low-energy excitations, dominated by phonons.

After subtracting the high-temperature inelastic spectra from the low-temperature inelastic data one is left with well-defined dispersive magnetic features. Magnon dispersions for different stacking periodicities, rare earth ions and substrate orientation can be seen in Fig. 3.9. For all samples, we observe an increase in the magnetic spectral weight as we move towards $\mathbf{Q}_{AFM}$. Moreover, the energy of the spin excitations disperses from approximately 50 meV to 20 meV as the scattering vector gets closer to $\mathbf{Q}_{AFM}$ for the PNO-based SLs, while the magnon bandwidth is clearly reduced for the NNO-NGO SL. This is further illustrated by the extracted magnon dispersion shown in Fig. 3.10.

The variations in the magnon dispersion can be related to the microscopic spin structure. PNO-PAO SLs host the well known noncollinear AFM spin spiral, extensively studied for example by Frano *et al.* [86]. In contrast, the NNO-NGO SL orders in the recently discovered collinear pattern (see Fig. 3.2 and Ref. [126]).

We first focus on the PNO-PAO SLs, which show a spiral state and a similar dispersion as the NNO film, which is representative of bulk RNiO$_3$. Both the ground state and the low-energy excitation spectrum of bulk NNO were explained by a $J_1-J_2-J_4$ model with exchange interactions between nearest-, second-nearest, and fourth-nearest-neighbor Ni spins. J_1 is anomalously small due a strong competition between the AFM super-exchange and the ferromagnetic (FM) double-exchange interactions. The AFM ordering within one sublattice of equally sized octahedra and magnetic moments follows from the J_2 coupling, which is dominated by superexchange interactions. Low-energy charge fluctuations between nearest-neighbor sites lead to a FM double-exchange interaction, which is optimized for an angle of 90° between adjacent spins. The close similarity between the magnon dispersions of the NNO film and of the PNO-PAO SLs shows that the magnetism in the two-dimensional limit can be explained by the model developed for bulk NNO with similar exchange coupling constants (Fig. 3.10). According to this model, the strongest exchange interactions J_2 and J_4 connect
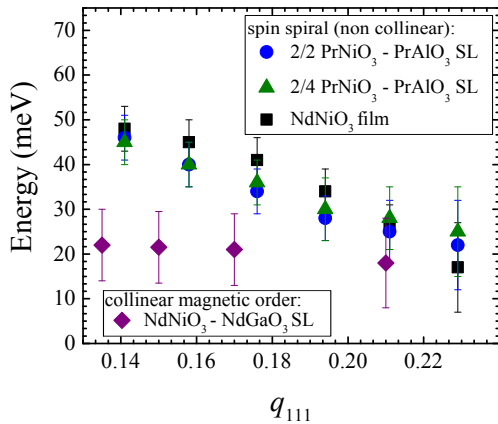
Figure 3.10: Magnon dispersion of PNO-based superlattices compared to the one from the NNO-NGO $(111)_{\text{pc}}$ superlattice (extracted from Figure 3.9). In addition we show the magnon dispersion for the NNO thin film from Fig. 3.8.

spins within the same sublattice of the bond order state, whereas the nearest-neighbor interaction is weaker and does not substantially affect the measured magnon dispersion [100]. The model therefore naturally explains the observed insensitivity of the spin dynamics to the bond order parameter. We therefore conclude that our magnetic model can be applied to a wide range of $R\text{NiO}_3$ thin films and heterostructures with different electronic and structural properties. In particular, the increased metallicity (and bandwidth) obtained from a combination of compressive strain and a larger rare-earth ion does not have a significant impact on the magnon dispersion. The spin spiral in $R\text{NiO}_3$ is thus essentially unperturbed by a modulation of the bond order.

We now proceed to the collinearly ordered NNO-NGO SL, where the magnon energy near the magnetic zone boundary is reduced by a factor of 2 (see Fig. 3.10). According to Ref. [126] the different spin structure is a consequence of truncated exchange bonds along the magnetic ordering vector inherent to the particular SL geometry. We there-

fore construct a magnetic supercell comprising 3 u.c. NNO, separated by the nonmagnetic NGO, stacked along the [111]$_{\text{pc}}$ direction. We start from the magnetic structure determined by the REXS experiments (see Fig. 3.2) as well as the bulk exchange parameters and set the bond disproportionation to $\delta d = 0.01\,\text{Å}$, *i.e.* $S_{\text{LB}} = 0.55$ and $S_{\text{SB}} = 0.45$ as suggested by the double-cluster calculation (see Fig. 3.4). The ground state and the magnetic dispersion are numerically computed using the SpinW software package [208]. The result is shown in Fig. 3.11, where the low-energy eigenmodes are indicated by orange lines. These modes are dispersionless in the [111]$_{\text{pc}}$ direction and their energies are lower than the zone-boundary energy of the bulk dispersion (gray lines). In order to compare the calculated modes to the experimental data, one has to consider the experimental resolution indicated by the gray bar. It is evident that within the current resolution the predicted splitting of the low-energy modes cannot be resolved. However, the overall energy scale and the lack of dispersion in the [111]$_{\text{pc}}$ direction are in good agreement with the model calculation.

In the LNO-LAO SL, where magnetic order was previously observed by muon spin rotation and resonant elastic x-ray scattering [86, 121], we detected an increase in spectral weight upon approaching $\mathbf{Q}_{\text{AFM}}$ both in the elastic and in the inelastic channel, but no dispersive feature. This may be a consequence of heavy damping of the magnon modes by incoherent particle-hole excitations in the metallic sample. We note, however, that these experiments were hampered by strong self-absorption due to the proximity of the La M edge, so that no firm conclusion on the absence of pronounced magnon modes in the RIXS spectra could be reached.

3.4   Conclusions and outlook

In summary, we used high-resolution RIXS to simultaneously probe the bond and magnetic order in a representative selection of RNiO$_3$ thin
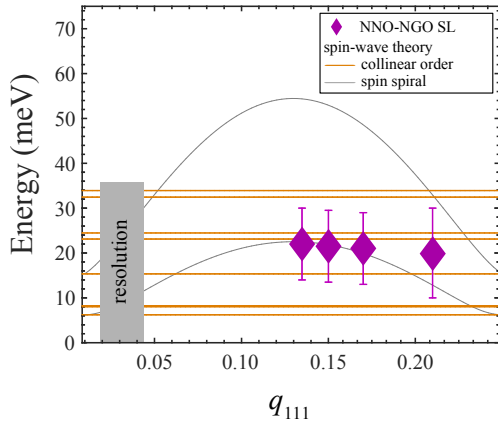
Figure 3.11: Linear spin-wave theory for a collinear magnetic structure. The magnetic supercell comprises 8 ML NNO separated by non-magnetic NGO. Orange lines show the low-energy eigenmodes of this collinear system. The purple diamonds represent the measured data, while the gray box indicates the resolution limit in the RIXS experiment. Gray lines indicate the calculated dispersion of magnons in the spiral state of the bulk-like NNO film.

films and superlattices. Firstly, we showed that RIXS in conjunction with multiplet calculations in the framework of a double-cluster model can serve as a highly sensitive probe of bond order. We found a variety of long-range bond order strengths for bulk-like films and for SLs of RNiO$_3$ with different rare-earth ions R. Additionally, we observed indications of fluctuating short-range bond order in LNO-LAO SLs. Secondly, we investigated the magnetic properties of the same samples and established that the spin spiral magnetism is a robust order, which develops in most RNiO$_3$ systems irrespective of the bond order strength. We also showed that the model for the magnetic excitations in bulk RNiO$_3$ provides an accurate description of the magnon dispersions in SLs with noncollinear magnetic order. On the other hand, we find an essentially flat dispersion with reduced magnon energies in the case of SLs with collinear magnetic order. This observation is explained by a spin-wave theory with the same interaction parameters adapted for the particular SL geometry. Our approach determines bond and magnetic order on a quantitative level, which is of great importance to understand the feedback between these two different ordering phenomena. According to recent theoretical work, this interplay is a key factor for the emergence of exotic phases like multiferroicity [118,119] or even potentially superconductivity [115,116] in RNiO$_3$.

In the future, it would be of great interest to study systems with a single active magnetic nickelate layer, in which the conventional noncollinear spin spiral cannot develop. The spin excitations measured by RIXS could give valuable insight to develop models for genuine two-dimensional magnetism in RNiO$_3$. In addition, RIXS and in particular spin excitations will help to understand the recently discovered superconductivity in an infinite-layer nickelate of composition Nd$_{0.8}$Sr$_{0.2}$NiO$_2$ [128]. Similarly to the cuprates, the possibility of spin-mediated superconductivy could be explored using RIXS.

Our approach to analyze the inter-orbital excitations with a double-cluster model could be used as a reference for studies of other high-

valence and highly covalent TMOs [232,233]. The accurate determination of bond order parameters by high-resolution site-selective RIXS is especially relevant for other materials with bond order such as manganites [234] and tellurides [235], which can be characterized in a similar way.

Chapter 4

Interplay of structure, bond and magnetic order in NdNiO$_3$ thin films

In Chapter 3 we have seen that heteroepitaxy is a powerful tool to control the macroscopic properties of TMOs harnessing the interplay between crystal structure and electronic correlations. Here, we further study the influence of epitaxial lattice mismatch on the stabilization of novel octahedral rotations and distortions, and their connection with the metal-to-insulator transition (MIT) as well as magnetic transition in rare-earth nickelates. The electronic and magnetic correlations in NdNiO$_3$ and other rare-earth nickelates are exceptionally sensitive to the modifications introduced by the substrate [77, 86, 105, 121], which can result in a complete suppression of the MIT for large compressive strains [123, 236]. On the other hand, we recall the study by Catalano *et al.* introduced in Fig. 1.6: tensile strain imposed to NdNiO$_3$ films through [101]-oriented NdGaO$_3$ substrates enhances T_{MIT} by more than 100 K [85]. This effect was attributed to the specific three-fold inter-

connectivity between the NiO$_6$-GaO$_6$ octahedral network of film and substrate across the (101) interface (*i.e.* each BO$_6$ unit shares three oxygen anion with the next one), together with close lattice matching between NdNiO$_3$ and NdGaO$_3$. These results stimulated further studies of films and superlattices on substrates with this unconventional orientation [117, 125, 237, 238], which led to important insights into magnetic ordering phenomena in thin and ultra-thin NdNiO$_3$ layers [100, 126, 239], further emphasizing the relevance of interfacial bonding of octahedral networks.

To gain a deeper understanding of new emerging phases and a possible alteration of electronic correlations in nickelate heterostructures, we have investigated the similarities and differences of NdNiO$_3$ thin films grown on [101]- and [011]-oriented NdGaO$_3$ substrates, respectively (Fig. 4.1). For both orientations, the interconnectivity of the octahedral network across the film-substrate interface is three-fold [77], and thus the epitaxial interplay between film and substrate is expected to be particularly pronounced. By utilizing electrical transport measurements and scanning transmission electron microscopy (STEM) as complementary techniques to probe different length scales, we find that the T_{MIT} can be controlled over a wide temperature range. The macroscopic properties of NdNiO$_3$ thin films can therefore be effectively modified by substrate orientation and film thickness, while our microscopy results indicate that in the vicinity of the substrate-film interface a phase is heteroepitaxially stabilized that has no bulk analog. Our experimental findings are corroborated by density functional theory (DFT) calculations suggesting that energetically disfavored phases can be accommodated by crystallographic stacking faults or a reorientation of the NdNiO$_3$ unit cells along the growth direction. Furthermore, our DFT calculations reveal an enhanced bond disproportionation in NdNiO$_3$, explaining the enhanced T_{MIT} in our films and those of Ref. [85]. In order to connect the lattice distortions and bond-disproportionated phase to the magnetic order observed in NdNiO$_3$ thin

Table 4.1: Overview of thin film samples and their properties. d_{NNO} represents the thickness of the $NdNiO_3$ layer.

d_{NNO} (Å)	Orientation	Remarks
110	(101) and (011)	grown by magnetron sputtering [85]
106	(101) and (011)	STEM study in Fig. 4.4
104	(101) and (011)	
70	(101) and (011)	STEM (REXS) study in Fig. 4.4 (4.7), noncollinear mangetic order
40	(101) and (011)	
14	(101)	STEM results in Fig. 4.3 and Ref. [126], collinear mangetic order

films, we used resonant elastic x-ray scattering (REXS). Similarly to the observations for T_{MIT}, we find that the magnetic transition temperature T_N largely depends on the layer thickness of the $NdNiO_3$ thin films and —albeit to a lesser extent— on the substrate facet. Our results suggest that bond order amplitudes above a critical value are a prerequisite for robust noncollinear magnetic order. For $NdNiO_3$ thin films with smaller bond order strength, we find a dramatically reduced transition temperature, and an altered spin structure in the ultra-thin limit. These close lying structural, magnetic and electronic energy scales facilitate the stabilization of novel phases through interface connectivity in heteroepitaxy. Our results provide insights into competing energy scales at microscopic length scales and give new perspectives for the epitaxial control of macroscopic phases in oxide heterostructures.

Parts of this Chapter are available as a manuscript by Y.E. Suyolcu* and K. Fürsich* *et al.*. The draft has been submitted for publication (June 2020) and can be found as item 10) in the List of Publications.

4.1 Sample and experimental details

Pulsed laser deposition (PLD) was used to grow $NdNiO_3$ thin films and superlattices (SLs) on $NdGaO_3$ (011) and (101) crystallographic
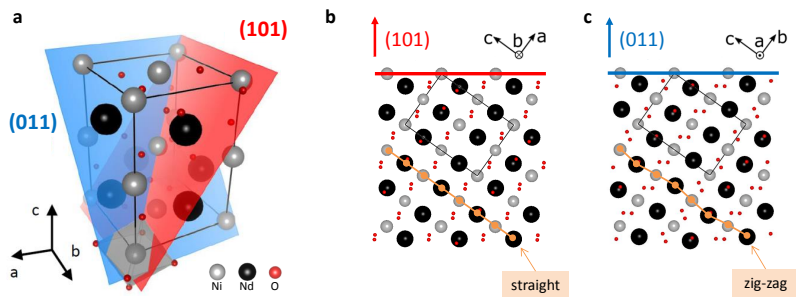
Figure 4.1: (a) Schematic of the orthorhombic NdNiO$_3$ unit cell, with the (101) and (011) crystallographic planes highlighted in red and blue, respectively. Additionally, one NiO$_6$ is shown in gray. Note that NdGaO$_3$ exhibits a similar unit cell (not shown here) with slightly different lattice parameters (see Section 4.1). (b), (c) Projections of the NdNiO$_3$ crystal structure along the [101] and [011] direction, respectively. The unit cell from panel (a) is indicated by black lines, and the (101) and (011) crystallographic planes by red and blue lines, respectively. The orange lines indicate characteristic *straight* and *zigzag* patterns of the Ni and Nd cation positions in the (101) and (011) projections, respectively. These patterns can be identified in STEM imaging.

Table 4.2: Overview of SL samples and their properties. d_{NNO} and d_{NGO} give the thicknesses of the NdNiO$_3$ and NdGaO$_3$ layers, respectively. Each NdNiO$_3$-NdGaO$_3$ bilayer is repeated four times. We indicated the presence and absence of an antiferromagnetic (AFM) Bragg peak in the column labeled "AFM observed". In the case of magnetic order we state the type of the microscopic spin structure. All SL samples are grown on (101) NdGaO$_3$ using PLD.

d_{NNO} (Å)	d_{NGO} (Å)	AFM observed	Spin order
26	12	yes	noncollinear
14	4.2	yes	collinear
14	12	yes	collinear
12	12	yes	collinear
10	12	yes	collinear
8	4.2	no	-
8	12	no	-
6	12	no	-

surfaces, respectively. We will use *Pbnm* notation throughout the whole chapter, see Fig. 4.1. The thicknesses of the NdNiO$_3$ samples were determined by x-ray diffraction (XRD) and x-ray reflectivity (XRR). The properties of all samples investigated are indicated in Tabs. 4.1 and 4.2. To facilitate the comparison of different substrate facets, NdNiO$_3$ was deposited simultaneously on a [011]- and [101]-oriented NdGaO$_3$ substrate for selected thicknesses, yielding pairs of films grown under the same conditions with nominally identical film thicknesses. Details about the growth procedure can be found in Ref. [87]. Both, bulk NdNiO$_3$ and NdGaO$_3$ exhibit the orthorhombic space group *Pbnm* at room-temperature, with lattice parameters $a = 5.387$ Å, $b = 5.383$ Å, $c = 7.610$ Å, and $a = 5.428$ Å, $b = 5.498$ Å, and $c = 7.708$ Å, respectively [218, 240]. Thus, the larger NdGaO$_3$ unit cell dimensions can impose tensile strain on an epitaxial NdNiO$_3$ unit cell. The [011] and [101] NdGaO$_3$ substrate orientations correspond to cuts perpendicular to the $[111]_{\mathrm{pc}}$ and $[\bar{1}11]_{\mathrm{pc}}$ body diagonal of the pseudocubic unit cell, respectively. Note that while in the simplified pseudocubic reference

frame all body diagonal directions are equivalent, the [011] and [101]
direction of the orthorhombic *Pbnm* unit cells of NdNiO$_3$ and NdGaO$_3$
are distinct. Projections of the crystal structure perpendicular to the
(011) and (101) plane are shown in Figs. 4.1 (b,c), with a characteristic
zig-zag line connecting the Ni-Nd cation positions in the former cut,
and a *straight line* in the latter. In the following, we will use these
distinct projections to identify the orientation of the substrate and the
film in the STEM high-angle annular dark-field (HAADF) images [Figs.
4.3 (a), 4.4].

The electron-transparent specimens were prepared by employing
mechanical grinding, tripod-wedge polishing and argon-ion milling steps,
respectively. Details can be found in Ref. [241] and item 10) in the List
of Publications.

Electrical resistance measurements were performed using a Physi-
cal Property Measurement System (PPMS) in van-der-Pauw geometry.
The data shown in Fig. 4.2 panel (a) and (b) were recorded upon slowly
cooling down the sample.

In order to determine the ground state of strained NdNiO$_3$ on [101]-
and [011]-oriented NdGaO$_3$, our colleagues Z. Zhong and P. Hansmann
carried out DFT calculations with the VASP (Vienna ab initio simu-
lation package) code [242, 243] using the generalized gradient approxi-
mation GGA-PBE functional [244]. For the fully relaxed NdGaO$_3$ unit
cell in *Pbnm* symmetry we obtained the lattice parameters $a = 5.334$ Å,
$b = 5.302$ Å, and $c = 7.569$ Å. We note here that DFT lattice param-
eter tend to overestimate atomic distances in solids, but their relative
changes is captured properly. In other words, the absolute lattice pa-
rameters of substrate and film may deviate substantially from the ex-
perimental values, but the calculations still correctly reflect the phase
behavior of strained NdNiO$_3$ films. For NdNiO$_3$ an onsite Hubbard U
of 2 eV was used and the in-plane lattice parameters were fixed to the
values of NdGaO$_3$, while the out-of-plane lattice parameter was varied
and internal atomic positions were relaxed. Note that for the [101] ori-

entation only the b-axis coincides with a main in-plane crystallographic direction, and for [011] orientation the a-axis. Hence, we define the second in-plane lattice parameter as $a^* = \sqrt{a^2 + c^2}$ and $b^* = \sqrt{b^2 + c^2}$, respectively. Consequently, a^* and b of [101]-oriented NdNiO$_3$ were fixed to the corresponding values calculated for NdGaO$_3$, and a and b^* were fixed for [011]-orientated NdNiO$_3$, while in both cases the out-of-plane lattice parameters c^* were varied to relax the internal atomic positions. The parameter c^* corresponds to the distance between consecutive Ni planes along the [101] and [011] direction, respectively.

To determine the magnetic order of the NdNiO$_3$ thin films and SLs, we performed complementary REXS experiments at the BESSY-II undulator beam line UE46-PGM1 at the Helmholtz-Zentrum Berlin. The energy of the x-rays was tuned to the Ni L_3 resonance at $\approx 853\,\text{eV}$, and we used π-polarized light to maximize sensitivity to the contributions from magnetic scattering [86].

4.2 Bond order amplitude and oxygen positions

The electrical transport properties of NdNiO$_3$ films grown on [011]- and [101]-oriented NdGaO$_3$ substrates are shown in Figs. 4.2 (a,b). All films thicker than 14.4 Å display a change of slope in resistivity with decreasing temperature, signaling a transition from metallic to insulating behavior. We determined the transition temperature T_{MIT} using the maximum value of $-\partial(\ln(\rho))/\partial T$, where ρ is the resistivity and T the temperature. We find the highest $T_{\text{MIT}} = 285\,\text{K}$ for the 106 Å thick NdNiO$_3$ film on (101) NdGaO$_3$, which is substantially higher than the T_{MIT} of 175 K of the corresponding film on (011) NdGaO$_3$, and the T_{MIT} of 150 K reported for films on (001) NdGaO$_3$ [217]. In more detail, Fig. 4.2 (c) displays the transition temperature T_{MIT} as a function of NdNiO$_3$ layer thickness d for both substrate orientations, with the
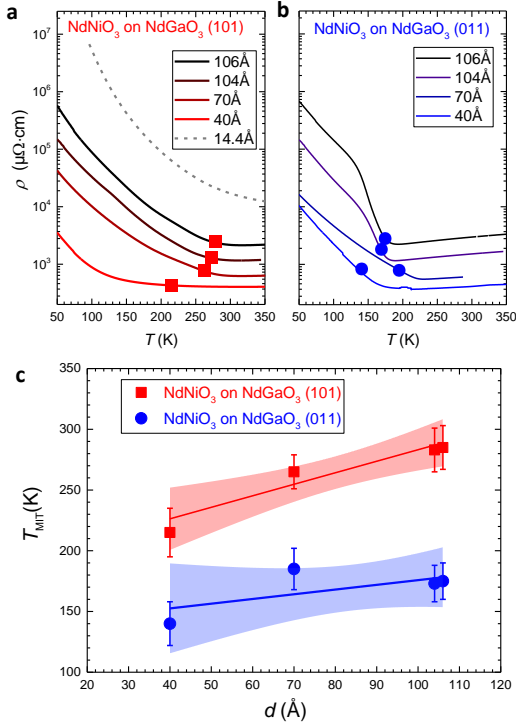
Figure 4.2: (a), (b) Electrical resistivity ρ as a function of temperature T measured for NdNiO$_3$ films of different thickness grown on [101]- and [011]-oriented NdGaO$_3$ substrates, respectively. The filled symbols indicate the transition temperature T_{MIT}. Note that the 14.4 Å film [gray dashed lines in panel (a)] is semiconducting without MIT. All curves except the one for the 14.4 Å film are offset in vertical direction by multiples of 250 μΩ·cm for clarity. (c) T_{MIT} as a function of NdNiO$_3$ film thickness d. The red and blue solid lines are least square fits to the (101) and (011) data points, respectively. The shaded areas give the 85 % confidence bands of the fits.
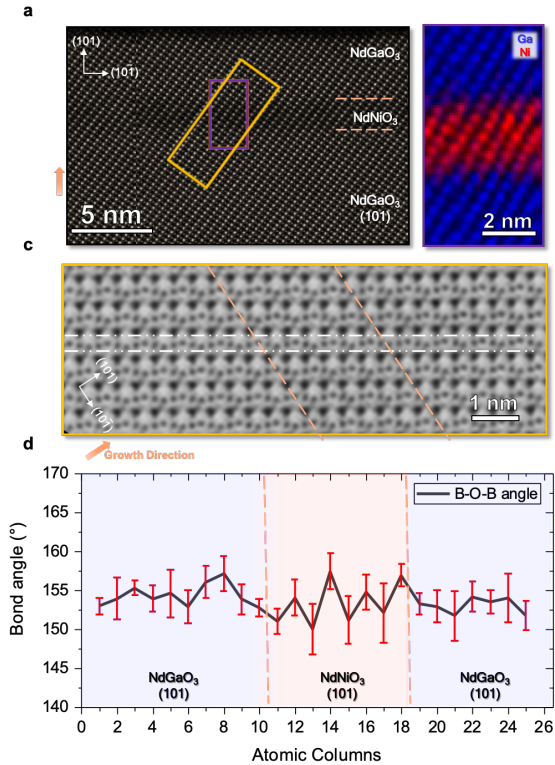
Figure 4.3: (a) STEM-HAADF image of the ultra-thin $14.4 \,\text{Å}$ $NdNiO_3$ film, including the $NdGaO_3$-$NdNiO_3$ substrate-film and the $NdNiO_3$-$NdGaO_3$ film-capping layer interfaces, indicated by dashed orange lines. (b) Atomic-resolution two-dimensional elemental maps of Ga (blue) and Ni (red). Interfacial intermixing occurs for one monolayer at most for both interfaces. (c) STEM-ABF image providing information about the oxygen positions. The atomic column within the white dashed-dotted lines corresponds to B-O-B bonds, with B = Ga, Ni. (d) Bond angle measurement across the $NdGaO_3$-$NdNiO_3$-$NdGaO_3$ structure, indicating that the B-O-B bond angle remains constant within the experimental error. Error bars indicate the 95% confidence interval. The blue and orange colored areas are guides for the eye indicating the $NdGaO_3$ and $NdNiO_3$ regions, respectively.

error bars given by the full width at half maximum of the peak in the derivative function $-\partial(\ln(\rho))/\partial T$. Notably, T_{MIT} increases with increasing thickness d for the films on both substrate orientations. This trend is particularly pronounced in the case of [101]-oriented substrates [shown in red in Fig. 4.2 (b)], and extrapolates to a T_{MIT} of 335 K reported for much thicker films in Ref. [85]. Moreover, a comparison of the (101) and (011) films of identical nominal thickness indicates that the [101] substrate orientation generally results in a higher T_{MIT}.

To gain insights on the thickness dependence of T_{MIT} and the absence of the MIT in ultra-thin films, we performed a STEM investigation of the thinnest 14.4 Å sample of our series. Note that this sample exhibits a second NdGaO$_3$-NdNiO$_3$ interface, that is, between the film and the NdGaO$_3$ capping layer, which possibly enhances interface-induced effects. As visualized in the STEM-HAADF image in Fig. 4.3 (a), the 14.4 Å film is of excellent crystalline quality with coherent interfaces and without traceable defects or stacking faults. Furthermore, atomic resolution STEM-EELS mapping of Ni and Ga [Fig. 4.3 (b)] suggests that elemental intermixing at the interfaces is limited to one monolayer at most. Detailed information about the local octahedral distortions at the NdGaO$_3$-NdNiO$_3$ interfaces can be obtained from high-resolution STEM-ABF imaging, which allows to track the oxygen atomic column positions [Fig. 4.3 (c)]. The analysis of the ABF image is shown in Fig. 4.3 (d), quantifying the bond angle between the B-site cation (Ga, Ni) and oxygen from the substrate region across the film and into the capping layer. Importantly, we find that across the interfaces the Ga-O-Ga and Ni-O-Ni bond angles remain constant within the experimental error, suggesting that the oxygen positions of the NdNiO$_3$ layer are forced to the oxygen positions given by NdGaO$_3$. In other words, this implies that the Ga-O-Ga bond angle of NdGaO$_3$ is transferred to the Ni-O-Ni angle in the epitaxial NdNiO$_3$ layer, which is consistent with the bond angle transfer scenario from NdGaO$_3$ substrates to NdNiO$_3$ films proposed in Ref. [85], and a pre-

viously performed less comprehensive ABF image analysis on the same 14.4 Å film [126]. For nickelate films thicker than 14.4 Å, however, the ABF analysis in Ref. [126] revealed a subsequent relaxation of the Ni-O-Ni bond angles up to bulk-like values, indicating that the strongly enhanced T_{MIT} of thicker $NdNiO_3$ films on [101]-oriented $NdGaO_3$ substrates is likely not caused by altered Ni-O-Ni bond angles, but caused by other effects that will be discussed later. The pinning of oxygen positions in the vicinity of the film-substrate interface obstructs the NiO_6 octahedral breathing-mode distortion and together with the modified Ni-O-Ni bond angle suppresses the MIT. As a result, in thicker films, a thin $NdNiO_3$ layer close to the interface of the $NdGaO_3$ substrate shows no bond disproportionation down to lowest temperatures [126], while layers further away from the interface gradually develop a breathing distortion, which sets the basis for the temperature-driven MIT. In this scenario, and within the range of film-thicknesses considered in Fig. 4.2, T_{MIT} naturally decreases as a function of reduced film thickness, with a crossover to a regime of ultra-thin films where the octahedral breathing mode is suppressed.

Next, we clarify the mechanisms that are responsible for the different T_{MIT} of $NdNiO_3$ films of nominally identical thickness grown on [011]- and [101]-oriented substrates, respectively. To this end, we performed STEM-HAADF imaging with atomic resolution on the two 70 Å-thick films. A representative HAADF image of each sample is shown in Fig. 4.4. In case of [101] substrate orientation, high epitaxial quality of the $NdNiO_3$ film is found [Fig. 4.4 (a)]. In particular, the Nd and Ga ions in the $NdGaO_3$ substrate are arranged in *straight lines*, as expected for the [101] orientation [see also Fig. 4.1 (b)]. A closely similar *straight line* pattern is adopted by the Nd and Ni ions in the $NdNiO_3$ film and persists up to the topmost layers, suggesting that the entire film grew in the same orientation as the substrate. By contrast, several regions with crystal defects can be observed in the film on [011]-oriented $NdGaO_3$ [Fig. 4.4 (b)], which was grown simultaneously

under identical conditions (see Section 4.1). While the first monolayers
of the film exhibit good crystalline quality, the defective regions start to
form further away from the NdNiO$_3$-NdGaO$_3$ interface. The majority
of defects in Fig. 4.4 (b) can be attributed to stacking faults of the per-
ovskite crystal lattice. However, a close inspection of the upper parts
of the defective regions reveals patches with rather *straight lines* of Nd
and Ni, while overall the Nd and Ni ions are mostly arranged in *zig-
zag lines* in congruence with the Nd and Ga ions of the [011]-oriented
substrate. Remarkably, this change of the Nd and Ni arrangement is
indicative of a reorientation of the NdNiO$_3$ unit cell with respect to the
growth direction, *i.e.* from [011] to [101] orientation.

The higher defect density and the presence of partially reoriented
regions in the films grown on (011) NdGaO$_3$ substrates are partic-
ularly interesting to study when aiming to understand basic mech-
anisms that lead to the formation of a particular crystalline phase.
This NdNiO$_3$-NdGaO$_3$ system seems to reflect the competing energy
scales between epitaxial octahedral connectivity and the formation of
the NdNiO$_3$ bond-disproportionated state. Hence, to shed light on
the possible presence of competing energy scales, we consider different
epitaxial combinations between the [011]- and [101]-oriented NdNiO$_3$
and NdGaO$_3$ unit cells in a strain minimization scenario, followed by
DFT+U calculations of the corresponding ground state energies.

4.3 Ground state and bond order strength from DFT+U calculations

In order to understand the observed differences in T_{MIT} of films grown
on the different NdGaO$_3$ facets, we first address the lattice mismatch
as origin of preferred film orientation. Determined by the choice of sub-
strate facet, NdNiO$_3$ experiences a slightly different lattice mismatch
depending on its own relative orientation. This is illustrated in the top
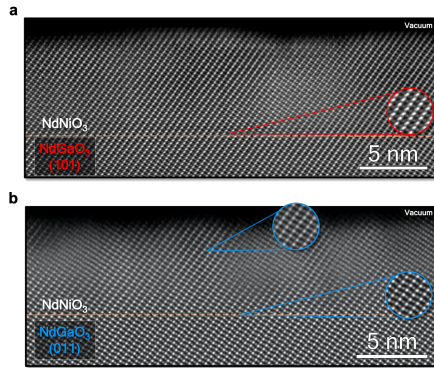
Figure 4.4: (a), (b) STEM-HAADF images of the 70 Å NdNiO$_3$ films on
[101]- and [011]-oriented NdGaO$_3$ substrates, respectively. The insets
illustrate the presence of characteristic *straight* and *zig-zag* patterns
of the Ni and Nd cation positions, which are indicative of the [101]
and [011] orientations, respectively. While the NdNiO$_3$ film on (101)
NdGaO$_3$ is entirely [101]-oriented and of high crystalline quality (a),
a more defective structure together with reoriented [101] patches is
observed for the film on (011) NdGaO$_3$ (b).
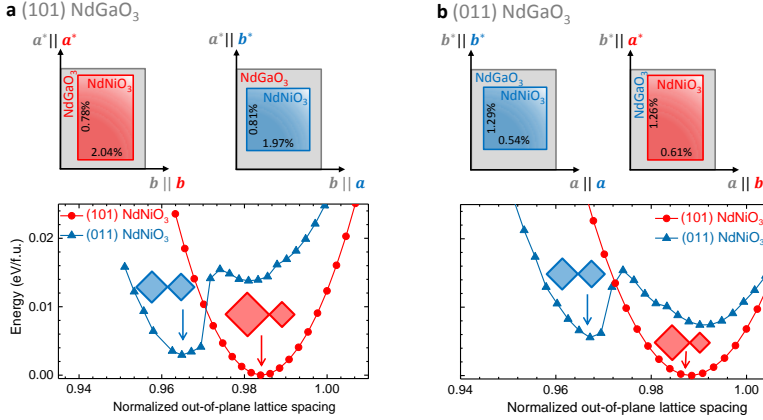
Figure 4.5: Top panels: Schematic projections of the dimensions of the bulk NdNiO$_3$ and NdGaO$_3$ unit cells for different film orientations on (a) (101) NdGaO$_3$ and (b) (011) NdGaO$_3$ substrates. The crystallographic in-plane directions (a^*, b^*, a, b) of NdNiO$_3$ and NdGaO$_3$ are indicated, together with the normalized, directional lattice mismatch $(l_{\mathrm{NdGaO_3}} - l_{\mathrm{NdNiO_3}})/l_{\mathrm{NdNiO_3}}$ in %. Bottom panels: Free energy on NdNiO$_3$ as a function of the normalized out-of-plane d lattice spacing as obtained from DFT+U calculations for the four different substrate-film orientation configurations depicted in the top panels. Keeping the in-plane lattice parameters fixed to those of [101]-oriented NdGaO$_3$ in (a) and [011]-oriented NdGaO$_3$ in (b), the ground state energies have been calculated for a range of values for the out-of-plane c^* spacing. Since the NdGaO$_3$ substrate induces tensile strain in all configurations, a reduced c^* spacing is expected with respect to the bulk (for the normalization we used the DFT+U values for NdNiO$_3$, that is $c^*_{(101)} = 4.360$ Å for the (101) phase and $c^*_{(011)} = 4.342$ Å for the (011) phase). Further, the DFT+U derived structures reveal an enhanced bond disproportionation in [101]- compared to [011]-oriented films on both substrate orientations, as illustrated by the insets.

part of Fig. 4.5 (a,b). For all possible combinations of film and sub-
strate orientation, the substrate induces tensile strain to the NdNiO$_3$
film. For the one-to-one configurations we find $\approx 0.8\%$ and $\approx 2.0\%$
in-plane lattice mismatch for (101)-(101) NdNiO$_3$-NdGaO$_3$ [Fig. 4.5
(a)] and $\approx 1.3\%$ and $\approx 0.5\%$ for (011)-(011) [Fig. 4.5 (b)]. The values
for the other two arguably counter-intuitive configurations of (011)-
(101) and (101)-(011), however, do not significantly differ. Thus strain
minimization alone cannot explain the experimentally observed partial
reorientation to (101) for films grown on (011) substrates [Fig. 4.4 (b)].

Next we address the relevance of electronic interactions (on the level
of DFT+U) by discussing the results obtained for the four configura-
tion illustrated in the top panels of Fig. 4.5 using a Hubbard U of 2 eV,
typical for rare-earth nickelates [83,134]. The bottom panels of Fig. 4.5
(a,b) show the ground state free energy of NdNiO$_3$ as a function of the
normalized out-of-plane lattice spacing $c^*_{(101)}/c^{*\mathrm{bulk}}_{(101)}$ and $c^*_{(101)}/c^{*\mathrm{bulk}}_{(101)}$,
respectively (bulk values were taken from the DFT+U calculation, see
Section 4.1), while the in-plane lattice constants have been fixed to
those of (011) and (101) NdGaO$_3$, respectively. On both substrate
facets the growth of [011]-oriented NdNiO$_3$ has an overall higher energy
and is therefore less favored [bottom panels in Fig. 4.5 (a,b)]. For [101]-
oriented NdNiO$_3$ we find a global minimum on both substrate facets for
reduced out-of-plane lattice spacings of about 98.5% of the substrate
c^* parameter in good agreement with out-of-plane lattice spacing de-
termined by resonant x-ray reflectivity [126]. Thus we conclude that
the combination of strain and electronic interactions captured in our
DFT+U calculations indicate a preference of [101] film orientation in-
dependent of the substrate facet. In addition our DFT+U calculations
reveal a second important result: The crystal structures corresponding
to the global energy minima differ significantly from bulk regarding
the size of the bond disproportionation. More specifically, in the bond-
disproportionated ground state of (101) NdNiO$_3$, the long (d_L) and
short (d_S) Ni-O bond lengths in the expanded and compressed NiO$_6$

octahedra are $d_L = 1.97\,\text{Å}$ and $d_S = 1.90\,\text{Å}$, respectively. Parametrization of the disproportionation δd as the difference in long and short bond lengths d_L and d_S from the mean value, yields $\delta d = 0.035\,\text{Å}$, which is significantly enhanced compared to a δd of $0.015\,\text{Å}$ calculated for a fully relaxed bulk NdNiO$_3$ unit cell[1]. Conversely, the distortion δd of the hypothetical, local minimum structures of (011) NdNiO$_3$, either on (101) or (011) NdGaO$_3$ is similar to that of bulk NdNiO$_3$[2]. Therefore, we conclude that the orientational structure stabilization is not driven by strain minimization alone, but by its combination with electronic interactions arising from the tendency of the nickel $3d^8\underline{L}^1$ configuration to favor a disproportion into two sites with $3d^8\underline{L}_{1+x}$ and $3d^8\underline{L}_{1-x}$. In other words, the system chooses the orientation with a particular tensile lattice mismatch that maximizes the bond disproportionation.

This explains our observations for thick films on [101]-orientated substrates, where we clearly observe the stabilization of [101] film orientation (STEM image in Fig. 4.4) and an enhancement of T_{MIT} compared to bulk. However our DFT+U calculations do not account for effects of interconnetivity in the vicinity of the film-substrate interface. Due to the necessity to form Ga-O-Ni bonds across the interface and the stability of the NdGaO$_3$ *Pbnm* structure (with only one Ga Wyckoff position $4a$) down to lowest temperature, this interfacial connectivity prevents the development of bond disproportionation close to the interface. In ultra-thin slabs on (101) NdGaO$_3$, the length scale on which this pinning of atomic positions by the substrate prevents bond disproportionation in NdNiO$_3$ has been estimated to lie around 8 atomic layers [126]. In the present study we find a related length scale in the [011] film growth, where within approximately the first 10 atomic layers

---

[1]The exact numeric value of δd depends on details of the calculation, such as the choice of U. However, we emphasize that the trend of an enhanced bond disproportionation for (101) NdNiO$_3$ is robust.

[2]Importantly, the crystal structures of (011) NdNiO$_3$ (all data points in Fig. 4.5, including the side-minima) do not exhibit enhanced bond disproportionation.

(≈ 20 Å) a defect-free [011]-orientation of the NdNiO$_3$ film is observed [Fig. 4.4 (b)]. Above this critical length scale, where the pinning effect of the substrate is relaxed, the above discussed combination of lattice mismatch and electronic correlations takes over and causes the partial reorientation to a (101) film alignment and defect formation as observed in the top part of the STEM image in Fig. 4.4 (b).

We conclude that closely similar energy scales of lattice and electronic degrees of freedom in rare-earth nickelates enable the heteroepitaxial stabilization of phases driven by enhanced electronic interactions. In particular, our study shows that the symmetry of the substrate as well as the choice of the crystal facet can have significant impact on the electronic properties of NdNiO$_3$, as demonstrated by the complex thickness and facet dependence of T_{MIT}. Up to thicknesses of 5-10 atomic layers, the structural pinning of the substrate dominates and determines the film orientation and results in a suppression of bond disproportionation in the NdNiO$_3$ slabs. Above this length scale, lattice mismatch in combination with electronic correlations determine the properties of the films. Our study therefore provides an extraordinarily high level of understanding and control of the bond-disproportionated phase in NdNiO$_3$.

4.4 Interplay of bond and magnetic order investigated by REXS

Having established a picture of the relevant energy scales for the bond-disproportionated phase in NdNiO$_3$ thin films, we proceed to study the unique magnetic order in these compounds. In particular, we focus on the implications of structural properties and modified bond order for the spin order in these compounds. As we have seen in Chapter 3, REXS is a valuable tool to study the microscopic AFM spin structure and the transition temperature of nickelate thin films, specifically in

the ultra-thin limit. In this Section, we take advantage of the investigation of SLs where the ultra-thin slabs are repeated consecutively (Tab. 4.2) to boost sensitivity to small modifications of the magnetic REXS signal provided by only a few monolayers.

We use x-rays resonantly tuned to the Ni L_3 edge to access the characteristic $(1/2, 0, 1/2)$[3] AFM Bragg peak of NdNiO$_3$. Dictated by the orthorhombicity of the NdGaO$_3$ substrate, two distinct domains exist in epitaxially grown NdNiO$_3$ resulting in magnetic Bragg peaks at $(1/2, 0, 1/2)$ and $(1/2, 0, \bar{1}/2)$ [245]. For an intuitive experimental scattering geometry we restrict ourselves here to the former and investigate the magnetic order along the [101] direction. Importantly, this implies different scattering geometries for the samples grown on (101) and (011) NdGaO$_3$. For NdNiO$_3$ on (101) NdGaO$_3$, the direction of the magnetic propagation vector coincides with the surface normal, *i.e.* the magnetic contribution is superimposed to the reflectivity in a specular scan. Consequently the magnetism for this facet can be studied in a straightforward fashion. For NdNiO$_3$ on (011) NdGaO$_3$, the direction of the magnetic propagation vector differs from the surface normal. Therefore we mounted the samples on a 70° wedge, which brings the [101] direction into the scattering plane. To extract the magnetic transition temperature T_N, we systematically increase the temperature of our samples (starting from $T = 10$ K) and define T_N as the temperature at which the AFM peak disappears [see Fig. 4.6 (b)]. In addition to T_N, we extract the relative magnetic moment directions at $T = 20$ K from the azimuthal dependence of the AFM peak following the protocol described in Section 4.1 and Ref. [86] [see Fig. 4.6 (a)].

Figure 4.6, panel (c) depicts the magnetic transition temperature T_N as a function of NdNiO$_3$ layer thickness and NdGaO$_3$ substrate orientation. For NdNiO$_3$ layer thicknesses $d > 60$ Å grown on [101]-oriented NdGaO$_3$, T_N is comparable to the bulk value of NdNiO$_3$

---

[3]The $(1/2, 0, 1/2)$ peak in orthorhombic *Pbnm* notation corresponds to the $(1/4, 1/4, 1/4)$ peak in a pseudocubic reference frame.
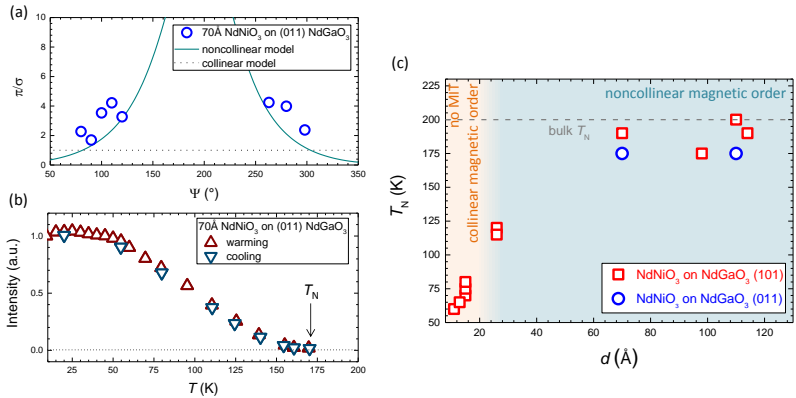
Figure 4.6: (a) and (b) Magnetic REXS characterization of a $70\,\text{Å}$ thick $NdNiO_3$ thin film on (011) $NdGaO_3$. (a) The azimuthal dependence of the $(1/2, 0, 1/2)$ magnetic peak signals noncollinear magnetic order. Note that we can only access a limited range of the azimuth angle Ψ due to limitations imposed by the $70°$ wedge. (b) Temperature dependence of the AFM Bragg peak for warming and cooling cycle. T_N was determined from the disappearance/onset of the characteristic AFM Bragg peak. (c) Magnetic transition temperature T_N as a function of $NdNiO_3$ layer thickness d for growth on [101]- (red squares) and [011]-oriented (blue circles) $NdGaO_3$, respectively. The gray dashed line gives T_N for bulk $NdNiO_3$ [122]. The orange shaded area indicates the transition into the ultra-thin limit of $NdNiO_3$ film thicknesses with absent MIT in accordance with Figs. 4.2 and 4.3. Note that for $d > 20\,\text{Å}$ we find noncollinear magnetic order (blue shaded area), which is also observed in bulk samples. For thicknesses between $10\,\text{Å} < d < 20\,\text{Å}$ the spin structure is characterized as collinear (up up down down) order. For $d < 10\,\text{Å}$, we did not detect an AFM Bragg peak indicative of period-four long-range magnetic order.

($T_N^{\text{bulk}} \approx 200$ K) [122]. This is already a striking result since we recall from the previous Section that the T_{MIT} in these samples is clearly enhanced, therefore T_N and T_{MIT} do not coincide as observed in bulk. For thicknesses smaller than ≈ 60 Å, we find that T_N is significantly reduced, similarly to the observations of a thickness dependent T_{MIT} [Fig. 4.2 (c)]. Specifically, for $d < 60$ Å the magnetic transition temperature T_N decreases as a function of d down to 55 K for the sample with $d = 10$ Å. For samples with even smaller NdNiO$_3$ slab thicknesses, we did not observe the characteristic AFM Bragg peak of NdNiO$_3$. Therefore we conclude that for $d < 10$ Å, the system does not host the typical period-four magnetic order found in NdNiO$_3$ samples with thicker magnetically active layers. The comparison of the NdNiO$_3$ samples on [101]- and [011]-oriented NdGaO$_3$ with nominally the same thicknesses reveals an enhanced T_N of about 20 K for the growth on (101) NdGaO$_3$. As far as the spin structure is concerned, we observe a crossover from noncollinear to collinear spin structure at $d \approx 20$ Å, in agreement with Ref. [126]. Interestingly, the absence of a MIT is closely linked to a collinear arrangement of spins, as illustrated in Fig. 4.6 (c).

We first discuss the difference in the magnetic ordering temperature T_N for NdNiO$_3$ grown on [101]- and [011]-oriented NdGaO$_3$. For the comparison we use the sibling samples with thicknesses of 110 Å and 70 Å and therefore limit ourselves to film thicknesses $d > 60$ Å . The (101) NdNiO$_3$ films show an enhanced T_N of about 20 K compared to the (011) ones. We recall that in comparison, T_{MIT} in (101) NdNiO$_3$ is enlarged by more than 50 K compared to (011) NdNiO$_3$. In first approximation, one can glean from the bulk phase diagram of RNiO$_3$ for R=Nd and Pr (*c.f.* Fig.1.3), that a higher T_N is expected for larger values of T_{MIT}, as the MIT (and the concomitant evolution of bond order) possibly constitutes the prerequisite for the magnetic order [8–10]. However, we emphasize that T_N for our thin films is similar to the magnetic ordering temperature of bulk NdNiO$_3$. In particular, the dramatically increased T_{MIT} for (101) NdNiO$_3$ compared to bulk is not

reflected in the magnetic ordering temperature and the separation of T_N and T_{MIT} is rather reminiscent of $SmNiO_3$. Therefore, we conclude that the magnetic order in thicker $NdNiO_3$ shows a different dependence on structural modifications such as octahdral tilts and rotations than the MIT. In addition, the lattice constraints and correlation effects resulting in an enhanced bond disproportionation δd in the (101) $NdNiO_3$ are not directly reflected in an enhanced magnetic ordering temperature. The noncollinear magnetic order seems to be a robust order, which sets in independent of the specific value and modifications of the bond disproportionation δd, in agreement with the RIXS study presented in Chapter 3.

Next we focus on the thickness dependence of T_N, which we have investigated for (101) $NdNiO_3$. In contrast to the linear dependence observed for T_{MIT} vs. d, T_N follows d in an order parameter like fashion. In particular, we identify the three regions mentioned before: absence of $(1/2, 0, 1/2)$ magnetic order ($d < 10\,\text{Å}$), monotonic increase of T_N for larger d ($10\,\text{Å} < d < 60\,\text{Å}$) with a crossover from collinear to noncollinear spin structure at $d \approx 20\,\text{Å}$, and a d independent T_N, where the value of T_N and the noncollinear spin order are comparable to the $NdNiO_3$ bulk ($d > 60\,\text{Å}$). This indicates once more that bulk-like magnetism in our films develops for films thicker than a critical number of layers, or equivalently for films exceeding a critical bond disproportionation δd larger than a certain value. The $NdNiO_3$ films with $d > 60\,\text{Å}$ show bulk like magnetic order in terms of spin arrangement and ordering temperature. While T_{MIT} is strongly affected by a modulated bond order amplitude, the magnetic order in $NdNiO_3$ seems to be robust and independent of δd, as long as a critical δd is realized. For $d < 60\,\text{Å}$, δd is reduced below the critical value, as T_N sensitively depends on the layer thickness. The further decrease of δd leads to a crossover to a collinear spin structure, while the magnetic Bragg peak remains at the same $(1/2, 0, 1/2)$ value, even in absence of a MIT [126,239]. Similarly to the energy scales established in the previous Sections, this intermediate

thickness regime is governed by a complex interplay of interface effects and the bulk ground state, while interface effects, such as the pinning of oxygen positions, ultimately dominate for thinner films. Interestingly, the previously observed length scale for the epitaxial stabilization of novel phases (about $\approx 20\,\text{Å}$, derived from STEM and transport investigations) is in excellent agreement with the film thicknesses of the crossover regime found in the REXS study. Finally for the thinnest films with $d \leq 10\,\text{Å} = 4\,\text{ML}$, the characteristic AFM order of RNiO$_3$ is absent. As illustrated in Fig. 4.1 (b), samples with $d \leq 4\,\text{ML} \approx 10\,\text{Å}$ are too thin to host the orthorhombic unit cell and therefore the period-four AFM order cannot develop.

We therefore conclude that the magnetic order and in particular the transition temperature T_N shows a different but equally sensitive dependence on film thickness and substrate faced compared to the MIT. Our findings imply that heteroepitaxially induced modifications of the bond disproportionation cause the change from noncollinear to collinear spin order, but a finite bond order seems not to be the prerequisite for the occurrence of period-four magnetic order. However, when the thickness of the magnetic layer is one magnetic period or less, the period-four order cannot develop anymore. Either long range magnetic order is completely suppressed or develops at a different ordering vector. Future experiments will differentiate between these scenarios. Finally, we point out, that the comparable length scales for the stabilization of novel electronic, magnetic, and structural phases establish a hitherto elusive understanding to control the properties of TMOs using heteroepitaxy.

In the last part of this Section, we aim to quantify the reoriented regions of (101) NdNiO$_3$ from the thin film grown on [011]-oriented NdGaO$_3$. As this information remains elusive from the STEM investigation in Fig. 4.4, we exploit the high sensitivity of REXS to detect signals of magnetically active layers down to 1 u.c. and less [86, 191]. Therefore REXS provides the necessary sensitivity to trace even small
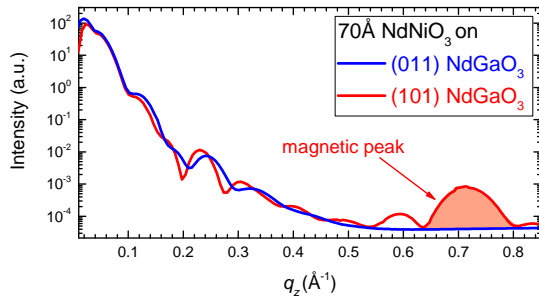
Figure 4.7: REXS from $70\,\text{Å}$ thick $NdNiO_3$ films on [101]- and [011]-oriented $NdGaO_3$ substrates. The data were taken at $T = 20\,\text{K}$ using π-polarized x-rays tuned to the Ni L_3 edge. For the (101) $NdNiO_3$ film, the AFM Bragg peak appears as expected in reflectivity, *i.e.* in a scattering conditions where the magnetic propagation vector and the surface normal coincide with the [101] direction. We indicate the magnetic contribution to the reflectivity with a red shaded area. Contrary, for the film grown on (011) $NdGaO_3$, we do not observe a magnetic peak in specular conditions, which would be indicative of large reoriented regions of $NdNiO_3$ with [101] orientations. Therefore the $NdNiO_3$ film on [011]-oriented $NdGaO_3$ mostly comprises [011]-oriented $NdNiO_3$, despite the presence of defective and reoriented regions suggested by the STEM investigation.

portions of reoriented (101) NdNiO$_3$. Fig. 4.7 shows specular scans
(at the Ni L_3 edge and $T = 20$ K) of the 70 Å thick NdNiO$_3$ films. In
this specular scattering condition, the size of the momentum transfer
along the surface normal is varied, while its direction remains constant,
i.e. parallel to the surface normal. Therefore, we detect magnetic con-
tributions to the refelctivity only if the magnetic propagation vector
is parallel to the surface normal. As discussed in the introduction of
this Section, the magnetic ordering vector of NdNiO$_3$ is along [101]
(in addition to [10$\bar{1}$], which will be discarded here due to experimental
reasons), and consequently, we can use the direction of the magnetic
ordering vector as an indicator of the thin film orientation. For NdNiO$_3$
on (101) NdGaO$_3$ we observe a magnetic contribution to the refelctiv-
ity, indicating the expected (101) NdNiO$_3$ phase. The magnetic peak
(red shaded area in Fig. 4.7) at $q_z \approx 0.7$ Å^{-1} can be unambiguously
assigned to the period-four magnetic order of bulk NdNiO$_3$. In the
film on (011) NdGaO$_3$, we would expect a similar magnetic contribu-
tion in case of substantial reorientation to (101) NdNiO$_3$. However, for
NdNiO$_3$ grown on (011) NdGaO$_3$, we do no find indications of a mag-
netic signal at $q_z \approx 0.7$ Å^{-1} (see blue curve in Fig. 4.7), which would
suggest that large parts of the samples host [101]-oriented NdGaO$_3$[4].
Our REXS study therefore suggests that most of the NdNiO$_3$ thin film
grown on (011) NdGaO$_3$ comprises [011]-orientation.

Consequently, we emphasize that — in spite of the presence of rel-
atively large defective and reoriented regions seen by STEM — the
film on [011]-oriented NdGaO$_3$ mostly comprises [011]-oriented NdNiO$_3$
[Figs. 4.4 (b) and 4.7]. This suggests that PLD growth kinetics and
heteroepitaxy mostly overcome the energy barrier between the (011)
and (101) phase of NdNiO$_3$, facilitating the stabilization of the less fa-
vored (011) phase, in particular in proximity to the NdNiO$_3$-NdGaO$_3$

---

[4]We confirmed the conventional period-four noncollinear magnetic in the (011)
NdNiO$_3$ thin film. The corresponding AFM Bragg peak along [101] can be accessed
in a different scattering geometry, as discussed in the beginning of this Section, Fig.
4.6 (a) and (b).

interface [Fig. 4.4 (b)]. The macroscopic electrical transport and the magnetic properties of the films on (011) NdGaO$_3$ shown in Fig. 4.2 are therefore dominated by the (011) majority phase of NdNiO$_3$, which explains the observed difference in T_{MIT} of films grown on (101) and (011) NdGaO$_3$ substrates.

4.5 Conclusions and outlook

In summary, we investigated in detail the heteroepitaxial modifications in NdNiO$_3$ thin films by combining STEM, electrical transport measurements, REXS and DFT+U calculations. We identified a complex interplay between heteroepitaxial lattice constraints and electronic correlations, which manifests itself in a intricate dependence of the MIT and AFM transition temperature with film thickness and substrate orientation. Finally, we established a picture of competing energy scales that facilitate the stabilization of phases with no bulk analogue by means of facet and thickness control in heterostructures. The modified bond disproportionation has important implications for the magnetic ground state, which can be qualitatively different from the bulk RNiO$_3$ series [126], and for the exchange interactions. The enhanced bond disproportionation might result in a larger double exchange contribution, thereby modifying the exchange coupling constants stabilizing the magnetic order in RNiO$_3$. This scenario can be tested using RIXS experiments similar to the ones presented in Chapter 3 [100, 239].

The controlled creation of phases opens a new route to tune material properties in heterostructures for future applications in functional devices. Engineering of structural distortions and electronic correlations could potentially be used to stabilize exotic phases in RNiO$_3$ such as multiferroicity [118, 119] and superconductivity [115, 116, 128] in a technological relevant parameter range. This could possibly be done by using other orthorhombic substrates to systematically change the nature and the size of the strain.

Chapter 5

Raman scattering from current-stabilized nonequilibrium phases in Ca$_2$RuO$_4$

In the previous Chapters we discussed how the properties of quantum materials comprising $3d$ TM ions can be tuned using heterostructuring, that is epitaxial strain and spatial confinement. While this approach offers undoubtedly intriguing and useful perspectives, it does not offer a dynamic control of TMOs that can be turned on/off or modified in a continuous way. Therefore, it limits the endeavor to integrate TMOs as active elements of *in-operando* systems, which rely on fast switching between different states or electronic responses. To move further towards potential applications of quantum materials, we expand our study to *in-situ* control of TMOs using electrical current. Therefore, we investigate TMOs with $4d$ ions, which adds another flavor —spin-orbit coupling (SOC)— to the complex physics of correlated oxides.

Recall therefore the discussion in Chapter 2, where we identified SOC
as a key parameter to entangle the electron spin and shape of the elec-
tron orbital.   Due to the SOC-enhanced inter-connectivity of lattice
and electronic degrees of freedom, $4d$ electron systems offer one of the
richest playground among all TMOs.

In particular, we used Raman light scattering to study the current-
stabilized nonequilibrium semimetallic and metallic phases in Ca_2RuO_4,
which we have introduced in Chapter 1.4.2. By determining the local
temperature through careful analysis of the Stokes and anti-Stokes in-
tensities, we find that Joule heating can be completely avoided by sup-
plying sufficient cooling power in a helium-flow cryostat, and that the
semimetallic state is a genuine effect of the applied electrical current.
We further investigate the current-induced semimetallic state as a func-
tion of temperature and current. We confirm the absence of long-range
antiferromagnetic order and identify a substantial Fano broadening of
several phonons, which suggests coupling to a continuum of charge and
orbital fluctuations. Our results demonstrate that the current-induced
phases have characteristics distinct from the equilibrium ones.

This Chapter has been published to a large extent in K. Fürsich et
$al.$, Phys Rev. B **100**, 081101(R) (2019), which is item 7) in the List
of Publications.

5.1   Experimental Details

High-quality Ca_2RuO_4 single crystals with $T_N = 110\,K$ were grown
by the floating zone method as previously described [50, 246].   The
Ca_2RuO_4 crystals with dimensions $2.6 \times 1.0 \times 0.6\,mm^3$ were mounted
on the sample holder of a He flow type cryostat using GE varnish.
We used silver epoxy to contact the samples in a two-probe circuit
and a Keithley 2400 Source Measure Unit for sampling and control.
The transport experiments were carried out in the voltage-controlled
mode. The Raman measurements were performed with the Jobin-Yvon

LabRam HR800 single-grating Raman spectrometer in-house at MPI Stuttgart using the 632.8 nm excitation line of a HeNe laser. Details of the sample mounting and the Raman set-up are given in Section 2.2.3.

All spectra were taken in backscattering geometry along the crystallographic c axis, while the current was applied in-plane along the crystallographic (110) direction. As Ca_2RuO_4 crystallizes in the orthorhombic $Pbca - D_{2h}^{15}$ space group, excitations in the B_{1g} and A_g representations of the point group D_{2h} were probed in crossed and parallel configurations, corresponding to $z(XY)\bar{z}$ and $z(XX)\bar{z}$ geometries in Porto's notation, respectively. The polarization of the incident light was thus always kept at $45°$ with respect to the Ru-O-Ru in-plane bonds [see inset in Fig. 5.1 (b) and (d) for the scattering geometry]. Some spectra (Fig. 5.7) were corrected for the Bose thermal factor to obtain the Raman response $\chi''(\omega)$. Our spectra measured in the absence of current flow are in agreement with the ones reported in literature [59, 203].

5.2 High-current regime — The L^*-phase

In the first part of this Chapter, we focus on the current-induced metal-insulator transition (MIT) at and near room temperature, where the metallic phase sets in at currents of about 100 mA (*i.e.* in the high-current regime). In particular, we choose two configurations to evaluate the role of Joule heating. First we stabilize the temperature at $T = 250$ K and provide sufficient cooling power to avoid the Joule heating effects discussed below (Fig. 5.1). In a second set of experiments, we do not provide any cooling power to the sample and we leave it at room temperature, $T = 295$ K, before applying the electrical current (Fig. 5.2). As the voltage across the sample is increased, we observe a nonlinear increase in currents for both experimental conditions [Figs. 5.1 (a) and 5.2 (a)]. Raman spectra were measured at different points in the transport curve and show distinct changes for lower resis-
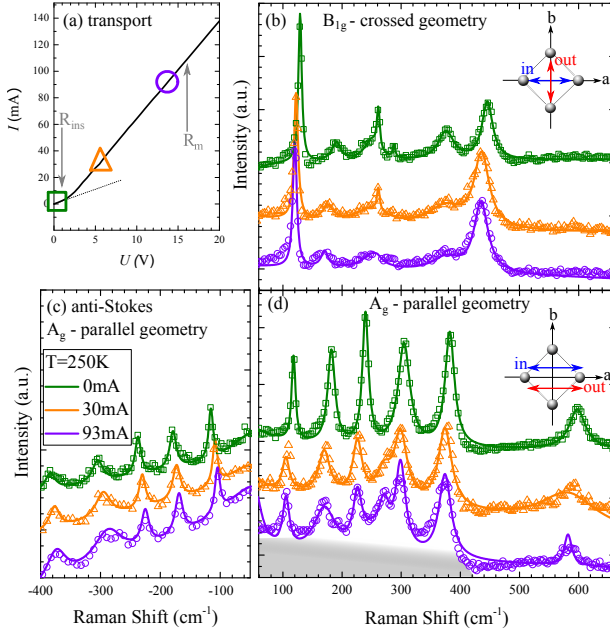
Figure 5.1: Current-induced MIT in Ca_2RuO_4. (a) Transport measurement. R_{ins} (R_m) indicates regions with high (low) resistance, which corresponds to the insulating (metallic) phase. The dotted line is an extrapolation of current values for the R_{ins} region. (b) Raman spectra in B_{1g} geometry (Stokes parts of the spectrum). (c) and (d) Raman spectra in A_g geometry for anti-Stokes and Stokes parts of the spectrum, respectively. The symbols in panel (b),(c) and (d) represent experimental Raman data, taken at the current values indicated with the corresponding marker in panel (a). The lines in panels (b),(c) and (d) are fits to experimental data. The inset in panels (b) and (d) illustrate the scattering geometry of the Raman experiment with respect to the Ru lattice (dotted lines: Ru-O-Ru bonds; a, b: crystallographic axes). The shaded area in panel (d) illustrates the increased electronic response, as discussed in the text.
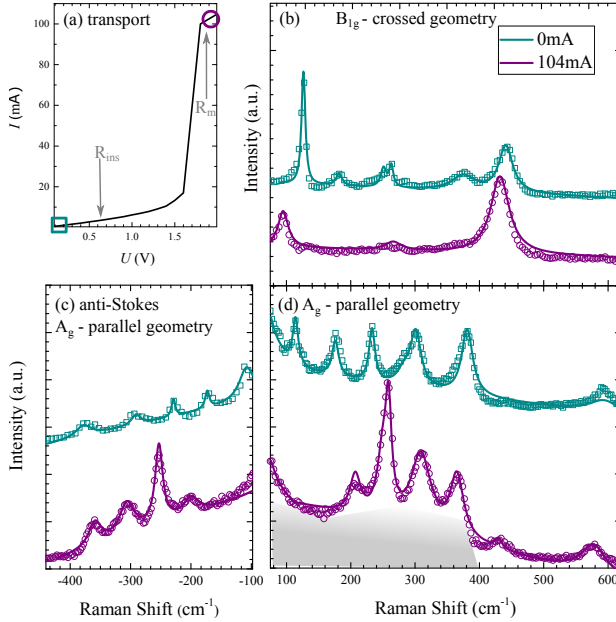
Figure 5.2: Measurements at room temperature without cooling. We observe a temperature-driven MIT in Ca_2RuO_4, instead of a current-induced MIT (c.f. Fig. 5.1). (a) Transport measurement. (b) Raman spectra in B_{1g} geometry (Stokes part of the spectrum). (c) and (d) Raman spectra in A_g geometry for anti-Stokes and Stokes parts of the spectrum, respectively. Temperatures are given in Tab. 5.1. In analogy to Fig. 5.1, the current values for the Raman spectra (experimental data: symbols; fit: lines) are indicated with the corresponding symbol in panel (a). In panel (d) the shaded area illustrates the increased electronic response.
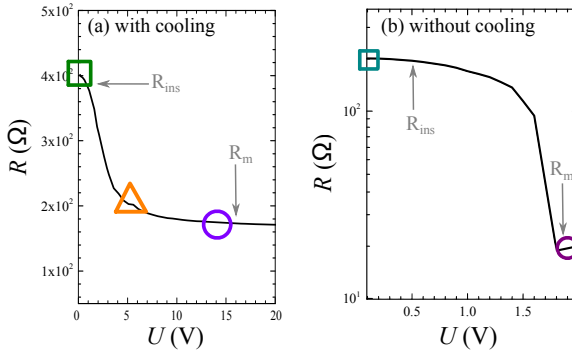
Figure 5.3: R(V) curves (a) with cooling and (b) without cooling. The arrows illustrate two regions with different resistance, $i.e.$ insulating (R_{ins}) and metallic (R_m) state.

tance values due to the appearance of the metallic phase [see Figs. 5.1 and 5.2]. Particularly, the increased electronic response towards lower wavenumbers [shaded gray area in Figs. 5.1 (d) and 5.2 (d)] indicates the transition into the metallic state [190, 247].

For a more comprehensive overview of transport data, we give $R(V)$ curves in addition to the $I(V)$ data [Figs. 5.1 (a) and 5.2 (a)]. Both panels of Fig. 5.3 show two different regimes with higher resistance R_{ins} and lower one R_m, corresponding to insulating and metallic regimes, thereby confirming the metal-to-insulatorl transition (MIT) [159]. We point out that our data was taken in the voltage-controlled mode, which is why we use $U(V)$ as the horizontal axes of the transport plots.

5.2.1   Stokes/anti-Stokes analysis

We first focus on the careful evaluation of the temperature in the current-induced metallic state by comparing Stokes and anti-Stokes intensities [173, 174, 248], which correspond to creation and annihilation of an elementary excitation and therefore have a positive or negative Raman shift, respectively. The ratio of the Raman scattered photons

of both processes has been derived in equation 2.20 and can be written as [173, 174]

$$\frac{I_{\mathrm{AS}}}{I_{\mathrm{S}}} = \frac{(\nu_{\mathrm{L}} + \nu_{\mathrm{p}})^3}{(\nu_{\mathrm{L}} - \nu_{\mathrm{p}})^3} \exp(\frac{-h\nu_{\mathrm{p}}}{k_{\mathrm{B}}T}) \tag{5.1}$$

with the frequencies of the phonon mode ν_{p} and of the laser ν_{L}, the Planck constant h and the Boltzmann constant k_{B}. Based on this relation, one can determine the *in-situ* temperature T at the laser spot. This accounts for possible effects of laser heating[1] and, in the present work, of current-induced Joule heating.

We demonstrate the Stokes/anti-Stokes analysis for the 93 mA data at 250 K following equation 5.1. The spectrum is fitted by a superposition of Voigt profiles with an additional linear background (see Fig. 5.4). This procedure is standard in the analysis of Raman spectra as the Voigt profile accounts for both experimental resolution and intrinsic lifetime broadening [249, 250], as introduced in Section 2.3.1. To evaluate the temperature following equation 5.1, we need to compare the intensities of Stokes and anti-Stokes profiles for a specific phonon [173, 174]. This is illustrated in Fig. 5.4, where the corresponding Stokes and anti-Stokes phonons are marked with the same color. The temperatures given in Tab. 5.1 correspond to the average of the temperatures determined for all visible phonon frequencies ν_{p} of one spectrum.

Our analysis shows that with active cooling (Fig. 5.1) the temperature of the sample remains constant. Therefore, the current-induced MIT is a true effect of the electrical current, while heating can be neglected (left part of Tab. 5.1). Remarkably, the measurements at room temperature without cooling (Fig. 5.2) reveal a significant Joule heating (right part of Tab. 5.1) to a temperature $T > T_{\mathrm{MIT}}$. Without external cooling power the Stokes/anti-Stokes analysis shows that the MIT is not induced by electrical current but rather by Joule heating

---

[1]We kept our laser power well below 1 mW to avoid laser heating.
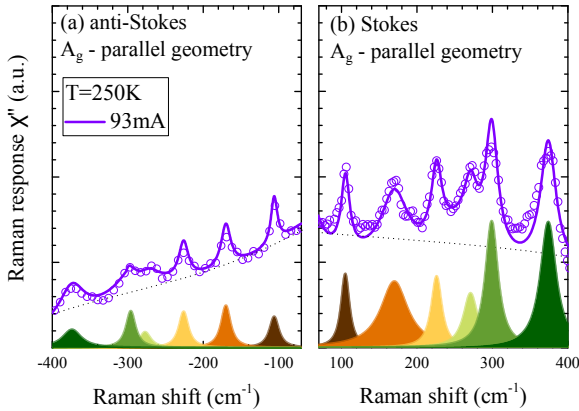
Figure 5.4: Raman spectra in the parallel A_g channel for (a) anti-Stokes and (b) Stokes regions, respectively. Each experimental spectrum is fitted by a superposition of several Voigt profiles and a linear background. The Voigt peaks are shown at the bottom. The dotted line shows the linear background. Corresponding phonons of the Stokes and anti-Stokes sides of the spectra are marked with the same color.

[2]. As a consequence, in order to observe the nonequilibrium metallic L^*-phase one must provide sufficient cooling power.

---

[2]The Raman spectra in fact are also closely similar to those collected in the equilibrium L-phase rather than to those from the current-induced L^* phase shown in Fig. 5.6.

Table 5.1: Temperatures with (left side) and without (right side) cooling, as determined from equation 5.1.

With cooling			Without cooling		
I / mA	T / K	phase	I / mA	T / K	phase
0	249 ± 4	S	0	295 ± 4	S
30	249 ± 5	transition			
93	252 ± 5	L^*	104	390 ± 5	L
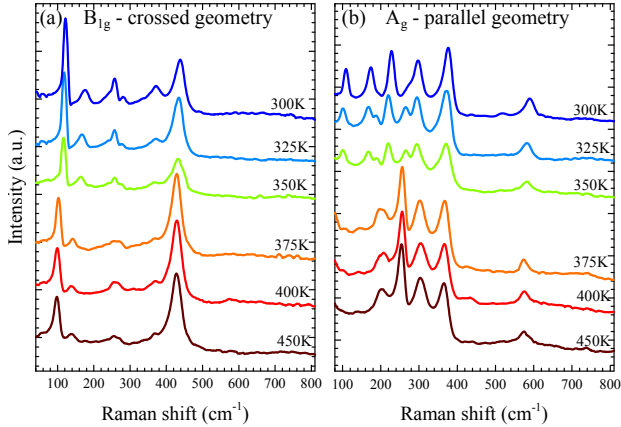
Figure 5.5: Temperature-induced MIT in Ca_2RuO_4. (a) and (b) Temperature-dependent Raman spectra in B_{1g} and A_g geometry, respectively.

5.2.2 Temperature-driven vs. current-driven MIT — L vs. L^*-phase

Having answered the fundamental question about the presence and role of heating effects, we now turn to the comparison of nonequilibrium (L^*) and equilibrium (L) metallic phases. We have therefore additionally investigated the temperature-induced MIT in Ca_2RuO_4 to obtain spectra for the equilibrium S- and L-phases [59, 203, 251, 252] in Fig. 5.5. The Raman experiments were performed on the very same crystal mounted in a Linkam cryostat to facilitate measurements up to 450 K. Note that for the specific set-up used here, we estimate an error in sample temperature of ± 10 K.

Fig. 5.6 compares the current-induced nonequilibrium L^*-phase to the metallic equilibrium L-phase obtained by increasing the temperature to $T = 400$ K, well beyond $T_{MIT} = 357$ K. The spectra of the L- and L^*- phase are similar (Fig. 5.6), and both are clearly distinct from the ones of the S-phase [Figs. 5.1 and 5.2 (b),(d) for 0 mA]. It is worth

mentioning that the Raman spectra of the L^*- phase resemble those of
metallic Sr_2RuO_4 measured at $T = 300\,K$ [253]. However as observed
in Fig. 5.6 (and in agreement with the neutron scattering study of
Ref. [168], where the sample was mounted in the same way), we note
that L- and L^*- phases are not identical. Differences in the number
and positions of the phonon modes are particularly apparent in the A_g
channel [Fig. 5.6 (b)]. This could be attributed to differences in the
crystal structure of the two phases, which were inferred from structural
refinements of neutron diffraction measurements for both nonequilib-
rium and equilibrium metallic states [162, 168]. The L^*-phase shows a
larger orthorhombicity (defined as the difference between the in-plane
lattice parameters a and b) and a smaller out-of-plane lattice param-
eter c in comparison to the L-phase. Both features suggest that the
L-phase is less distorted than the L^*-phase and hence, the Raman
spectra for these states reflect this difference. In light of recent re-
sults [166], another possibility to explain the differences between L-
and L^*-phases revolves around the heterogeneous development of the
current-stabilized state. In this scenario, the nonequilibrium metal-
lic phase does not pervade the bulk of the sample in a uniform way,
thereby resulting in defects, phase-boundaries and phase-slips. Due
to phonon-band folding induced by periodic domain boundaries, addi-
tional phonon modes might appear in the Raman spectrum. Future
spatially-resolved experiments might be able to discriminate between
these possibilities.

5.3   Low-current regime — The S^*-phase

We now turn to the discussion of the low-current regime which is char-
acterized by currents smaller than $1\,mA$ and is distinct from the high-
current states discussed until now. As mentioned before, the low cur-
rents lead to the formation of the so-called S^*-phase. We compare
the nonequilibrium S^*-phase to the equilibrium S-phase at $T = 10\,K$.
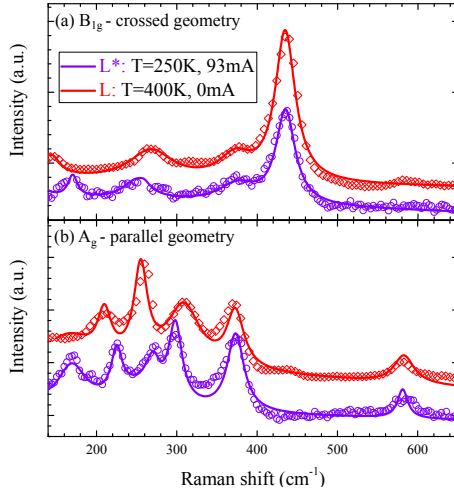
Figure 5.6: Raman scattering from metallic phases in Ca_2RuO_4. (a), (b) Raman spectra in B_{1g} and A_g geometry, respectively. Symbols (Lines) represent experimental (fitted) data.

The Raman spectra for crossed and parallel configurations are shown in Fig. 5.7. The feature at $101\,cm^{-1}$ in B_{1g} geometry was previously identified as single-magnon excitation [59] inherent to the soft-moment magnetic state in Ca_2RuO_4. In the current-stabilized phase the magnon peak is absent, thereby suggesting that long-range AFM order is suppressed. This observation confirms earlier bulk magnetometry measurements [167], and neutron studies [168] which did not identify magnetic Bragg reflections characteristic of AFM ordering in the S^*-phase.

The phonon energies are nearly identical in the S- and S^*-phases (apart from some minor softening in the S^* phase), which is consistent with the nearly identical Ru-O bond lengths identified by neutron diffraction [168]. In contrast to the symmetric phonon lineshapes in the S-phase, several of the phonons in the S^*-phase exhibit markedly asymmetric lineshapes. Phonon asymmetries are known to result from interactions with a continuum. The phonon asymmetry can be ob-
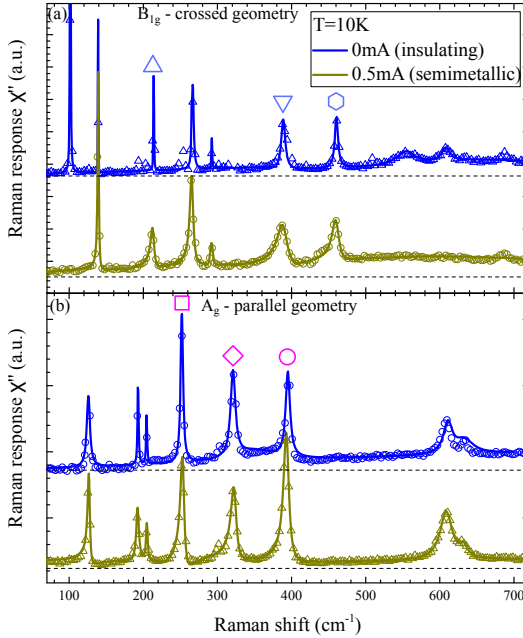
Figure 5.7: Current-stabilized semimetallic phase in comparison to the equilibrium AFM insulating phase. Raman spectra in (a) crossed B_{1g} geometry and (b) A_g geometry. The lines are superpositions of Fano peaks fitted to the data (small symbols). The phonon modes marked with large symbols are analyzed in Fig. 5.8.
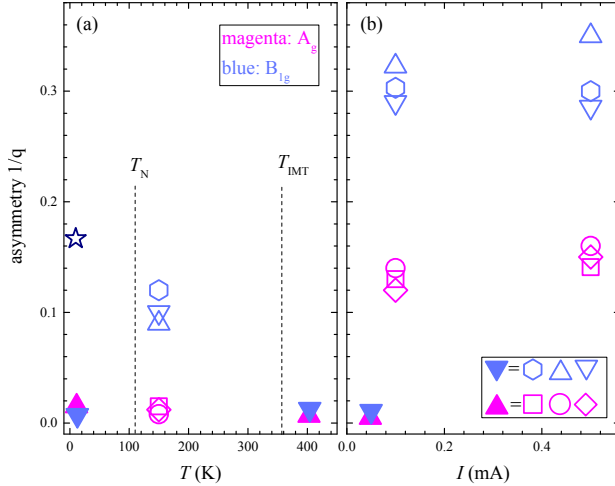
Figure 5.8: Asymmetry parameter $1/q$ for (a) equilibrium and (b) nonequilibrium phases of Ca_2RuO_4. Data for panel (b) were taken at $T = 10\,\mathrm{K}$. Magenta (blue) symbols correspond to $1/q$ values for parallel (crossed) polarization. For the B_{1g} geometry, we analyze the phonons at 211, 388 and $458\,\mathrm{cm}^{-1}$ and for the A_g channel at 252, 321 and $392\,\mathrm{cm}^{-1}$, as indicated in Fig. 5.7 with the corresponding open symbol. Filled symbols summarize all phonons for a specific geometry. The increased asymmetry in the insulating paramagnetic state is in qualitative agreement with Ref. [203]. The dark blue star marks the asymmetry value for Sr-doped Ca_2RuO_4 at $456\,\mathrm{cm}^{-1}$ (B_{1g} channel), taken from Ref. [251].

tained from fits to a Fano profile: $I(\nu) = I_0(q + \epsilon)^2/(1 + \epsilon)^2$, with
$\epsilon = (\nu - \nu_p)/\Gamma$. Besides the phonon frequency ν_p and the effective
phonon linewidth Γ, we extract the Fano parameter q whose inverse
is directly proportional to the electron-phonon coupling strength V
and the imaginary part of the electronic susceptibility ρ [202, 203], *i.e.*
$1/q \propto V\rho$. In Fig. 5.8, we compare the asymmetry parameter $1/q$
of selected phonons (as indicated in Fig. 5.7) for S^*- and equilibrium
phases of Ca_2RuO_4. Interestingly, we find an increased asymmetry for
the current-stabilized phase suggesting an enhanced electronic suscep-
tibility to orbital and/or charge fluctuations [254, 255]. For low and
high temperatures in the equilibrium phases and for low currents in
the nonequilibrium phase, we find nearly negligible asymmetry param-
eters for all phonons investigated.

The presence of charge and orbital fluctuations has already been dis-
cussed in the equilibrium phases of Ca_2RuO_4. The Fano asymmetry in
the paramagnetic insulating state of Ca_2RuO_4 was attributed to orbital
fluctuations [157, 203], similar to observations in Ir- and Ti- based cor-
related oxides [249, 250]. Sr-doped metallic Ca_2RuO_4 exhibits a larger
asymmetry due to coupling to charge fluctuations [251, 253]. Our data
show that the asymmetry $1/q$ in the nonequilibrium S^*-phase is even
larger, possibly because both orbital and charge channels contribute
in the semimetallic state. Additionally, we point out that the ratio
of asymmetry parameters for B_{1g} and A_g is different in the nonequi-
librium and equilibrium phases. In the current-stabilized states $1/q$
is larger for the A_g channel, which further supports the appearance
of charge fluctuations. Detailed theoretical work is required to single
out and quantify the different contributions from charge and orbital
fluctuations.

5.4 Conclusions and outlook

In summary, we studied the nonequilibrium phases of Ca_2RuO_4 using Raman light scattering. Comparing Stokes and anti-Stokes Raman signals demonstrates that Joule heating can be avoided by external cooling. Therefore, it is evident that the nonequilibrium phases can be triggered via a true current-induced transition. In addition, our data have revealed pronounced Fano asymmetries of several phonons and the current-driven disappearance of the magnon excitations in the nonequilibrium S^*- phase. These observations are signatures of an electronic structure that is different from any of the previously studied equilibrium phases.

In the future, it will be instructive to extend our Raman experiments to nonzero momentum transfer by using intermediate-energy resonant inelastic x-ray scattering at the Ru L edges [256]. It would be also beneficial to perform scattering experiments with applied electrical current on ruthenates and other compounds that are less insulating in nature, such as the Ti-substituted bilayer ruthenate $Ca_3(Ru_{1-x}Ti_x)_2O_7$ [257], as this would allow to explore more in detail the effect of small structural modifications in the low current regimes.

Summary and outlook

In summary, the studies presented in this thesis demonstrate how various perturbation methods can be exploited to tailor the microscopic, and consequently also the macroscopic response of TMO systems. We focused on two prototypical correlated oxide systems, rare-earth nickelates and single-layer ruthenates. Using heterostructuring and electrical current, we stabilize exotic, nonequilibrium phases which are distinct from known bulk phases and of potential interest for future electronic devices and novel applications. All our studies employ advanced spectroscopic methods, such as resonant inelastic x-ray scattering, and theoretical models, as this synergetic combination enables to extract fundamental material parameters. Through this we demonstrate that light scattering is a powerful tool to probe the structural and electronic properties in various correlated oxide materials. In the following paragraphs we summarize the main findings of this thesis and put them in a broader context to highlight possible new research directions for TMOs in anticipation of a great future for quantum materials.

Chapters 3 and 4 have been dedicated to the rare-earth nickelates, a particularly intriguing material system with several intertwined collective ordering phenomena. In Chapter 3 we use resonant inelastic x-ray scattering to simultaneously probe bond order and spin excitations in bulk-like films as well as samples with ultra-thin magnetically active layers. We show that a modified bond disproportionation is an effective tuning knob to change the magnetic state in rare-earth nickelates.

Based on the observation of collective spin excitations and a spin-only
model, we quantify the exchange interactions to answer fundamental
questions about the unique noncollinear spin structure in these systems.
In detail, we identify the importance of double-exchange interactions
for the stabilization of the noncollinear spin arrangement. In this way,
our approach enables a microscopic understanding of a long-debated
puzzle, and at the same time opens up perspectives for other designed
oxide heterostructures. We specifically emphasize the prospect to study
dynamically induced or modified magnetic ground states and exchange
couplings using our method [258, 259].

In Chapter 4, we develop an extraordinarily high level of under-
standing and control of the bond-disproportionated phase in conjunc-
tion with the structural properties of rare-earth nickelates. We observe
that changes in the bond disproportionation have a crucial influence on
the metal-to-insulator and the magnetic transitions. Our study spot-
lights the important role of the oxygen ligands in electronic transitions,
which sometimes is overseen. As an outlook for future investigations
we suggest to control phase transitions and properties of TMOs by the
nature and stochiometry of the anion lattice.

The methodologies developed in Chapters 3 and 4 can be read-
ily applied to superconducting infinite-layer nickelate thin films, which
have been synthesized only very recently [129, 260]. In particular, the
quantification of exchange interactions and the crucial role of oxygen
positions is essential to develop a microscopic understanding of the su-
perconducting phase of these materials. Obviously, our approach can
be also extended to other TMOs with intertwined magnetic, orbital,
and structural degrees of freedom.

In Chapter 5, we exemplify that a SOC enhanced structure-property
relationship can be used to continuously tune the electronic properties
in Ca_2RuO_4 using electrical current. We answer fundamental questions
that lie at the core of several ongoing debates by means of Raman light
scattering. One of those questions concerns the role of current-induced

Joule heating, where we could show that active cooling can prevent any significant heating effects in the sample. With this established, we were able to unambiguously attribute the emergent semimetallic behavior to orbital and charge fluctuations. Our approach can serve as a blue-print for the integration of *in-operando* devices in light scattering experiments. This is of specific interest for systems, where small modifications in the lattice are reflected by substantial changes in the macroscopic response, such as Ir-based TMOs [29]. In a broader perspective, the direct observation of tunable properties by electric fields or currents is particularity relevant for material systems with ferroelectric and piezoelectric properties, or for the *in-situ* study of batteries.

In the future, it will be intriguing to further explore different phases of correlated oxide materials to realize unconventional states of matter with unprecedented properties and functionalities. One particularly fascinating state of matter with direct manifestations of quantum mechanics is the quantum spin liquid. In a quantum spin liquid long-range magnetic order is absent even at zero temperature due to the presents of large quantum fluctuations. Instead the system hosts a long-range quantum entangled magnetic state with fractionalized spin degrees of freedom, giving rise to nontrivial topological order and nontrivial elementary excitations [261]. The Kitaev spin liquid is an intriguing example of a quantum spin liquid, as the elementary excitations are predicted to be Majorana fermions. The spin-only Hamiltonian of the Kitaev spin liquid can be solved exactly and therefore provides a good and fertile playground for several theoretical predictions [262,263]. The possible experimental realizations of this exotic state of matter is — as anticipated by theory— limited to a few promising material candidates, and often comprises TM ions with substantial SOC, such as Ru and Ir [264]. Signatures of Majorana fermions as excitations have been so far found in α-RuCl$_3$ [265]. In addition, the honeycomb compound H$_3$LiIr$_2$O$_6$ was characterized as a quantum liquid state, even though the Kitaev-type quantum spin liquid has not yet been identified [266]. Light

scattering experiments in analogy to the ones presented in this thesis
will help to further understand this exotic state of matter, thereby con-
tributing to pave the way towards topological quantum computing[3].

In addition to the quest to answer fundamental questions in quan-
tum mechanics, one might explore new ways to tune the properties
of quantum materials. Among others, one could think of using moiré
engineering in analogy to twisted bilayer graphene [268] to enrich the
properties and functionalities of oxides materials [269]. In a moiré su-
perlattice two layers of a material are stacked and form a quasi-periodic
pattern, which can be altered continuously by changing the respective
orientation of the two layers [270]. So far moiré lattices were mostly re-
alized in stacked Van-der-Waals materials such as graphene. Recently,
the discovery of emergent many-body ground states sparked new inter-
est in these compounds. In particular, the attention focused on the dis-
covery of superconductivity in magic-angle bilayer graphene: two single
layers of graphene stacked with a "magic" angle of 1.1° with respect to
each other [268,271]. Importantly, the phase diagram of twisted bilayer
graphene is reminiscent of the one from high-T_c cuprates (see Fig. 1).
The presence of correlations induced by the moiré lattice [272] is re-
flected in several common features in both phase diagrams, such as the
dome-like shape of the transition temperature T_c as a function of carrier
concentration, asymmetry between hole and electron doping, and the
proximity to a variety of controllable magnetic phases [273–275]. While
the exact pairing mechanism in twisted bilayer graphene is currently
still under debate, moiré superlattices could be a promising platform
to study unconventional superconductivity.

Inspired by these appealing observations, one might be tempted
to exploit the possibilities of moiré engineering beyond Van-der-Waals
materials and transfer the concepts to strongly correlated materials. A

---

[3]As a first step, we have performed a resonant inelastic x-ray scattering study
at the Ru L edge [197,256,267] on the Kitaev model system RuCl$_3$, which allowed
us to quantify the exchange interactions. The manuscript has been submitted for
publication and can be found as item 11) in the List of Publications.

recent study by Chen *et al.* uses two different kinds of stripe patterns for epitaxially grown $La_{0.67}Sr_{0.33}MnO_3$ on $LaAlO_3$ to realize a TMO-based moiré lattice [269]. In addition to stripe domains, which form periodically from local relaxation of the strain imposed by substrate, the system hosts miscut stripes. The latter develop from the surface miscut, *i.e.* the fact that the crystallographic axes do not exactly coincide with the surface. The combination of both kind of stripes in the films yields a moiré pattern reflected in the electronic landscape. The emergent moiré pattern was experimentally verified by a spatially modulated optical conductivity and ferromagnetism. This first realization of an oxide-based moiré lattice probably marks the genesis of an incipient research field of enormous potential and one can only surmise the variety of properties and functionalities that could be realized with TMO materials. Using twistronics, the boundaries set by heterostructuring could be overcome and oxide materials might offer the same flexibility as layered two-dimensional materials.

The above mentioned unprecedented functionalities could pave the way for next-generation energy storage and conversion devices based on quantum materials. I deeply hope that these fascinating materials contribute and help our society to shape a green and sustainable future for all of us.

Bibliography

[1] M. S. Senn, J. P. Wright, and J. P. Attfield, Nature **481**, 173 (2012).

[2] B. Keimer *et al.*, Nature **518**, 179 (2015).

[3] J. G. Bednorz and K. A. Müller, Z. Phys. B **64**, 189 (1986).

[4] B. Keimer and J. E. Moore, Nat. Phys. **13**, 1045 (2017).

[5] R. Ramesh and D. G. Schlom, Nat. Rev. Mater. **4**, 257 (2019).

[6] R. J. Green, M. W. Haverkort, and G. A. Sawatzky, Phys. Rev. B **94**, 195127 (2016).

[7] J. Shi *et al.*, Nat. Commun. **4**, 2676 (2013).

[8] J. B. Torrance *et al.*, Phys. Rev. B **45**, 8209 (1992).

[9] J. L. García-Muñoz, J. Rodríguez-Carvajal, and P. Lacorre, Europhys. Lett. **20**, 241 (1992).

[10] M. L. Medarde, J. Phys.: Condens. Matter **9**, 1679 (1997).

[11] H. Guo *et al.*, Nat. Commun. **9** (2018).

[12] J. Shi, Y. Zhou, and S. Ramanathan, Nat. Commun. **5**, 4860 (2014).

[13] H.-T. Zhang *et al.*, Nat. Commun. **10**, 1651 (2019).

[14] Z. Zhang *et al.*, Nature **553**, 68 (2018).

[15] F. Zuo *et al.*, Nat. Commun. **8**, 240 (2017).

[16] R. Jaramillo *et al.*, Nat. Phys. **10**, 304 (2014).

[17] J. Chen *et al.*, ACS Appl. Mater. Interfaces **11**, 34128 (2019).

[18] Y. Zhou *et al.*, Nature **534**, 231 (2016).

[19] A. M. Glazer, Acta Cryst. B **28**, 3384 (1972).

[20] S. J. May *et al.*, Phys. Rev. B **82**, 014110 (2010).

[21] D. N. Basov, R. D. Averitt, and D. Hsieh, Nat. Mater. **16**, 1077 (2017).

[22] H. Takagi and H. Y. Hwang, Science **327**, 1601 (2010).

[23] F. Lyzwa *et al.*, Phys. Rev. Mater. **4**, 043606 (2020).

[24] D. Lee *et al.*, Science **362**, 1037 (2018).

[25] N. Reyren *et al.*, Science **317**, 1196 (2007).

[26] A. Ohtomo and H. Y. Hwang, Nature **427**, 423 (2004).

[27] J. A. Mundy *et al.*, Nature **537**, 523 (2016).

[28] H.-H. Kim *et al.*, Science **362**, 1040 (2018).

[29] G. Cao *et al.*, Phys. Rev. Lett. **120**, 017201 (2018).

[30] M. Nakano *et al.*, Nature **487**, 459 (2012).

[31] J. Jeong *et al.*, Science **339**, 1402 (2013).

[32] M. Nakano *et al.*, Appl. Phys. Lett. **103**, 153503 (2013).

[33] C. H. Ahn, J.-M. Triscone, and J. Mannhart, Nature **424**, 1015 (2003).

[34] H. Tanaka, J. Zhang, and T. Kawai, Phys. Rev. Lett. **88**, 027204 (2001).

[35] P. Cox, *Transition Metal Oxides: An Introduction to their Electronic Structure and Properties* Oxford University Press, Oxford, 2010.

[36] R. Cowan, *The Theory of Atomic Structure and Spectra* University of California Press, Berkeley, 1981.

[37] D. I. Khomskii, *Transition Metal Compounds* Cambridge University Press, Cambridge, 2014.

[38] V. I. Anisimov, M. A. Korotin, and E. Z. Kurmaev, J. Phys. Condens. Matter **2**, 3973 (1991).

[39] Y. Mita *et al.*, Phys. Status Solidi B **223**, 247 (2001).

[40] J. Hubbard and B. H. Flowers, J. Proc. R. Soc. A **276**, 238 (1963).

[41] J. Hubbard and B. H. Flowers, J. Proc. R. Soc. A **281**, 401 (1964).

[42] The Hubbard model at half a century, Nat. Phys. Editorial **9**, 523 (2003).

[43] M. Schmitt *et al.*, Phys. Rev. B **100**, 054431 (2019).

[44] A. V. Chumak *et al.*, Nat. Phys. **11**, 453 (2015).

[45] M. W. Haverkort, *Spin and orbital degrees of freedom in transition metal oxides and oxide thin films studied by soft x-ray absorption spectroscopy* PhD thesis, University of Cologne Faculty of Mathematics and Natural Sciences Physics Department, 2005.

[46] M. W. Haverkort, M. Zwierzycki, and O. K. Andersen, Phys. Rev. B **85**, 165113 (2012).

[47] K. Fürsich *et al.*, Phys. Rev. B **97**, 165126 (2018).

[48] B. J. Kim *et al.*, Phys. Rev. Lett. **101**, 076402 (2008).

[49] B. Zwartsenberg *et al.*, Nat. Phys. **16**, 290 (2020).

[50] A. Jain *et al.*, Nat. Phys. **13**, 633 (2017).

[51] C. Dietl, *Synthesis and Electronic Ordering Phenomena of Calcium Ruthenate Thin Films* PhD thesis, University of Stuttgart, 2018.

[52] K. Fürsich, The optical constants of nio studied with resonant x-ray reflectivity and cluster calculations Master's thesis, Julius-Maximilians Universität Würzburg, 2016.

[53] C. Ballhausen, *Introduction to Ligand Field Theory* McGraw-Hill Book Co., New York, 1962.

[54] F. D. Groot and A. Kotani, *Core Level Spectroscopy of Solids* Taylor and Francis CRC Press, Boca Raton, 2008.

[55] Z. Fang, N. Nagaosa, and K. Terakura, Phys. Rev. B **69**, 045116 (2004).

[56] G. Khaliullin, Phys. Rev. Lett. **111**, 197201 (2013).

[57] A. Akbari and G. Khaliullin, Phys. Rev. B **90**, 035137 (2014).

[58] J. Chaloupka and G. Khaliullin, Phys. Rev. Lett. **116**, 017203 (2016).

[59] S.-M. Souliou *et al.*, Phys. Rev. Lett. **119**, 067201 (2017).

[60] P. Rivero, V. Meunier, and W. Shelton, Phys. Rev. B **93**, 024111 (2016).

[61] M. Reehuis *et al.*, Phys. Rev. B **73**, 144513 (2006).

[62] T. J. Regan *et al.*, Phys. Rev. B **64**, 214422 (2001).

[63] F. C. Zhang and T. M. Rice, Phys. Rev. B **37**, 3759 (1988).

[64] P. W. Anderson, Science **235**, 1196 (1987).

[65] L. H. Tjeng *et al.*, Phys. Rev. Lett. **78**, 1126 (1997).

[66] J. Zaanen, G. A. Sawatzky, and J. W. Allen, Phys. Rev. Lett. **55**, 418 (1985).

[67] A. E. Bocquet *et al.*, Phys. Rev. B **46**, 3771 (1992).

[68] T. Harano *et al.*, Appl. Phys. Lett. **102**, 222404 (2013).

[69] T. Burnus, *Study of Charge, Spin and Orbital States in Novel Transition-Metal Oxides Using X-Ray Absorption Spectroscopy* PhD thesis, University of Cologne Faculty of Mathematics and Natural Sciences Physics Department, 2008.

[70] D. Alders *et al.*, Phys. Rev. B **57**, 11623 (1998).

[71] G. A. Sawatzky and J. W. Allen, Phys. Rev. Lett. **53**, 2339 (1984).

[72] M. Jiang, M. Berciu, and G. A. Sawatzky, Phys. Rev. Lett. **124**, 207004 (2020).

[73] M. A. Korotin *et al.*, Phys. Rev. Lett. **80**, 4305 (1998).

[74] I. I. Mazin *et al.*, Phys. Rev. Lett. **98**, 176406 (2007).

[75] V. Bisogni *et al.*, Nat. Commun. **7** (2016).

[76] E. Pavarini *et al.*, *Quantum Materials: Experiments and Theory, Modeling and Simulation, Vol. 6* Verlag des Forschungszentrum Jülich, 2016.

[77] S. Catalano *et al.*, Rep. Prog. Phys **81**, 046501 (2018).

[78] T. Mizokawa, D. I. Khomskii, and G. A. Sawatzky, Phys. Rev. B **61**, 11263 (2000).

[79] S. B. Lee, R. Chen, and L. Balents, Phys. Rev. Lett. **106**, 016405 (2011).

[80] S. B. Lee, R. Chen, and L. Balents, Phys. Rev. B **84**, 165119 (2011).

[81] H. Park, A. J. Millis, and C. A. Marianetti, Phys. Rev. Lett. **109**, 156402 (2012).

[82] A. Subedi, O. E. Peil, and A. Georges, Phys. Rev. B **91**, 075128 (2015).

[83] J. Varignon *et al.*, npj Quantum Mater. **2**, 2397 (2017).

[84] H. Y. Hwang *et al.*, Nat. Mater. **11**, 103 (2012).

[85] S. Catalano *et al.*, APL Mater. **3**, 062506 (2015).

[86] A. Frano *et al.*, Phys. Rev. Lett. **111**, 106804 (2013).

[87] M. Wu *et al.*, Phys. Rev. B **88**, 125124 (2013).

[88] M. Zaghrioui *et al.*, Phys. Rev. B **64**, 081102 (2001).

[89] J. Kanamori, J. Appl. Phys. **31**, 14 (1960).

[90] Y. Murakami *et al.*, Phys. Rev. Lett. **81**, 582 (1998).

[91] K. Kugel and D. Khomskii, Zh. Eksp. Teor. Fiz. **64**, 1429 (1972).

[92] J. A. Alonso *et al.*, Phys. Rev. Lett. **82**, 3871 (1999).

[93] J. A. Alonso *et al.*, Phys. Rev. B **61**, 1756 (2000).

[94] S. Johnston *et al.*, Phys. Rev. Lett. **112**, 106404 (2014).

[95] I. Vobornik *et al.*, Phys. Rev. B **60**, R8426 (1999).

[96] J. L. García-Muñoz, J. Rodríguez-Carvajal, and P. Lacorre, Phys. Rev. B **50**, 978 (1994).

[97] J. Rodríguez-Carvajal *et al.*, Phys. Rev. B **57**, 456 (1998).

[98] V. Scagnoli *et al.*, Phys. Rev. B **73**, 100409 (2006).

[99] V. Scagnoli *et al.*, Phys. Rev. B **77**, 115138 (2008).

[100] Y. Lu *et al.*, Phys. Rev. X **8**, 031014 (2018).

[101] J. Mannhart and D. G. Schlom, Science **327**, 1607 (2010).

[102] Y. E. Suyolcu *et al.*, J. Supercond. and Nov. Magn. , 1 (2019).

[103] F. Wrobel *et al.*, Appl. Phys. Lett. **110**, 041606 (2017).

[104] J. Liu *et al.*, Appl. Phys. Lett. **96**, 233110 (2010).

[105] S. Middey *et al.*, Annu. Rev. Mater. Res. **46**, 305 (2016).

[106] M. Imada, A. Fujimori, and Y. Tokura, Rev. Mod. Phys. **70**, 1039 (1998).

[107] J. Chakhalian *et al.*, Nat. Phys. **2**, 244 (2006).

[108] J. Chakhalian *et al.*, Science **318**, 1114 (2007).

[109] E. Benckiser *et al.*, Nat. Mater. **10**, 189 (2011).

[110] A. Gozar *et al.*, Nature **455**, 782 (2007).

[111] D. G. Schlom *et al.*, Annual Review of Materials Research **37**, 589 (2007).

[112] A. Vailionis *et al.*, Phys. Rev. B **83**, 064101 (2011).

[113] Y. E. Suyolcu *et al.*, Scientific Reports **7**, 453 (2017).

[114] R. Scherwitzl *et al.*, Adv. Mater. **22**, 5517 (2010).

[115] J. Chaloupka and G. Khaliullin, Phys. Rev. Lett. **100**, 016404 (2008).

[116] P. Hansmann *et al.*, Phys. Rev. Lett. **103**, 016401 (2009).

[117] S. Middey *et al.*, Phys. Rev. Lett. **116**, 056801 (2016).

[118] G. Giovannetti *et al.*, Phys. Rev. Lett. **103**, 156401 (2009).

[119] J. van den Brink and D. I. Khomskii, J. Phys.: Condens. Matter **20**, 434217 (2008).

[120] A. S. Disa *et al.*, APL Mater. **3**, 062303 (2015).

[121] A. V. Boris *et al.*, Science **332**, 937 (2011).

[122] Y. Lu *et al.*, Phys. Rev. B **93**, 165121 (2016).

[123] M. Hepting *et al.*, Phys. Rev. Lett. **113**, 227206 (2014).

[124] M. Wu *et al.*, Phys. Rev. B **91**, 195130 (2015).

[125] O. Janson and K. Held, Phys. Rev. B **98**, 115118 (2018).

[126] M. Hepting *et al.*, Nat. Phys. **14**, 1097 (2018).

[127] C. Domínguez *et al.*, Nat. Mater. (2020).

[128] D. Li *et al.*, Nature **572**, 624 (2019).

[129] D. Li *et al.*, (2020).

[130] A. S. Botana and M. R. Norman, Phys. Rev. X **10**, 011024 (2020).

[131] X. Wu *et al.*, Phys. Rev. B **101**, 060504 (2020).

[132] Y. Lu *et al.*, Phys. Rev. B **95**, 195117 (2017).

[133] J. Ruppen *et al.*, Phys. Rev. B **96**, 045120 (2017).

[134] A. Hampel and C. Ederer, Phys. Rev. B **96**, 165130 (2017).

[135] H. Qi *et al.*, J. Mater. Sci **50**, 5300 (2015).

[136] Z. Liao *et al.*, Nat. Mater. **15**, 425 (2016).

[137] D. Kan *et al.*, Nat. Mater. **15**, 432 (2016).

[138] M. W. Haverkort *et al.*, Phys. Rev. Lett. **101**, 026406 (2008).

[139] C. Dietl *et al.*, Appl. Phys. Lett. **112**, 031902 (2018).

[140] E. Dagotto, Science **309**, 257 (2005).

[141] S. Nakatsuji and Y. Maeno, Phys. Rev. Lett. **84**, 2666 (2000).

[142] Y. Maeno *et al.*, Nature. **372**, 532 (1994).

[143] J. P. Carlo *et al.*, Nat. Mater. **11**, 323 (2012).

[144] G. M. Luke *et al.*, Nature **394**, 558 (1998).

[145] K. Ishida *et al.*, Nature **396**, 658 (1998).

[146] M. Rice, Nature **396**, 627 (1998).

[147] I. I. Mazin and D. J. Singh, Phys. Rev. Lett. **82**, 4324 (1999).

[148] A. Damascelli *et al.*, Phys. Rev. Lett. **85**, 5194 (2000).

[149] A. P. Mackenzie *et al.*, npj Quantum Mater. **2**, 40 (2017).

[150] A. P. Mackenzie *et al.*, Phys. Rev. Lett. **76**, 3786 (1996).

[151] A. P. Mackenzie and Y. Maeno, Rev. Mod. Phys. **75**, 657 (2003).

[152] S. A. Kivelson *et al.*, arXiv:2002.00016 (2020).

[153] A. Pustogow *et al.*, Nature **574**, 72 (2019).

[154] K. Ishida *et al.*, J. Phys. Soc. Jpn. **89**, 034712 (2020).

[155] Z. Wang, X. Wang, and C. Kallin, Phys. Rev. B **101**, 064507 (2020).

[156] F. B. Kugler *et al.*, Phys. Rev. Lett. **124**, 016401 (2020).

[157] I. Zegkinoglou *et al.*, Phys. Rev. Lett. **95**, 136401 (2005).

[158] H. Liu and G. Khaliullin, Phys. Rev. Lett. **122**, 057203 (2019).

[159] M. Braden *et al.*, Phys. Rev. B **58**, 847 (1998).

[160] J. H. Jung *et al.*, Phys. Rev. Lett. **91**, 056403 (2003).

[161] C. S. Alexander *et al.*, Phys. Rev. B **60**, R8422 (1999).

[162] O. Friedt *et al.*, Phys. Rev. B **63**, 174432 (2001).

[163] F. Nakamura *et al.*, Phys. Rev. B **65**, 220402(R) (2002).

[164] F. Nakamura *et al.*, Sci. Rep. **3**, 2536 (2013).

[165] R. Okazaki *et al.*, J. Phys. Soc. Jpn. **82**, 103702 (2013).

[166] J. Zhang *et al.*, Phys. Rev. X **9**, 011032 (2019).

[167] C. Sow *et al.*, Science **358**, 1084 (2017).

[168] J. Bertinshaw *et al.*, Phys. Rev. Lett. **123**, 137204 (2019).

[169] G. Mattoni, S. Yonezawa, and Y. Maeno, Appl. Phys. Lett. **116**, 172405 (2020).

[170] M.-C. Lee *et al.*, Phys. Rev. B **98**, 161115(R) (2018).

[171] Y. Lu, *From Itinerant to Localized: an x-ray spectroscopic study of transition metal oxides* PhD thesis, University of Stuttgart, 2017.

[172] H. Kuzmany, *Solid-State Spectroscopy –An Introduction* Springer, Berlin, Heidelberg, 2009.

[173] M. Cardona and G. Güntherodt, *Light Scattering in Solids II: Basic Concepts and Instrumentation*, volume 50 Springer, 1982.

[174] W. Hayes and R. Loudon, *Scattering of Light by Crystals* Dover Publications, Inc., Mineloa, NY, 2004.

[175] L. J. P. Ament *et al.*, Rev. Mod. Phys. **83**, 705 (2011).

[176] L. J. P. Ament *et al.*, Phys. Rev. Lett. **103**, 117003 (2009).

[177] D. Betto *et al.*, Phys. Rev. B **96**, 020409 (2017).

[178] L. Braicovich *et al.*, Phys. Rev. Lett. **104**, 077002 (2010).

[179] J. Zhang *et al.*, Cryst. Growth Des. **17**, 2730 (2017).

[180] H. Zheng *et al.*, Crystals **9**, 324 (2019).

[181] B.-X. Wang *et al.*, Phys. Rev. Mater. **2**, 064404 (2018).

[182] C. Ulrich *et al.*, Phys. Rev. Lett. **103**, 107205 (2009).

[183] E. Benckiser et al., Phys. Rev. B **88**, 205115 (2013).

[184] G. Fabbris et al., Phys. Rev. Lett. **117**, 147401 (2016).

[185] A. Hariki, M. Winder, and J. Kuneš, Phys. Rev. Lett. **121**, 126403 (2018).

[186] G. Ghiringhelli et al., J. Phys.: Condens. Matter **17**, 5397 (2005).

[187] Y. Y. Peng et al., Phys. Rev. B **92**, 064517 (2015).

[188] S. Moser et al., Phys. Rev. Lett. **115**, 096404 (2015).

[189] T. P. Devereaux et al., Phys. Rev. X **6**, 041019 (2016).

[190] T. P. Devereaux and R. Hackl, Rev. Mod. Phys. **79**, 175 (2007).

[191] J. Fink et al., Rep. Prog. Phys. **76**, 056502 (2013).

[192] M. Bluschke, *Resonant X-ray Scattering Studies of Collective Electronic States in Cuprates and Nickelates Controlled by Isovalent Chemical Substitution and Epitaxial Integration* PhD thesis, Technische Univesität Berlin, 2019.

[193] A. Frano, *Spin Spirals and Charge Textures in Transition-Metal-Oxide Heterostructures* PhD thesis, Technische Univesität Berlin, 2017.

[194] N. B. Brookes et al., Nuclear Instruments and Methods in Physics Research Section A: Accelerators, Spectrometers, Detectors and Associated Equipment **903**, 175 (2018).

[195] ESRF, State-of-the-art id32 rixs sepctrometer, 2020.

[196] G. Ghiringhelli et al., Rev. Sci. Instrum. **77**, 113108 (2006).

[197] H. Gretarsson et al., J. Synchrotron Rad. **27**, 538 (2020).

[198] M. Moretti Sala et al., J. Synchrotron Rad. **25**, 580 (2018).

[199] R. Fumagalli et al., Phys. Rev. B **99**, 134517 (2019).

[200] M. Hepting et al., Physica B: Condensed Matter **460**, 196 (2015) Special Issue on Electronic Crystals (ECRYS-2014).

[201] U. Fano, Phys. Rev. **124**, 1866 (1961).

[202] S. Naler *et al.*, Phys. Rev. B **65**, 092401 (2002).

[203] H. Rho *et al.*, Phys. Rev. B **71**, 245121 (2005).

[204] M. W. Haverkort *et al.*, Europhys. Lett. **108**, 57004 (2014).

[205] Y. Lu *et al.*, Phys. Rev. B **90**, 085102 (2014).

[206] R. Kubo, Phys. Rev. **87**, 568 (1952).

[207] P. W. Anderson, Phys. Rev. **86**, 694 (1952).

[208] S. Toth and B. Lake, J. Phys.: Condens. Matter **27**, 166002 (2015).

[209] T. Holstein and H. Primakoff, Phys. Rev. **58**, 1098 (1940).

[210] P. G. de Gennes, Phys. Rev. **118**, 141 (1960).

[211] H. A. Bethe, Z. Physik **71**, 205 (1931).

[212] T. Mizokawa *et al.*, Phys. Rev. Lett. **67**, 1638 (1991).

[213] J. M. Wills and W. A. Harrison, Phys. Rev. B **28**, 4363 (1983).

[214] C. Piamonteze *et al.*, Phys. Rev. B **71**, 020406 (2005).

[215] J. W. Freeland, M. van Veenendaal, and J. Chakhalian, J. Electron Spectrosc. Relat. Phenom. **208**, 56 (2016).

[216] J. Ruppen *et al.*, Phys. Rev. B **92**, 155145 (2015).

[217] U. Staub *et al.*, Phys. Rev. Lett. **88**, 126402 (2002).

[218] J. L. García-Muñoz *et al.*, Phys. Rev. B **79**, 134432 (2009).

[219] M. Medarde, M. T. Fernández-Díaz, and P. Lacorre, Phys. Rev. B **78**, 212101 (2008).

[220] A. Frano *et al.*, Adv. Mater. **26**, 258 (2014).

[221] M. M. Sala *et al.*, New J. Phys. **13**, 043026 (2011).

[222] M. Medarde *et al.*, Phys. Rev. B **80**, 245105 (2009).

[223] B. Lau and A. J. Millis, Phys. Rev. Lett. **110**, 126404 (2013).

[224] J. Shamblin *et al.*, Nat. Commun. **9** (2018).

[225] B. Li *et al.*, Adv. Electron. Mater. **2**, 1500261 (2016).

[226] H. K. Yoo *et al.*, Sci. Rep. **5** (2015).

[227] V. Bisogni *et al.*, Phys. Rev. B **85**, 214527 (2012).

[228] P. W. Anderson and H. Hasegawa, Phys. Rev. **100**, 675 (1955).

[229] J.-H. Kim *et al.*, Phys. Rev. Lett. **113**, 147206 (2014).

[230] G. Khaliullin and R. Kilian, Phys. Rev. B **61**, 3494 (2000).

[231] K. Nakajima *et al.*, J. Phys. Soc. Jpn. **62**, 4438 (1993).

[232] S. Balandeh *et al.*, Phys. Rev. B **96**, 165127 (2017).

[233] A. Khazraie *et al.*, Phys. Rev. B **97**, 075103 (2018).

[234] D. V. Efremov, J. van den Brink, and D. I. Khomskii, Nat. Mater. **3**, 853 (2004).

[235] K. Takubo *et al.*, Phys. Rev. B **90**, 081104 (2014).

[236] J. Liu *et al.*, Nat. Commun. **4**, 1 (2013).

[237] T. Kim *et al.*, Nature **533**, 68 (2016).

[238] J. Chakhalian, X. Liu, and G. A. Fiete, arXiv:2003.12211 (2020).

[239] K. Fürsich *et al.*, Phys. Rev. B **99**, 165124 (2019).

[240] L. Vasylechko *et al.*, Journal of alloys and compounds **297**, 46 (2000).

[241] Y. E. Suyolcu, *Atomic-Scale Control and Characterization of Oxide Heterostructures: Correlating Interfacial Structure and Novel Functionalities* PhD thesis, Technische Universität Darmstadt, 2019.

[242] G. Kresse and J. Furthmüller, Phys. Rev. B **54**, 11169 (1996).

[243] G. Kresse and D. Joubert, Phys. Rev. B **59**, 1758 (1999).

[244] J. P. Perdew, K. Burke, and M. Ernzerhof, Phys. Rev. Lett. **77**, 3865 (1996).

[245] M. Bluschke *et al.*, Phys. Rev. Lett. **118**, 207203 (2017).

[246] S. Nakatsuji and Y. Maeno, J. Solid State Chem. **156**, 26 (2001).

[247] Y. S. Ponosov and S. V. Streltsov, Phys. Rev. B **86**, 045138 (2012).

[248] I. P. Herman, J. Appl. Phys. **109**, 016103 (2011).

[249] H. Gretarsson *et al.*, Phys. Rev. Lett. **116**, 136401 (2016).

[250] C. Ulrich *et al.*, Phys. Rev. Lett. **115**, 156403 (2015).

[251] H. Rho *et al.*, Phys. Rev. B **68**, 100404(R) (2003).

[252] J. Jung, Solid State Commun. **133**, 103 (2005).

[253] S. Sakita *et al.*, Phys. Rev. B **63**, 134520 (2001).

[254] T. Mizokawa *et al.*, Phys. Rev. Lett. **87**, 077202 (2001).

[255] M. Sakaki *et al.*, J. Phys. Soc. Jpn. **82**, 093707 (2013).

[256] H. Suzuki *et al.*, Nat. Mater. **18**, 563 (2019).

[257] C. Sow *et al.*, Phys. Rev. Lett. **122**, 196602 (2019).

[258] A. S. Disa *et al.*, Nat. Phys. (2020).

[259] K. R. Beyerlein *et al.*, Phys. Rev. B **102**, 014311 (2020).

[260] M. Osada *et al.*, Nano Lett. **20**, 5735 (2020).

[261] H. Takagi *et al.*, Nat. Rev. Phys. **1**, 264 (2019).

[262] G. Jackeli and G. Khaliullin, Phys. Rev. Lett. **102**, 017205 (2009).

[263] L. Janssen and M. Vojta, Journal of Physics: Condensed Matter **31**, 423002 (2019).

[264] J. A. Sears *et al.*, Nat. Phys. (2020).

[265] S.-H. Do *et al.*, Nat. Phys. **13**, 1079 (2017).

[266] K. Kitagawa *et al.*, Nature **554**, 341 (2018).

[267] H. Gretarsson *et al.*, Phys. Rev. B **100**, 045123 (2019).

[268] Y. Cao *et al.*, Nature **556**, 80 (2018).

[269] X. Chen *et al.*, Nat. Phys. (2020).

[270] M. Yankowitz *et al.*, Science **363**, 1059 (2019).

[271] Y. Cao *et al.*, Nature **556**, 43 (2018).

[272] A. Kerelsky *et al.*, Nature **572**, 95 (2019).

[273] L. A. Gonzalez-Arraga *et al.*, Phys. Rev. Lett. **119**, 107201 (2017).

[274] A. L. Sharpe *et al.*, Science **365**, 605 (2019).

[275] W.-Y. He, D. Goldhaber-Gordon, and K. T. Law, Nat. Commun. **11**, 1650 (2020).

Acknowledgment

The research work presented in this thesis would not have been possible without the help of my supervisors, mentors, co-workers, friends, and family. I would like to thank for the professional, technical, and personal support, which I received during the past four years of working on this thesis.

First and foremost, I like to thank Prof. Dr. Bernhard Keimer for giving me the opportunity to join his department at the Max Planck Institute and to work on a variety of fascinating projects. It was an invaluable experience for me to witness his dedication to science as well as his belief in great ideas and scientific integrity. His way to advise, train, and motivate students to become the next generation of great scientists is truly inspiring for me. I am especially grateful for the offered freedom to follow and develop my own interests and the possibility to participate in many exciting conferences, summer schools, and experiments.

Likewise, I like to thank my day-to-day supervisor Dr. Matteo Minola for his valuable guidance and fantastic support. Among others, Matteo introduced me to the amazing field of inelastic photon scattering, in particular RIXS, and I profited a lot from his experience and patient teaching. I highly appreciate the scientific discussions on numerous subjects and his constant motivation to explore new techniques, methods, and approaches. It has been a pleasure being part of his research group.

I consider myself very lucky, because I had two great day-to-day supervisors, thus I also like to thank Dr. Eva Benckiser for her supervision. I especially benefited from Eva's extensive knowledge on the nickelates, which she kindly and constantly shared with me.

I am grateful to Prof. Dr. Tilman Pfau, Prof. Dr. Maria Daghofer, and Prof. Dr. Vladimir Hinkov for being on my thesis committee, and I thank Dr. Hans Boschker and Dr. Hagen Klauk for their time and guidance as external supervisors.

Synchrotron-based research is intriguing, but sometimes it can be quite tiring to spend long night-shifts at the beamline. Fortunately, I was surrounded by many colleagues and beamline scientists. I thank Davide Betto and Yi Lu for being part of the exciting nickelate beamtimes at the ESRF in Grenoble and for their help to analyze the data and to perform the associated calculations. Many thanks to Martin Bluschke for his fantastic work at all BESSY beamtimes in Berlin. I greatly appreciate the selfless commitment from the numerous beamline scientists, I had the pleasure to work with. Many thanks to Enrico Schierle, Eugen Weschke, Nick Brookes, Hlynur Gretarsson, Markus Weigand, Sonia Francoual, Andi Barbour, Claudio Mazzoli, and Eli Rotenberg.

I am grateful for a fruitful collaboration with Y. Eren Suyolcu, where he provided beautiful STEM images of our samples. Similarly, I like to express my gratitude towards Joel Bertinshaw for introducing me to the Ca_2RuO_4 current project and for sharing some nice IRIXS beamtimes. I also thank Giniyat Khaliullin, Maurits W. Haverkort, Philipp Hansmann, and Zhicheng Zhong for their theory support.

During my whole PhD work, I benefited from the extraordinary environment offered by the Max Planck Institute, in particular I had direct access to excellent samples. I sincerely appreciate the work from Georg Christiani and Gennady Logvenov for growing all the nickelate samples. Likewise, I like to thank Maximilian Krautloher for providing shiny Ca_2RuO_4 crystals. None of my experiments would have been possible without their samples.

List of Publications

12) D. Betto, M. Bluschke, D. Putzky, E. Schierle, A. Amorese, **K. Fürsich**, S. Blanco-Canosa, G. Christiani, G. Logvenov, B. Keimer, and M. Minola: Imprint of charge and oxygen orders on Dy ions in $DyBa_2Cu_3O_{6+x}$ thin films probed by resonant x-ray scattering
submitted for publication, Sept. 2020, preprint: arXiv:2009.03574.

11) H. Suzuki*, H. Liu*, J. Bertinshaw, K. Ueda, H. Kim, S. Laha, D. Weber, Z. Yang, L. Wang, H. Takahashi, **K. Fürsich**, M. Minola, H.-C. Wille, B. V. Lotsch, B. J. Kim, H. Yavas, M. Daghofer, J. Chaloupka, G. Khaliullin, H. Gretarsson, and B. Keimer: Quantifying the Exchange Interactions in the Kitaev Model System $RuCl_3$ by Ru L edge Resonant Inelastic X-ray Scattering
submitted for publication, July 2020, preprint: arXiv:2008.02037.

10) Y. E. Suyolcu*, **K. Fürsich***, M. Hepting, Z. Zhong, Y. Lu, Y. Wang, G. Christiani, G.Logvenov, P. Hansmann, M. Minola, B. Keimer, P. A. van Aken, and E. Benckiser: Control of the metal-insulator transition in $NdNiO_3$ thin films through the interplay between structural and electronic properties
submitted for publication, June 2020.

9) F. Lyzwa, A. Chan, J. Khmaladze, **K. Fürsich**, B. Keimer, C. Bernhard, M. Minola, and B.P.P. Mallett: Backfolded acoustic phonons in metal-oxide superlattices
Phys. Rev. Materials **4**, 043606, 2020.

8) A. Seo, P. P. Stavropoulos, H.-H. Kim, **K. Fürsich**, M. Souri, J. G. Connell, H. Gretarsson, M. Minola, H. Y. Kee, and B. Keimer: Compressive strain induced enhancement of exchange interaction and short-range magnetic order in Sr_2IrO_4 investigated by Raman

spectroscopy
Phys. Rev. B **100**, 165106, 2019.

7) **K. Fürsich**, J. Bertinshaw, P. Butler, M. Krautloher, M. Minola, and B. Keimer: Raman Scattering from current-stabilized nonequilibrium phases in Ca_2RuO_4
Phys. Rev. B **100**, 081101 (R), 2019.

6) **K. Fürsich**, Y. Lu, D. Betto, M. Bluschke, J. Porras, E. Schierle, R. Ortiz, H. Suzuki, G. Cristiani, G.Logvenov, N.B. Brookes, M.W. Haverkort, M. Le Tacon, E. Benckiser, M. Minola, and B. Keimer: Resonant inelastic x-ray scattering study of bond order and spin excitations in nickelate thin-film structures
Phys Rev. B **99**, 165124, 2019.
Selected as **Editors' suggestion**.

5) Y. Lu*, D. Betto*, **K. Fürsich**, H. Suzuki, H.-H. Kim, G. Cristiani, G. Logvenov, N. B. Brookes, E. Benckiser, M.W. Haverkort, G. Khaliullin, M. Le Tacon, M. Minola, and B. Keimer: Site-selective Probe of Magnetic Excitations in Rare-earth Nickelates using Resonant Inelastic X-ray Scattering
Phys. Rev. X **8**, 031014, 2018.
Selected for **ESRF Highlights 2018**.

4) V. B. Zabolotnyy, **K. Fürsich**, R. J. Green, P. Lutz, K. Treiber, Chul-Hee Min, A. V. Dukhnenko, N. Y. Shitsevalova, V. B. Filipov, B. Y. Kang, B. K. Cho, R. Sutarto, Feizhou He, F. Reinert, D. S. Inosov, and V. Hinkov: Chemical and valence reconstruction at the surface of SmB_6 revealed by means of resonant soft x-ray reflectometry
Phys. Rev. B **97**, 205416, 2018.
Selected as **Editors' suggestion** and for **Kaleidoscope**.

3) **K. Fürsich**, V. B. Zabolotnyy, E. Schierle, L. Dudy, O. Kirilmaz, M. Sing, R. Claessen, R. J. Green, M. W. Haverkort, and V. Hinkov: Theory-restricted resonant x-ray reflectometry of quantum materials
Phys. Rev. B **97**, 165126, 2018.

2) N. Nijem, **K. Fürsich**, H. Bluhm, S.R. Leone, and M.K. Gilles: Ammonia adsorption and co-adsorption with water in HKUST-1: Spectroscopic evidence for cooperative interactions
J. Phys. Chem. C **119**, 24781, 2015.

1) N. Nijem, **K. Fürsich**, S.T. Kelly, C. Swain, S.R. Leone, and M. K. Gilles: HKUST-1 thin film layer-by-layer liquid phase epitaxial growth: Film properties and stability dependence on layer number
Cryst. Growth Des. **15**, 6, 2015.

*: equal contribution

Conference Contributions

Resonant x-ray scattering of novel phases in metal oxides stabilized by heteroepitaxy, ***invited full-length online colloquium talk***, *physics department*, University of Massachusetts, Dartmouth, USA, 2020.

Resonant x-ray scattering study of bond order and spin excitations in nickelate thin-film structures, *European Powder Diffraction Conference (EPDIC)*, **invited keynote talk***, Sibenik, Croatia, 2020.
*postponed to 2021 due to COVID-19

Raman scattering from current-stabilized nonequilibrium phases in Ca_2RuO_4, *Interdepartmental MPI-FKF Seminar* "Functional Materials", Stuttgart, Germany, 2020.

Interface induced structural and magnetic reconstructions in nickelate thin film structures, *Helmholtz-Zentrum Berlin BESSYII user meeting, **invited talk** at the young scientist session*, Berlin, Germany 2019.

Resonant inelastic x-ray scattering study of bond order and spin excitations in nickelate thin-film structures, *New Generation of Strongly Correlated Electron Systems (NGSCES)*, Pescara, Italy 2019.

Resonant inelastic x-ray scattering study of bond order and spin excitations in nickelate thin-film structures, ***selected student talk**, CIFAR (Canadian Institute for Advanced Research) Summer School on Quantum Materials*, Vancouver, Canada 2019.

Resonant inelastic x-ray scattering study of bond order and spin excitations in nickelate thin-film structures, *DPG (German Physical Society) Spring Meeting*, Regensburg, 2019.

Bond and magnetic order in rare-earth nickelates simultaneously probed by resonant inelastic x-ray scattering, *IQST (Integrated Quantum Science and Technology) day*, **invited talk** *to present the "Science Highlight"*, Germany, 2018.

Ultrahigh-resolution resonant inelastic x-ray scattering from rare-earth nickelates: magnetic and dd-excitations, *DPG (German Physical Society) Spring Meeting*, Berlin, 2018.

Site-selective probe of magnetic and dd excitations in rare-earth nickelates using resonant inelastic x-ray scattering, *Max Planck – UBC – UTokyo School about Elementary Excitations in Quantum Materials*, Tokyo, Japan 2018.

Determining the optical constants of NiO with Resonant X-Ray Reflectivity, *DPG (German Physical Society) Spring Meeting*, Regensburg, 2016.

Other Conferences Attended/ Poster Contributions:

Summer School of the Max Planck – UBC – UTokyo Center about Design and Synthesis of Quantum Materials, Stuttgart, Germany, 2020.

IMPRS (International Max Planck Research School) Workshop on Frontiers of Quantum Materials (together with Peking University), Stuttgart, Germany 2019.

CIFAR (Canadian Institute for Advanced Research) program meeting on Quantum Materials, Vancouver, Canada 2019.

International Workshop on Oxide-Electronics (iWOE), Les Diableres, Switzerland, 2018.

New Generation of Strongly Correlated Electron Systems, San Sebastian, Spain 2018.

Max Planck – UBC – UTokyo School about Elementary Excitations in Quantum Materials, Tokyo, Japan 2018.

Frontiers of Research in Quantum Materials, Stuttgart, Germany 2017.

Advanced Light Source User Meeting, Berkeley, USA, 2013.

American Geophysical Union Fall Meeting, San Francisco, USA 2013.

Katrin Fürsich

Max Planck Insitute for Solid State Research
Heisenbergstr. 1
70569 Stuttgart, Germany
K.Fuersich@fkf.mpg.de

Education

2016 -2020	PhD in physics (expected graduation 2020)
	Max Planck Institute for Solid State Research, Germany
2014 - 2016	M.Sc. Nanotechnology
	Julius Maximilians University Würzburg, Germany
2010 - 2013	B.Sc. Nanotechnology (a solid state physics program)
	Julius Maximilians University Würzburg, Germany

Research Experience

2016 -2020	PhD student with Prof. Dr. B. Keimer
	Max Planck Institute for Solid State Research, Germany
2013 - 2014	Visiting researcher with Dr. M. Gilles & Prof. Dr. S. Leone
	Lawrence Nationoal Lab, Berkeley, USA

Awards and Scholarships

2020	Selected to attend the 70th Lindau Nobel Laureate Meeting (Interdisciplinary), postponed to 2021 due to COVID-19
2017	Female physicists award by the Bavarian Ministry of Science for an outstanding Master thesis, press releases [1] and [2]
2017	Röntgen award of the University of Würzburg for an outstanding Master's degree, press release (in German only)
2013	DAAD scholarship for a 9 month research stay at the University of California, Berkeley, California, USA
2010	Max-Weber-Fellow, Scholarship from the State of Bavaria, administered by the German National Merit Foundation